Analiza preostale čvrstoće oštećene totalne proteze kuka

Babić, Milena

Master's thesis / Diplomski rad

2019

Degree Grantor / Ustanova koja je dodijelila akademski / stručni stupanj: **University of Zagreb, Faculty of Mechanical Engineering and Naval Architecture / Sveučilište u Zagrebu, Fakultet strojarstva i brodogradnje**

Permanent link / Trajna poveznica: https://urn.nsk.hr/urn:nbn:hr:235:724874

Rights / Prava: In copyright / Zaštićeno autorskim pravom.

Download date / Datum preuzimanja: **2024-03-29**

Repository / Repozitorij:

Repository of Faculty of Mechanical Engineering and Naval Architecture University of Zagreb







UNIVERSITY OF ZAGREB
Faculty of mechanical engineering and naval architecture

MASTER'S THESIS

Milena Babić

Zagreb, 2019.

UNIVERSITY OF ZAGREB
Faculty of mechanical engineering and naval architecture

RESIDUAL STRENGTH ASSESSMENT OF A DAMAGED TOTAL HIP PROSTHESIS

Supervisor:

Prof. dr. sc. Željko Božić

Student:

Milena Babić

Zagreb, 2019.

I hereby declare that this thesis is entirely the result of my own work, except where it is indicated otherwise. I have fully cited all the used sources and I have only used the ones given in the list of references.

I would like to thank prof. dr. sc. Željko Božić for his time, patience and valuable guidance during the work on this thesis and for encouraging me to pursue this topic over the past years.

I would also like to truly thank my family and friends for all the support they have given me during my studies.

Milena Babić

SVEUČILIŠTE U ZAGREBU
FAKULTET STROJARSTVA I BRODOGRADNJE
Središnje povjerenstvo za završne i diplomske ispite
Povjerenstvo za diplomske ispite studija strojarstva za smjerove:
procesno-energetski, konstrukcijski, brodostrojarski i inženjersko modeliranje i računalne simulacije

Sveučilište u Zagrebu Fakultet strojarstva i brodogradnje	
Datum 17 -01- 2019	Prilog
Klasa: 602-04/19-6/13	
Ur. broj: 15-1703-19-13	

DIPLOMSKI ZADATAK

Student: **Milena Babić** Mat. br.: 0035193108

Naslov rada na hrvatskom jeziku: **Analiza preostale čvrstoće oštećene totalne proteze kuka**

Naslov rada na engleskom jeziku: **Residual strength assessment of a damaged total hip prosthesis**

Opis zadatka:

Femoral component of a total hip prosthesis can loosen from the bone, after years of usage, due to dynamic loading caused by human walking and other movements. Under cyclic loading damage can accumulate at stress concentration sites of femoral component of the prosthesis. Due to damage accumulation, a crack can initiate and further propagate by fatigue mechanism. At a critical combination of the crack size and applied load, when stress intensity factor reaches a critical value, fracture of the femoral component of the prosthesis can occur.

In this work, a damaged prosthesis with a crack initiated at stress concentration sites for a case of loosened femoral component of the prosthesis will be considered. An existing FEM model of femoral component of a total hip prosthesis previously developed and used to identify stress concentration sites should be adjusted and further developed to model the damaged prosthesis with a fatigue crack. The crack front shape should be modelled based on results of case studies of failed total hip prosthesis reported in relevant literature. Linear elastic FEM analysis should be carried out assuming loading at regular human walk and previously developed load models, as reported in contemporary literature. The applied loading and boundary conditions follow the model from recently published papers and for the analysis *Abaqus* software shall be used. Using linear elastic fracture mechanics, stress intensity factors should be calculated for different crack depths.

The Thesis will list the bibliography and any assistance received during this study.

Zadatak zadan:	Datum predaje rada:	Predviđeni datum obrane:
15. studenog 2018.	17. siječnja 2019.	23., 24. i 25. siječnja 2019.

Zadatak zadao: Predsjednica Povjerenstva:

Prof. dr. sc. Željko Božić Prof. dr. sc. Tanja Jurčević Lulić

TABLE OF CONTENTS

LIST OF FIGURES III
LIST OF TABLES VI
NOMENCLATURE VII
ABSTRACT VIII
SAŽETAK IX
PROŠIRENI SAŽETAK (EXTENDED ABSTRACT IN CROATIAN) X
1. INTRODUCTION 1
2. HIP JOINT ANATOMY AND BIOMECHANICS 5
2.1. Hip joint biomechanics 7
2.2. Common causes of hip joint pain and hip replacement surgery 10
3. HIP PROSTHESIS 12
3.1. Classifications of hip prostheses 12
3.1.1. Total hip prosthesis 12
3.1.2. Partial hip prosthesis 14
3.1.3. Hip resurfacing 15
4. 3D SCANNING 16
5. FINITE ELEMENT MODEL AND ANALYSIS 19
4.1. Geometry and boundary conditions 19
4.2. Materials 22
4.3. Loading conditions 22
4.4. Mesh 25
6. STRESS CONCENTRATION SITES 28
7. FRACTURE MECHANICS 34
7.1. Linear elastic fracture mechanics 43
7.1.2. Stress at the crack tip 43
7.1.3. Stress intensity factor 45
8. FINITE ELEMENT METHOD IN FRACTURE MECHANICS 46
8.1. Isoparametric finite elements 46
8.1.1. Two dimensional rectangular elements 46
8.2. Singular finite elements 47
8.2.1. Singular elements for solving linear elastic problems 48
9. STRESS INTENSITY FACTOR FOR A 3D QUARTER-ELLIPTICAL CORNER CRACK 51
9.1. Analytical solution 56
10. CRACK MODELLING ON THE FEMORAL COMPONENT OF A TOTAL HIP PROSTHESIS 58
11. CONCLUSION 71

REFERENCES 72
ENCLOSURE 77

LIST OF FIGURES

Figure 1. Fractured femoral components of total hip prostheses [2][38]. 3
Figure 2. Fatigue surface of the femoral component of a total hip prosthesis: (a) crack initiation site; (b) propagation lines; (c) final fracture zone [25]. 3
Figure 3. Hip joint [36] 5
Figure 4. Hip joint movements [39] 6
Figure 5. Q angle [40] 6
Figure 6. CCD angle: (a) coxa vara; (b) normal; (c) coxa valga [40] 7
Figure 7. The static resultant force acting on the hip joint during normal human walking [35]. 8
Figure 8. The static resultant force acting on the hip joint during limping [35]. 9
Figure 9. The static resultant force acting on the hip joint during normal human walking (F_R) compared to the static resultant force acting on the hip joint during limping (F_{R1}) [35]. 9
Figure 10. Total hip prosthesis [42] 13
Figure 11. (a) Calibration process; (b) sample of the prosthesis with reference point markers. 16
Figure 12. 3D scanning process 17
Figure 13. (a) The obtained point cloud; (b) CAD model built based on the point cloud. 18
Figure 14. Example of two tied components [44]. 20
Figure 15. (a) Femoral component shaft-cement mantle tie; (b) Cement mantle-fixture (bone) tie. 21
Figure 16. (a) Fixed base of the assembly; (b) tied surfaces. 21
Figure 17. (a) Angle of 9° in flexion; (b) angle of 10° in adduction. 23
Figure 18. The load applied in Case I 24
Figure 19. The load applied in Case II. 25
Figure 20. C3D10 element [47]. 25
Figure 21. (a) Mesh generated on the femoral component; (b) mesh of the cement mantle; (c) mesh of the fixation (bone); (d) detail of the mesh on the expected stress concentration location. 26
Figure 22. Mesh of the assembly. 27
Figure 23. Von Mises stress distribution for the prosthesis-cement-bone assembly: (a) Case I; (b) Case II. 28
Figure 24. Von Mises stress distribution for Case I (a) stress concentration location on the posterior-lateral side; (b) stress distribution on the femoral component; (c) stress concentration location on the anterior-medial side. 29
Figure 25. Maximum principal stress (absolute) distribution for Case I (a) stress concentration location on the posterior-lateral side; (b) stress distribution on the femoral component; (c) stress concentration location on the anterior-medial side. 29
Figure 26. Von Mises stress distribution for Case II (a) stress concentration location on the lateral side; (b) stress distribution on the femoral component; (c) stress concentration location on the medial side. 30
Figure 27. Maximum principal stress (absolute) distribution for Case II (a) stress concentration location on the lateral side; (b) stress distribution on the femoral component; (c) stress concentration location on the medial side. 30

Figure 28. Displacement on undeformed shape: (a) Case I; (b) Case II. 31
Figure 29. Displacement in both considered cases with deformation scale factor 50: (a) Case I; (b) Case II. 32
Figure 30. S-N curve of ASTM F-745. 33
Figure 31. Important parameters in fracture mechanics. 34
Figure 32. Classification of fracture mechanics. 35
Figure 33. Residual strength diagram (influence of the crack size on the strength) [49]. 36
Figure 34. Residual strength diagram based on nominal engineering stress [49]. 37
Figure 35. Crack propagation in time [49]. 38
Figure 36. Fatigue crack growth mechanism [51]. 39
Figure 37. Microscopic view of fatigue striation on the failed femoral component shaft [2]. 40
Figure 38. Fracture example: (a) brittle; (b) ductile [52]. 40
Figure 39. Brittle fracture (cleavage mechanism) at the blunted crack tip. Bottom: incident light reflection on the facets [51]. 41
Figure 40. Stages of rupture (ductile fracture) [51]. 42
Figure 41. Fracture modes: (a) Mode I (Opening mode); (b) Mode II (In-plane shear); (c) Mode III (Out-of-plane shear) [51]. 43
Figure 42. Stress at the crack tip [49]. 43
Figure 43. Infinite plate containing a central crack with uniform loading [49]. 44
Figure 44. A finite plate containing a central crack with uniform loading [49]. 45
Figure 45. Transformation of a regular rectangular element into an arbitrary element [49]. . 47
Figure 46. The usual mesh around the crack tip [49]. 48
Figure 47. Definition of the singular element used in the linear elastic analysis [49]. 49
Figure 48. Dimensions of the model, the applied load and boundary conditions (fixed bottom surface). 51
Figure 49. Crack front (red) and crack seam (from the corner to the red line). 52
Figure 50. Mesh. 53
Figure 51. Detail of the mesh. 53
Figure 52. Definition of crack extension direction. 54
Figure 53. Von Mises stress distribution. 54
Figure 54. Detail of the Von Mises stress distribution around the crack front. 55
Figure 55. K_1 values along the crack front for the five considered contours. 55
Figure 56. Convergence of the K_1 value for node 24. 56
Figure 57. Comparison of analytically and numerically obtained K_1 values. 57
Figure 58. The site with highest tensile stress value on the femoral component in Case I. ... 58
Figure 59. Position of the torus in the prosthesis-cement-bone assembly. 60
Figure 60. Partitioned cells of the femoral component shaft. 60
Figure 61. Crack front (red line) and the crack seam (faces from the edge to the red line) for the three crack lengths. 61
Figure 62. Mesh on the cells made by partitioning the femoral component shaft by the tori. 62
Figure 63. Elements around the crack front. 62
Figure 64. Mesh on the section containing the crack front for one crack length. 63
Figure 65. Mesh on the section containing the crack front for the three crack lengths. 63
Figure 66. Mesh detail on the prosthesis femoral component model. 64
Figure 67. Von Mises stress distribution for the smallest crack size. 64
Figure 68. Von Mises stress distribution for the middle crack size. 65
Figure 69. Von Mises stress distribution for the longest crack size. 65
Figure 70. The first and the last node location on the crack front. 66
Figure 71. K_I values along the contours for the smallest considered crack size. 67

Figure 72. Convergence of K_I value for node 30 for the smallest considered crack size. 67
Figure 73. K_I values along the contours for the middle crack size. 68
Figure 74. Convergence of K_I value for node 30 for the middle crack size. 68
Figure 75. K_I values along the contours for the longest considered crack size. 69
Figure 76. Convergence of K_I value for node 30 for the longest crack size. 69
Figure 77. Comparison of K_I values for the three considered crack lengths. 70

LIST OF TABLES

Table 1. Percent of the body weight acting on the hip joint during several normal human activities..... 10
Table 2. Mechanical properties of stainless steel for cast 18Cr12.5Ni2.5Mo..... 22
Table 3. Material properties of the cement mantle and cortical bone. 22
Table 4. Number of elements for each part of the assembly 26
Table 5. Comparison of analytically and numerically obtained K_I values for several nodes along the crack front..... 56

NOMENCLATURE

a	m	Crack length
a_p	m	Maximum allowed crack length
Δa	m	Crack extension
F_R	N	Static resultant force acting on the hip joint
F	N	Force acting on the hip joint based on the ISO 7206-4 standard
F_p	MPa	Minimum residual strength
F_u	MPa	Ultimate strength
F_s	MPa	Maximum expected work load
K	MPa√m	Stress intensity factor
K_1		Stress intensity factor for Mode I
M	N	Abductor muscle force
N	-	Number of cycles to crack initiation
S	-	Safety factor
u,v,w	m	Displacements
β	-	Geometry factor
θ	°	Angle of the quarter-elliptical corner crack
σ_p	MPa	Maximum allowed stress
σ_s	MPa	Maximum work stress
σ_y	MPa	Yield strength

ABSTRACT

Fatigue life of a loosened femoral component of the total hip prosthesis was considered for the loads based on the standard ISO 7206-4 and loads which occur due to normal human walking, by using finite element method. A reverse engineering procedure was implemented, where the CAD model of a total hip prosthesis was created by means of 3D scanning. By using the obtained CAD model, the FEM model was developed. Finite element analyses were performed for the obtained FEM model of the hip prosthesis implanted in cement and bone. The analyses showed that high tensile stresses occur on posterior-lateral side of the upper part of the femoral shaft, where fatigue cracks occur in real cases. Based on the analyses results and fracture surface from the real cases, a corresponding crack was modelled on the femoral component model. Several crack depths were considered and for each of them stress intensity factor values were obtained.

Key words: Fatigue life assessment; Finite element analysis; Fracture mechanics; Reverse engineering; 3D scanning; Total hip prosthesis

SAŽETAK

Životni vijek olabavljene femuralne komponente totalne proteze kuka je razmatran za opterećenja propisana ISO 7206-4 standardom te za opterećenja koja se pojavljuju tijekom normalnog hoda čovjeka, korištenjem metode konačnih elemenata. Primijenjen je proces povratnog inženjerstva, pri čemu je CAD model totalne proteze kuka dobiven pomoću 3D skeniranja. Na temelju dobivenog CAD modela, razvijen je FEM model. Provedene su analize metodom konačnih elemenata za dobiveni FEM model femuralne komponente totalne proteze kuka ugrađen u model koštanog cementa i zbite (kortikalne) kosti. Rezultati analize su pokazali da se najveće vrijednosti vlačnih naprezanja pojavljuju na posterior-lateralnoj strani gornjeg dijela tijela femuralne komponente, gdje se u stvarnim slučajevima iniciraju zamorne pukotine. Modelirana je odgovarajuća pukotina na temelju dobivenih rezultata i površine po kojoj propagiraju pukotine u stvarnim slučajevima. Razmatrano je nekoliko duljina pukotine te su za svaku od njih utvrđene vrijednosti koeficijenta intenzivnosti naprezanja.

Ključne riječi: Procjena životnog vijeka; Metoda konačnih elemenata; Mehanika loma; Povratno inženjerstvo; 3D skeniranje; Totalna proteza kuka

PROŠIRENI SAŽETAK (EXTENDED ABSTRACT IN CROATIAN)

UVOD

Ugradnja totalne proteze zgloba kuka je uspješna strategija koja se već desetljećima primjenjuje, te značajno poboljšava kvalitetu pacijentovog života, omogućujući povratak normalnih funkcija zgloba kuka izgubljenih uslijed oštećenja ili loma prirodnog zgloba kuka. Proteza zgloba kuka može biti ugrađena u bedrenu kost (femur) pomoću koštanog cementa ili izravno. Uspjeh i dugovječnost totalne proteze kuka je direktno povezana sa stabilnošću veza između proteze i kosti. Jedni od najvećih problema kod proteze kuka su zamor i trošenje materijala te se često povezuju s labavljenjem femuralne komponente totalne proteze kuka. Labavljenje femuralne komponente smatra se najvećim uzrokom loma proteze kuka. Može biti izazvano raznim mehanizmima i mehaničko-biološkim konfliktima. Kada je tek počela šira primjena totalnih proteza kuka, zamjene primarne proteze kuka su često bile potrebne. U međuvremenu zbog napretka na području materijala i konstruiranja došlo do smanjenja broja zamjene proteze kuka zbog infekcija i dislokacija, ali je oštećenje proteze uslijed labavljenja još uvijek učestala pojava.

Prilikom procjene životnog femuralne komponente totalne proteze kuka, razmatrana su dva slučaja opterećenja. U prvom slučaju (Case I), rubni uvjeti i opterećenje su temeljeni na testnim uvjetima propisanima standardom ISO 7206-4. U drugom slučaju (Case II), opterećenje se svodi na statičku rezultirajuću silu koja djeluje na zglob kuka prilikom hoda čovjeka. Mjesta koncentracije naprezanja su identificirana za oba slučaja opterećenja te je određen broj ciklusa do inicijacije pukotine za dobivene iznose naprezanja.

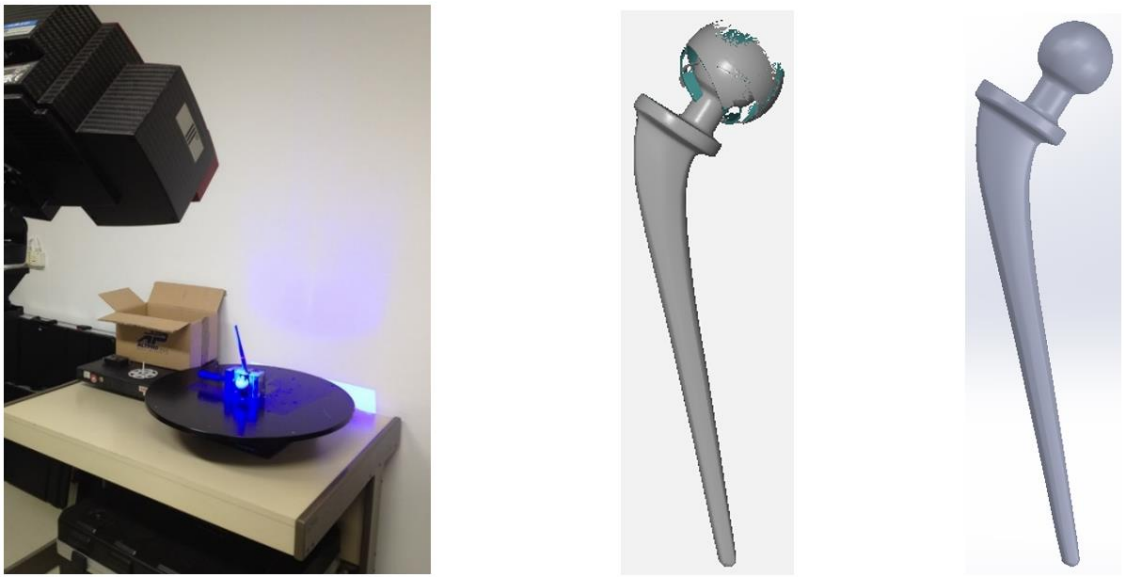
S obzirom da se i dalje bilježe slučajevi loma proteza kuka, prilikom konstruiranja proteza kuka u obzir treba uzimati i parametre mehanike loma. Nužno je razumjeti pojave inicijacije i propagacije pukotine kako bi se izbjegli in vivo lomovi proteza kuka. Metoda konačnih elemenata se danas uobičajeno koristi za preliminarna ispitivanja biomedicinskih komponenti komplicirane geometrije. U svrhu izrade ovog rada, metoda konačnih elemenata je korištena kako bi se modeliralo nekoliko dubina pukotine na primjeru femuralne komponente totalne

proteze kuka. Pukotina je modelirana na temelju identificiranih mjesta koncentracije naprezanja za slučaj opterećenja temeljen na standardu ISO 7206-4.

3D SKENIRANJE

3D skeniranje uzorka proteze kuka je provedeno pomoću optičkog skenera Advanced TOpometric Sensor (ATOS) i GOM 2016 softvera. Kako bi se postignula željena točnost rezultata, skener je prije početka skeniranja kalibriran. Kalibracija je provedena na kalibracijskoj ploči skeniranjem 18 karakterističnih točaka. Uzorak proteze je očišćen te je polirana površina glave femuralne komponente matirana pomoću otopine titanovog dioksida i alkohola. Referentne točke su postavljene na površinu proteze kako bi se omogućilo pravilno poravnanje različitih snimki nakon završetka skeniranja.

Uzorak je zatim pričvršćen na rotacijski stol steznom napravom kako bi se onemogućilo pomicanje uzorka tijekom skeniranja. Rotacijski stol je osam puta okrenut za 45° te su za svaku poziciju snimljeni skenovi. Na kraju su skenovi poravnati tako da se ručno izaberu tri referentne točke vidljive u oba skena, nakon čega softver prepozna ostale referentne točke. Svi skenovi su na taj način spojeni u jedan set podataka koji se naziva oblak točaka, u STL formatu. Dobivena STL datoteka je učitana u softver Geomagic Design X, gdje je na temelju oblaka točaka izgrađen CAD model femuralne komponente skenirane proteze kuka. Proces skeniranja, oblak točaka i dobiveni CAD model su prikazani na slici Slika 1.



(a) **(b)** **(c)**

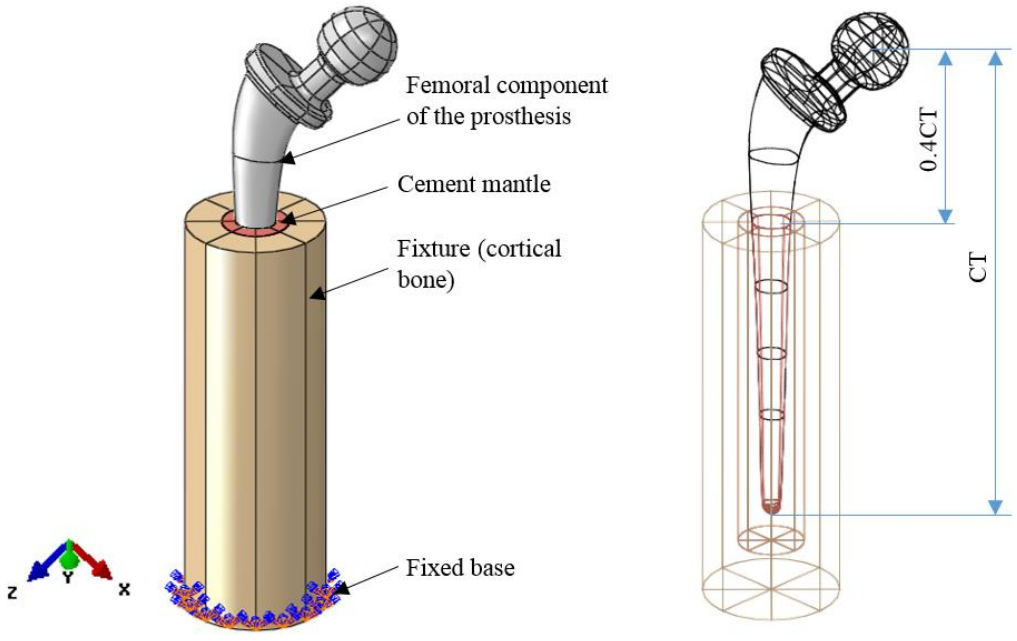
Slika 1. (a) Proces skeniranja; (b) dobiveni oblak točaka; (c) izgrađeni CAD model.

ANALIZA METODOM KONAČNIH ELEMENATA

FEM model femuralne komponente proteze je modeliran u softveru Abaqus na temelju izgrađenog CAD modela. Kao posljedica izgradnje CAD modela procesom povratnog inženjerstva, u geometriji CAD modela su se pojavile greške koje uključuju male rubove i površine. Te greške dalje mogu uzrokovati greške u mreži konačnih elemenata dobivenog modela i nestvarna mjesta koncentracije naprezanja, stoga ih je bilo potrebno ispraviti.

Geometrija i rubni uvjeti

Analizirani model se sastoji od sljedeće tri komponente: femuralna komponenta proteze kuka, koštani cement i zbita (kortikalna) kost, sa zajedničkim površinama povezanima zajedno funkcijom „tie" kako je prikazano na slici Slika 2. Pomoću površine tijela femuralne komponente proteze, stvorena je odgovarajuća površina istog oblika unutar cementa. Kako je propisano korištenim standardom, tijelo femuralne komponente je učvršćeno u cement do 0.4CT, gdje je CT udaljenost između središta glave femuralne komponente i najdonje točke tijela femuralne komponente, što se može vidjeti na slici Slika 2b. Vanjska površina cementa je potpuno vezana za unutarnju površinu kosti, što je također prikazano na slikom Slika 2.



(a) **(b)**

Slika 2. (a) Fiksirana donja površina modela; (b) povezane površine komponenti u modelu.

Materijali

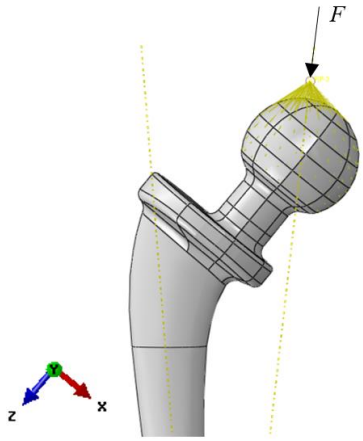
Korišteni materijal proteze je lijevani austenitni nehrđajući čelik za primjenu u implantatima ASTM F-745 (18Cr12.5Ni2.5Mo). Mehanička svojstva korištenog materijala preuzeta su iz literature [2]. Svojstva koštanog cementa su također pronađena u literaturi [2] [5], kao i svojstva kortikalne kosti koja su dobivena ispitivanjima i numeričkim simulacijama te zabilježena u korištenoj literaturi [27] [45] [29], Modul elastičnosti kortikalne kosti ovisi o gustoći kosti te je ovdje razmatrana određena gustoća, navedena u tablici Tablica 1. Svojstva materijala mogu se vidjeti u tablici Tablica 1.

Tablica 1. Svojstva korištenih materijala.

Svojstvo materijala	ASTM F-745	Cement	Zbita (kortikalna) kost
Modul elastičnosti (GPa)	0.205	2.3	27.72
Poissonov faktor	0.3	0.33	0.44
Gustoća (kg/m^3)	-	-	1860

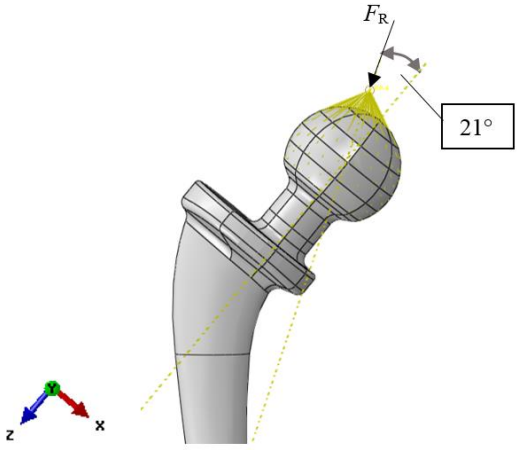
Opterećenje

S vremenom, veze između kosti i tijela femuralne komponente proteze slabe. Dugotrajnost proteze kuka ovisi upravo o tim vezama. Kako one popuštaju, tako dolazi do labavljenja proteze, što uzrokuje veći moment savijanja na tijelo femuralne komponente proteze i veća naprezanja na lateralnoj strani tijela femuralne komponente. To dalje može uzrokovati inicijaciju pukotine na mjestu koncentracije vlačnih naprezanja, propagaciju pukotine te na kraju lom proteze. Razmatrana su dva slučaja opterećenja. Prvi slučaj (Case I) je temeljen na standardu ISO 7206-4, gdje je sila od 2300 N postavljena tako da djeluje pod kutem od 9° u smjeru fleksije kuka i 10° u smjeru addukcije, od longitudinalne osi tijela femuralne komponente. S obzirom da sila u ovom slučaju djeluje izvan ravnine simetrije proteze, tijelo femuralne komponente je izloženo torziji i savijanju. Kako se kod proteze kuka sile prenose s acetabularne čašice na površinu glave femuralne komponente, koncentrirana sila je postavljena u točki iznad površine glave i zatim prenesena na cijelu površinu glave pomoću funkcije Coupling, kako je prikazano na slici Slika 3.



Slika 3. Položaj sile opterećenja u prvom razmatranom slučaju (Case I).

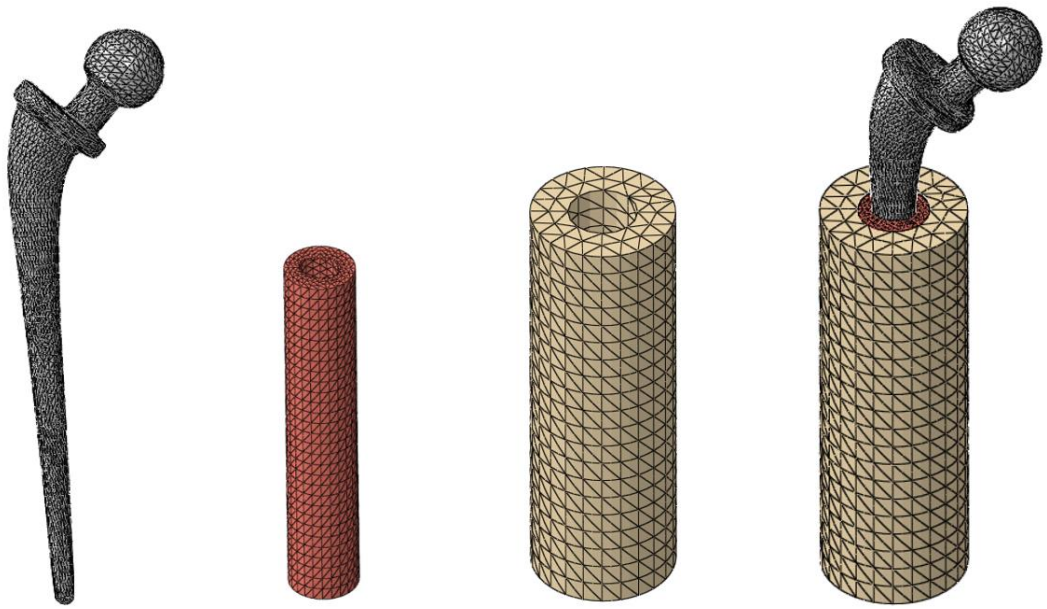
U drugom slučaju opterećenja (Case II), koncentrirana sila djeluje u ravnini simetrije proteze, pod kutem od 21° od longitudinalne osi vrata femuralne komponente, što je u suglasnosti s literaturom [35]. Iznos sile je 238% težine tijela [36] čovjeka prosječne mase od 90 kg. Sila je, kao u prvom slučaju, postavljena u točku iznad površine glave femuralne komponente i prenesena na cijelu površinu glave pomoću funkcije „coupling".



Slika 4. Položaj sile opterećenja u drugom razmatranom slučaju (Case II).

Mreža konačnih elemenata

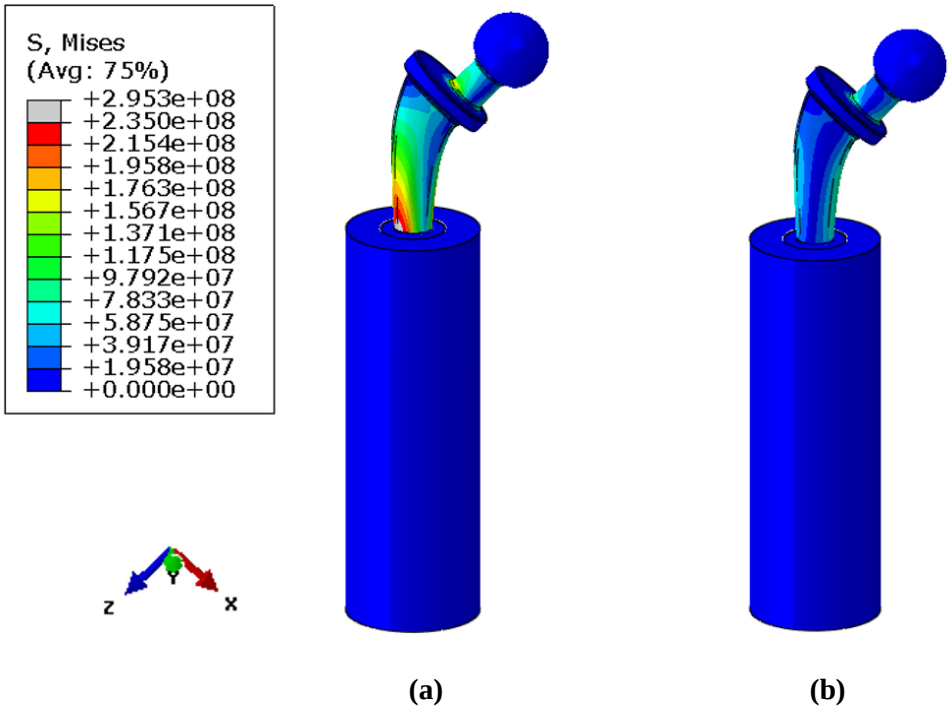
Nakon definiranja rubnih uvjeta, opterećenja i veza između komponenti modela, generirana je mreža konačnih elemenata na svim komponentama modela, kako prikazuje Slika 5. Korišteni elementi su C3D10 (tetraedarski elementi drugog reda). Mreža je posebno profinjena u području očekivane koncentracije naprezanja.



Slika 5. Mreža konačnih elemenata.

MJESTA KONCENTRACIJE NAPREZANJA, POMACI I BROJ CIKLUSA DO INICIJACIJE PUKOTINE

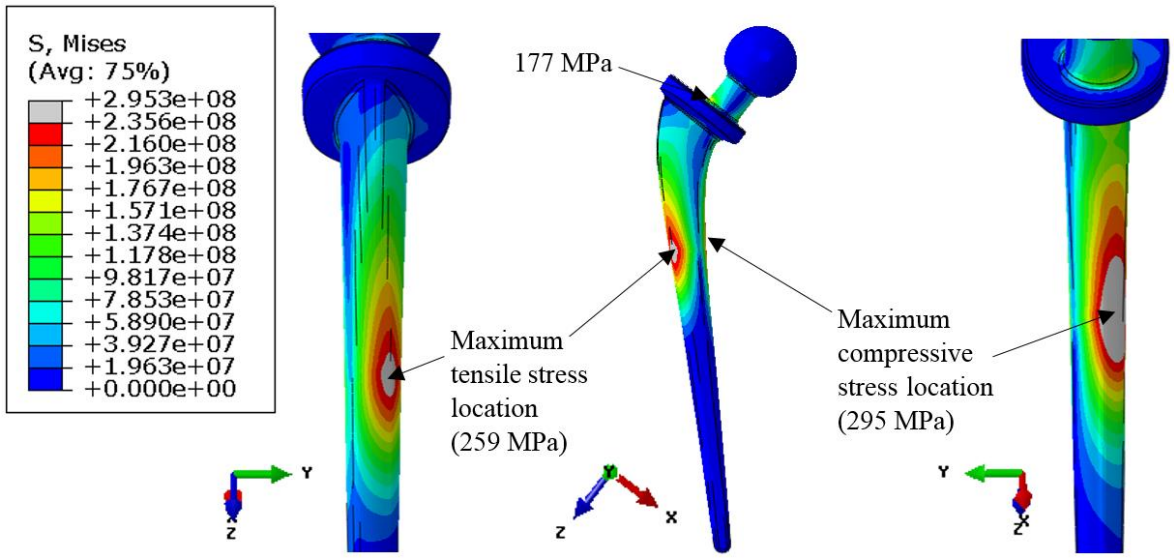
Provedenom numeričkom analizom, određena je raspodjela naprezanja za oba opisana slučaja opterećenja. Raspodjela Von Mises naprezanja za oba slučaja prikazana je na slici Slika 6.



(a) **(b)**

Slika 6. Raspodjela Von Mises naprezanja na modelu: (a) prvi slučaj opterećenja (Case I); (b) drugi slučaj opterećenja (Case II).

Raspodjela Von Mises naprezanja za prvi slučaj opterećenja (Case I), temeljen na standardu ISO 7206-4, prikazana je na slici Slika 7. Najveća vlačna naprezanja pojavila su se na posterior-lateralnoj strani gornjeg dijela tijela femuralne komponente, na rubu gdje je tijelo učvršćeno u cement. Može se zaključiti da je to mjesto s najvećom vjerojatnošću inicijacije pukotine. Najveća tlačna naprezanja pojavila su se na istoj visini, na anterior-medijalnoj strani tijela femuralne komponente.

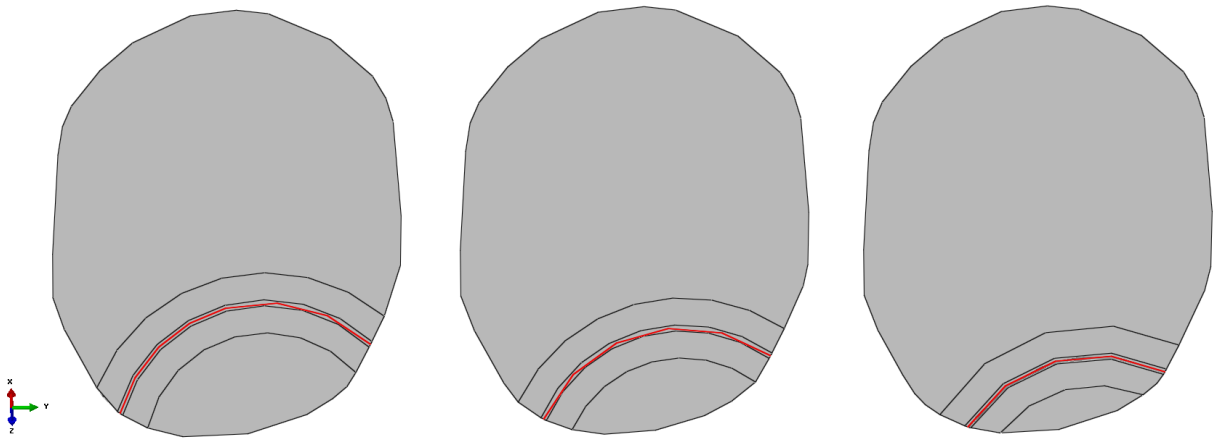


Slika 7. Raspodjela Von Mises naprezanja na femuralnoj komponenti proteze za prvi slučaj opterećenja (Case I).

Za drugi slučaj opterećenja (Case II), najveća vlačna naprezanja pojavila su se iznad ovratnika na lateralnoj strani proteze, a najveća tlačna naprezanja ispod ovratnika na medijalnoj strani proteze. Iznosi naprezanja za ovaj slučaj opterećenja (Case II) su znatno manji nego za prvi slučaj opterećenja (Case I). S obzirom da je utvrđeno mjesto s najvećom vjerojatnošću inicijacije pukotine, pomoću S-N dijagrama za materijal proteze ASTM F-745 [1] [20] određen je broj ciklusa do inicijacije pukotine za dobiveni iznos naprezanja. Za prvi slučaj opterećenja (Case I), najveća vlačna naprezanja pojavljuju se na posterior-lateralnoj strani gornjeg dijela tijela femuralne komponente i ona iznose 259 MPa. Odgovarajući broj ciklusa do inicijacije pukotine iznosi 353980. Prema podacima pronađenima u literaturi [20], proteza kuka bi trebala moći podnijeti milijun ciklusa godišnje te nakon inicijacije pukotine još 5 milijuna ciklusa. U ovom slučaju broj ciklusa do inicijacije pukotine iznosi 35% ciklusa u jednoj godini. U stvarnosti su opterećenja na protezu kuka manja nego u slučaju propisanim standardom.

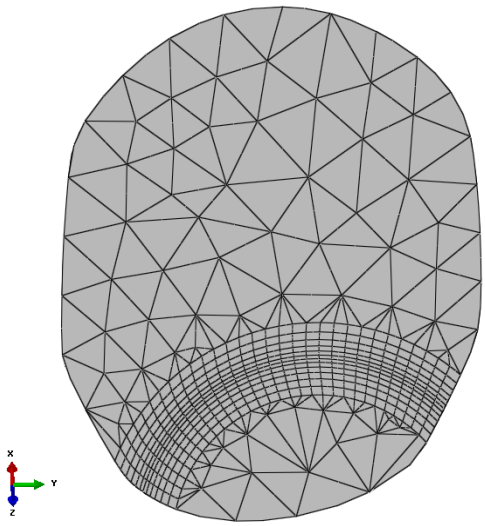
MODELIRANJE PUKOTINE NA FEMURALNOJ KOMPONENTI PROTEZE KUKA

Modelirane su tri različite duljine i položaji pukotine za prvi slučaj opterećenja (Case I). Fronta pukotine za tri razmatrane duljine i položaje pukotine je prikazana na slici Slika 8.

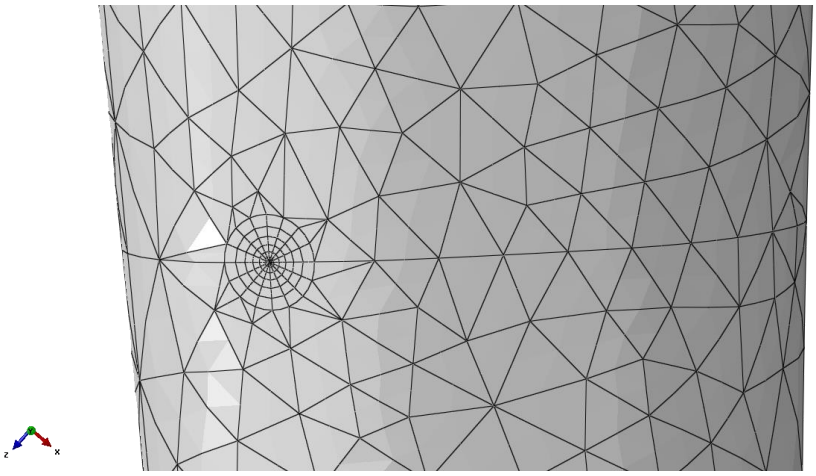


Slika 8. Fronta pukotine (crvena linija) za tri različite duljine i položaje pukotine.

U području neposredno oko fronte pukotine je generirana mreža klinastih (wedge) elemenata C3D15, kojima su središnji čvorovi pomaknuti na 0.25 duljine stranice prema fronti pukotine kako bi mogli opisati singularitet u tom području. U području oko klinastih elemenata generirana je mreža heksagonalnih elemenata drugog reda C3D20, a na ostatku modela korišteni su tetraedarski elementi drugog reda C3D10. Mreža konačnih elemenata na presjeku koji sadrži frontu pukotine prikazana je na slici Slika 9, a detalj mreže oko pukotine na femuralnoj komponenti prikazan je na slici Slika 10.

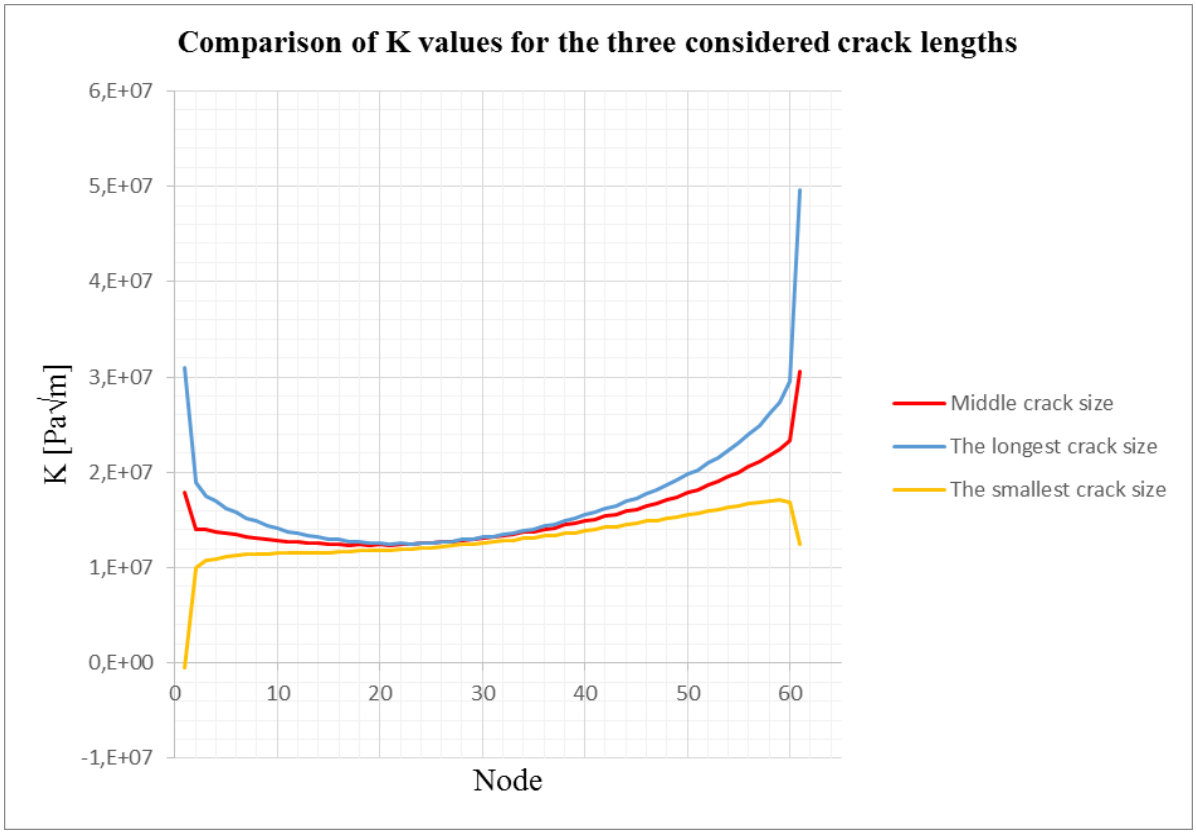


Slika 9. Mreža konačnih elemenata na presjeku koji sadrži frontu pukotine.



Slika 10. Detalj mreže konačnih elemenata oko pukotine na femuralnoj komponenti proteze.

Provedena je analiza metodom konačnih elemenata za model femuralne komponente proteze kuka oštećene s pukotinama oblika fronte prikazanih na slici Slika 8. Za svaku od razmatranih duljina pukotine dobivena je raspodjela Von Mises naprezanja te je utvrđena vrijednost faktora intenzivnosti naprezanja K_1 koristeći pet zadanih kontura oko fronte pukotine. Usporedba vrijednosti K_1 za tri razmatrane duljine pukotine po konturi najudaljenijoj od fronte pukotine prikazana je na slici Slika 11.



Slika 11. Usporedba vrijednosti K_1 za razmatrane pukotine.

ZAKLJUČAK

Analiza metodom konačnih elemenata provedena je za dva slučaja opterećenja olabavljene femuralne komponente totalne proteze kuka. Određena su mjesta koncentracije naprezanja za oba slučaja te je zaključeno da je za slučaj opterećenja temeljen na standardu ISO 7206-4 inicijacija pukotine najvjerojatnija na posterior-lateralnoj strani gornjeg dijela tijela proteze. Za taj slučaj opterećenja na temelju dobivenih rezultata, modelirane su tri duljine pukotine. Za svaku duljinu pukotine izračunate su vrijednosti faktora intenzivnosti naprezanja K_I. Pri sredini fronte pukotine, dobivena vrijednost faktora intenzivnosti naprezanja K_I je gotovo jednaka za sve tri duljine pukotine. U radu je pokazano da se faktor intenzivnosti naprezanja može izračunati za proizvoljni oblik fronte pukotine. U idućem koraku, izračunat će se faktori intenzivnosti naprezanja za veće duljine pukotine te će se moći procijeniti uvjeti nastupanja loma proteze.

1. INTRODUCTION

The present-day lifestyle, which includes reduced physical activity and irregular diet often leads to increased body weight and weakening of muscles, which make up an important part of joint support. This causes irregularities in biomechanics of human movement, including movements of hip joint. Irregular movements can further lead to permanent hip joint injuries, which in time may cause pain and stiffness of the joint. Patients with severe hip joint injuries are subject to hip replacement surgery. This type of surgery is a routine procedure after which the quality of patients' lives is considerably higher.

Total hip arthroplasty (THA) is an extremely successful strategy, implemented in large numbers worldwide, to restore the normal function of the hip joint impacted by fracture or disease [1] [2] [3]. It has become a routine procedure which significantly improves the patient's life quality [3] [4]. Hip prostheses can be fixed to the bones by cement or cementless methods [5] [6]. Bone, as a physiological living tissue, can repair, remodel and adapt itself to its surrounding environment [7]. Performance and success of long-term survival of THA, both cemented and cementless, is directly related to stability of the bond of the prosthesis and the bone or cement [5] [8] [9] [10] [11]. In hip prostheses, fatigue and wear are some of the major concerns, often associated with component loosening, the most common cause of hip prosthesis failure [12] [13] [14] [15]. Component loosening can be caused by various mechanisms and biological and mechanical conflicts [16] [17]. Cement joins the rigid femoral component of the prosthesis and the constantly changing bone [18]. It is the weakest link in the cemented total hip prosthesis because of its lower mechanical properties and brittle behaviour [5] [19]. Stem-cement debonding and cement cracking are the main causes for failure of the femoral components [14] [16] [19]. Normally, it is expected that hip prosthesis should endure minimum of 1 million cycles per year [20]. After proximal loosening, it should be able to further endure 5 million cycles [20]. In early years, the revision of hip prosthesis was a more common event due to biological and mechanical conflicts [1]. While failure due to infection, fraction and dislocation has become rare, failure caused by aseptic loosening is still common [21].

By introducing the endurance fatigue standard ISO 7206-4 in the 1980s, failure rates of hip prosthesis have significantly reduced [1] [20] [22]. However, it has been repeatedly reported that in vivo fracture of the hip prosthesis stem is still happening [23] [24] [25].

In engineering and orthopaedics 3D scanning is often used and it is becoming one of the most accurate ways of recreating prosthetics geometry [4]. In this paper a reverse engineering procedure is implemented, where the CAD model of a total hip prosthesis is created by means of 3D scanning. By using the obtained CAD model, the FEM model was developed. A finite element analysis was performed for the obtained FEM model of the hip prosthesis implanted in cement and bone. Material properties of the cement implemented in finite element analysis are in accordance with the data reported by Griza et al. [2] and Bousnane et al. [5]. Material properties of the bone applied in the finite element model correspond to the cortical bone properties obtained experimentally by Demiral et al. [26], Abdel-Wahab et al. [27] [28] [29] [30], Li et al. [7] [31] [32] [33], Alam et al. [34].

In fatigue life assessment of the total hip prosthesis femoral component the two different loading cases were considered. In Case I, loading and boundary conditions were based on fatigue standard ISO 7206-4 testing conditions. This standard is normally used to evaluate the endurance properties of hip prostheses femoral components, as described by Griza et al. [2]. In Case II, the load was applied according to the force distribution model given by Ruszkowski et al. [35]. In this case, the applied force was based on the measurement results of hip joint loading during normal human activities, as reported by Bergmann et al. [36] [37]. Stress concentration sites were identified and for the obtained stress values, the numbers of cycles to crack initiation were determined by using the S-N curve of the considered stainless steel prosthesis material ASTM F-745, [1] [20].

Since hip prostheses failure still occurs, as can be seen in Figure 1 and Figure 2, the fracture mechanics parameters need to be considered in the prosthesis design. It is necessary to understand the crack initiation and the crack growth phenomena, in order to prevent the possible in vivo fracture of the prosthesis.

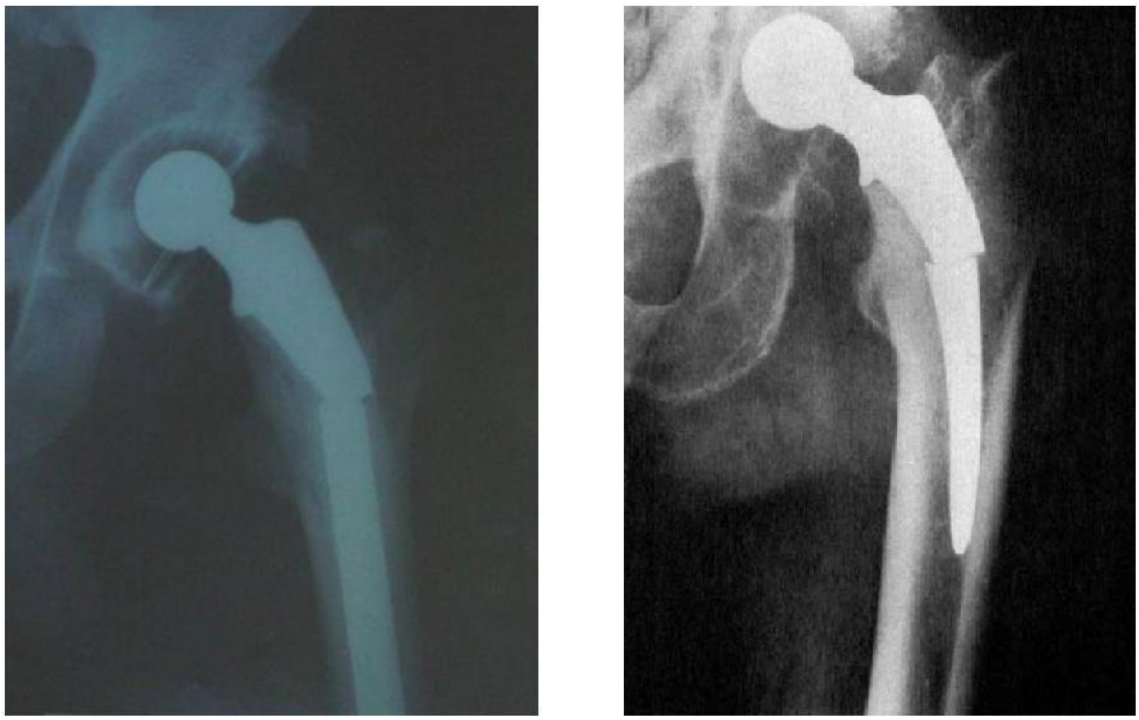


Figure 1. Fractured femoral components of total hip prostheses [2][38].

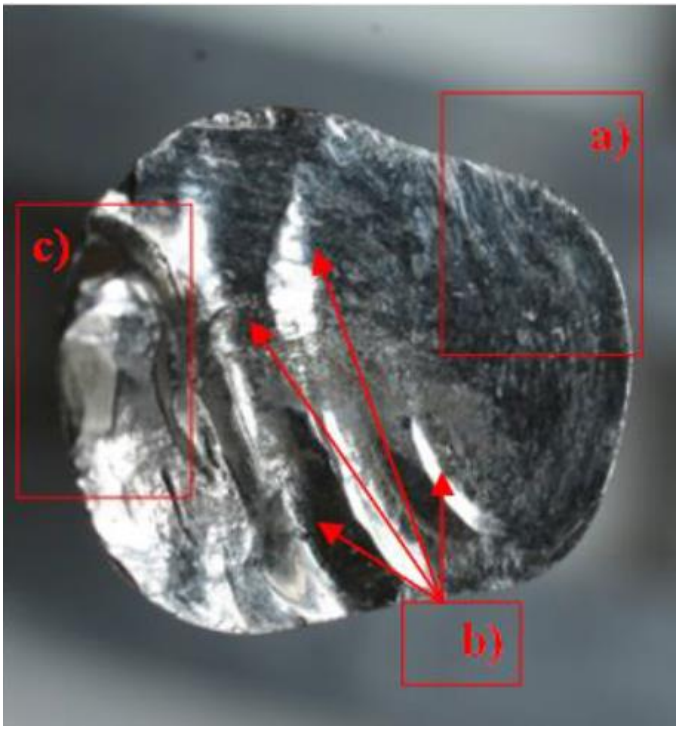


Figure 2. Fatigue surface of the femoral component of a total hip prosthesis: (a) crack initiation site; (b) propagation lines; (c) final fracture zone [25].

For biomedical components with complicated geometry and structure, such as total hip prosthesis, using the numerical simulations for preliminary studies is common. The conventional FEM can be used for simulating crack propagation in biomedical components with complex geometry. For this study, classical FEM was used to model several different length cracks on the hip prosthesis femoral component at the site where crack initiation was expected based on the obtained stress concentration sites and real case examples. The crack was modelled for Case I loading conditions, on the posterior-lateral side of the upper part of the femoral component shaft, where maximum tensile stresses appeared. Several different depths of the crack were considered and the stress intensity factor values were determined for each crack depth.

2. HIP JOINT ANATOMY AND BIOMECHANICS

Hip joint is one of the largest joints in human body. It is a ball-socket synovial joint. Femoral head is the ball and the acetabulum is the socket, as can be seen in Figure 3. The hip joint is the connection of the femur and the pelvis. Therefore it connects the lower extremity with the axial skeleton.

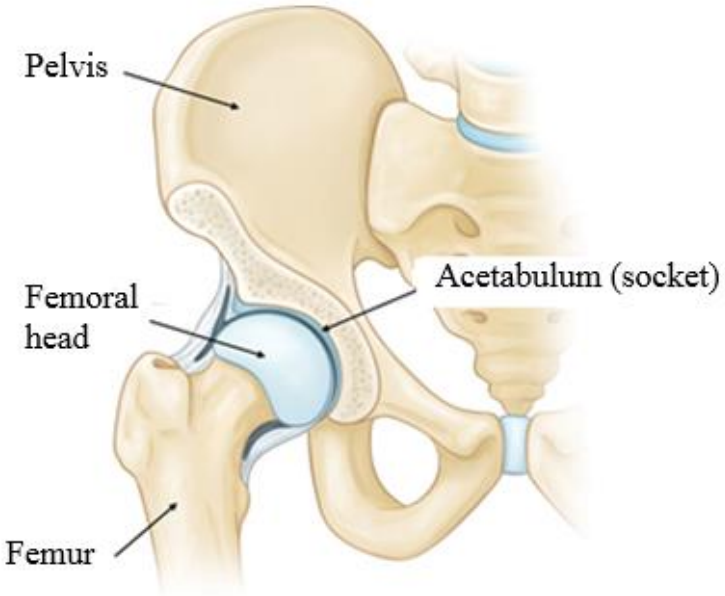


Figure 3. Hip joint [36].

Femoral head and acetabulum surfaces are covered by thick, white, smooth articular cartilage which is kept slippery by fluid made in the synovial membrane. The articular cartilage enables painless and easy movements of the femoral head inside the acetabulum. Labrum is a cartilage ring on the rim of the acetabulum that makes acetabulum deeper and more stable. Articular capsule, a fibrous connective tissue structure, is connected to labrum. Synovial membrane covers the inner surface of the articular capsule and produces synovial fluid which is thick and slimy. Hip joint is surrounded with strong ligaments and thigh muscles that keep the joint in the right position, enable the stability of the joint and prevent it from dislocation. Hip joint shape and structure enable movements of flexion, extension, abduction, adduction, rotation and many combinations of those movements, as shown in Figure 4.

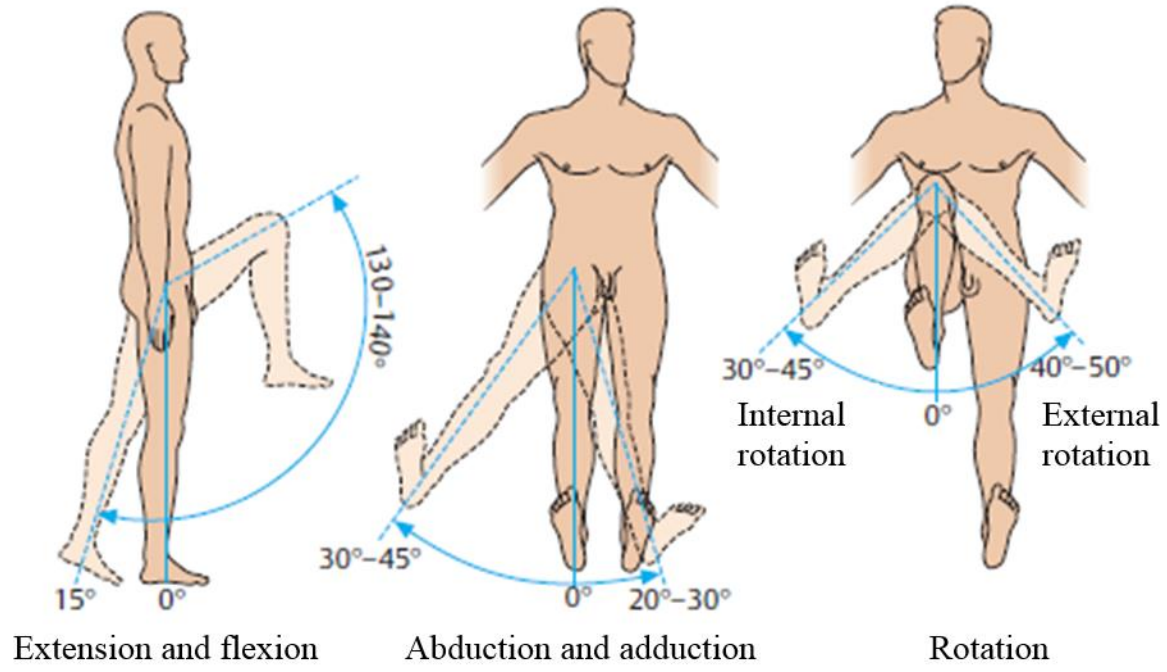


Figure 4. Hip joint movements [39].

Q angle, shown in Figure 5, is the angle that a line connecting the mid-point of the patella and a point near the anterior superior iliac spine closes with the line connecting the mid-point of the patella and tibial tubercle and in adults it is between 9 to 16°.

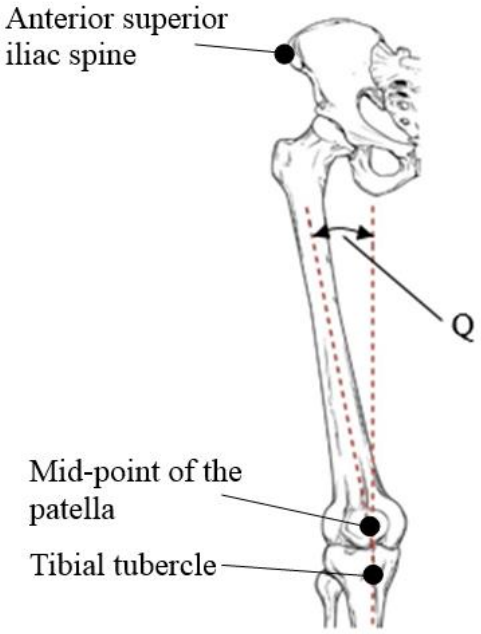
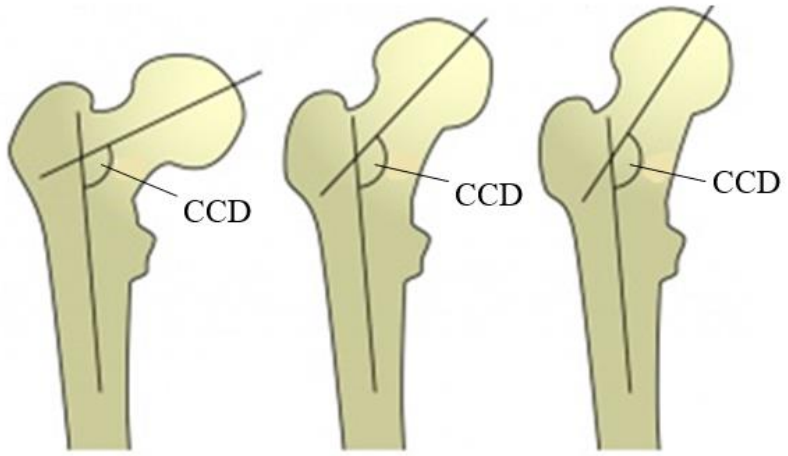


Figure 5. Q angle [40].

CCD angle (caput-collum-diaphyseal angle) is the angle between the longitudinal axis of the femoral neck and femoral shaft and in adults it is normally between 126 and 133°. Coxa vara is a deformity of the hip where CCD angle is decreased and coxa valga is a deformity of the hip where CCD angle is increased, as shown in Figure 6.



(a) CCD<126° (b) 126°<CCD>133° (c) CCD>133°

Figure 6. CCD angle: (a) coxa vara; (b) normal; (c) coxa valga [40].

2.1. Hip joint biomechanics

Most of the research works about the hip joint are based on loading conditions during normal human walking. Besides normal human walking, many of the research works are based on loading conditions during walking up and down the stairs, since those are the most common every day activities which humans are subjected to. During normal standing, both of the hip joints are loaded the same and each hip joint carries half of the upper human body weight. In this position, pelvis is the most stable and hip joints loaded less than in any other positions. When the position changes, the loads acting on the hip joint change accordingly. For example, loads acting on the hip joint during standing on one leg are significantly higher than during normal standing because the hip joint needs to carry whole upper body weight instead of half of the upper body weight.

Normal human walking is mostly based on flexion and extension, but determining the exact loading conditions on the hip joint is not so simple. Therefore simplified force distribution model on the hip joint during normal human walking is often used and it is based on the static resultant force F_R. The static resultant force closes a 16° angle with the line of gravity and its

range depends on the body weight and the abductor muscle force *M* that maintains a level pelvis and the weight of the body *T* [35], which can be seen in Figure 7. The above described forces bend the femur and cause tensile and compressive stresses on the femoral neck. These stresses are transferred to the diaphysis of the femur [35]. Loading conditions on hip prostheses are similar to loading conditions on the hip joint and the loads transfer from the femoral component of the prosthesis to the femur. Because of the high stresses at connection locations of the prosthesis and the bone, the bonds between the prosthesis and the bone can weaken and fail, which causes prosthesis loosening. After hip replacement surgery, patients often limp in order to decrease the load range acting on the hip prosthesis. This causes the resultant force acting on the hip joint to be more inclined to the line of gravity [35], which consequently bends the prosthesis femoral component shaft more than during normal walking, as shown in Figure 8 and Figure 9.

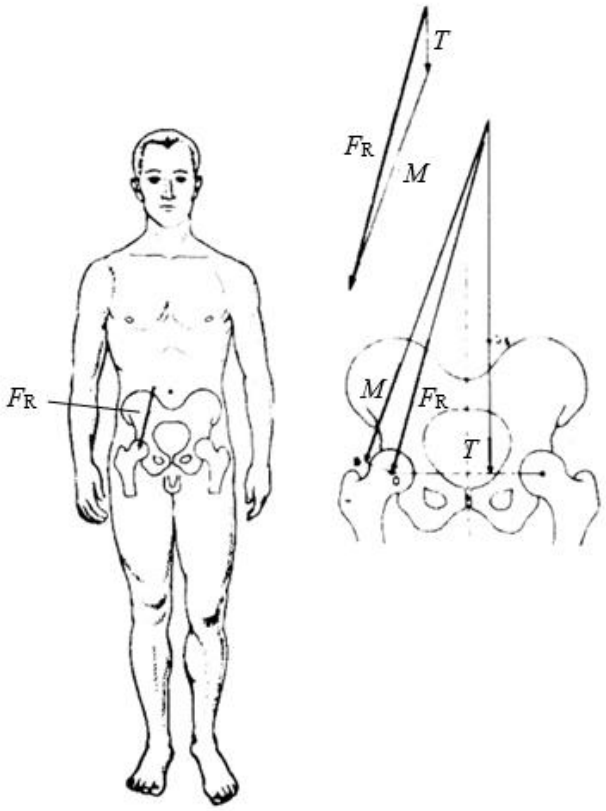


Figure 7. The static resultant force acting on the hip joint during normal human walking [35].

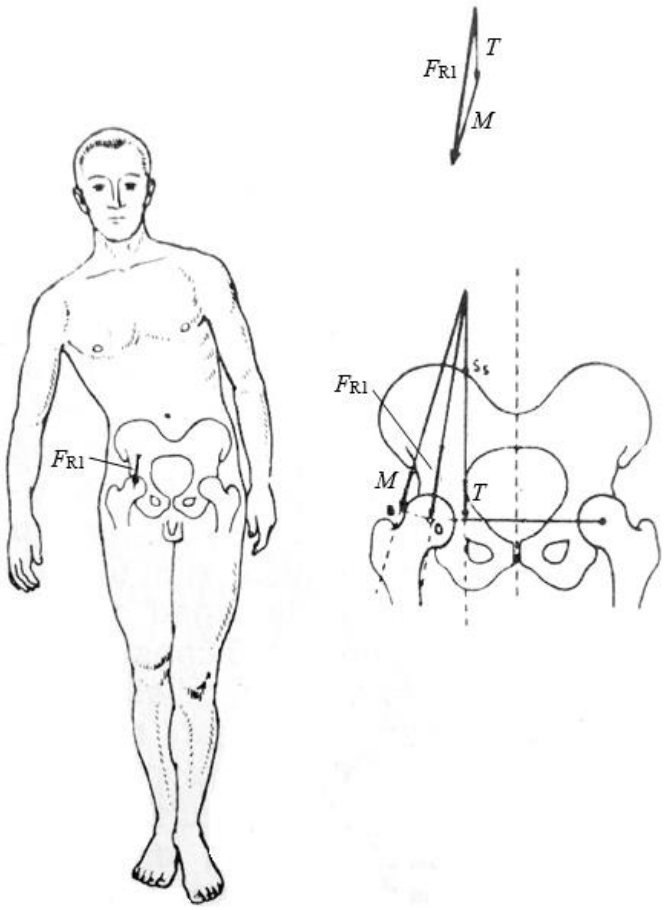


Figure 8. The static resultant force acting on the hip joint during limping [35].

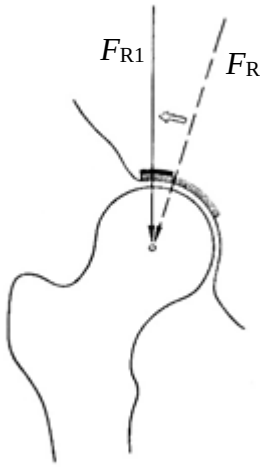


Figure 9. The static resultant force acting on the hip joint during normal human walking (F_R) compared to the static resultant force acting on the hip joint during limping (F_{R1}) [35].

Results of the experiments conducted by Bergmann et al. [36] show that the average resultant force acting on the hip joint during normal human walking is 238% of the human body weight. Experimental results for several different activities [36] are shown in Table 1.

Table 1. Percent of the body weight acting on the hip joint during several normal human activities.

Activity	% of the body weight
Slow walking	242
Normal walking	238
Fast walking	250
Up stairs	251
Down stairs	260
Standing up	190
Sitting down	156
Knee bend	143

2.2. Common causes of hip joint pain and hip replacement surgery

The most common cause of chronical pain and reduced hip mobility is arthritis. Osteoarthritis, rheumatoid arthritis and post-traumatic arthritis are the most common types of arthritis. Osteoarthritis is a type of arthritis where articular cartilage is worn out and there is a direct contact between the femoral head and the acetabulum. This type of arthritis is common for older people. Rheumatoid arthritis is an autoimmune disorder where synovial membrane is thickened and inflamed, which causes cartilage damage. Post-traumatic arthritis is caused by an injury of the joint. Avascular necrosis or osteonecrosis of the hip joint is caused by injuries of the hip joint such as dislocation or fracture, which decreases blood supply in the femoral head. Decreased blood supply causes bone tissue damage and therefore joint surface damage. All of the above described diseases lead to pain and decreased mobility of the hip joint, which makes even the simplest movements such as sitting down and walking painful and difficult. If the medication does not help, the most effective solution for pain relief is the hip replacement surgery.

Besides the traditional hip replacement surgery, minimally invasive approach has become common. In this approach soft tissue damage necessary to access the hip joint and the blood loss during the surgery are reduced to minimum and the recovery time is shorter than after the traditional surgery. In case of minimally invasive surgery, one or two smaller incisions are made instead of one long incision and CAS (Computer-assisted surgery) technology usage is recommended. This technology enables the surgeon to increase the accuracy of components positioning by displaying the location of the surgical instrument on a screen and that way it decreases the possibility of the prosthesis dislocation. The biggest defect of CAS technology is the high price of the equipment.

3. HIP PROSTHESIS

First successful hip prosthesis, similar to prostheses that are still in use, was made in 1960s. It consisted of metal femoral component, polyethylene acetabular component and it was fixated in the bone cement. Since then, there has been a big improvement in technology, surgical procedures, materials and equipment, which lead to improved hip replacement surgeries.

3.1. Classifications of hip prostheses

The main hip prostheses classification divides them into total hip prostheses and partial hip prostheses. Partial hip prosthesis replaces only the damaged part of the joint, which is usually the femoral head and it is used in cases of fracture of the bone. Total hip prosthesis replaces both hip joint bodies: femoral head and acetabulum.

Prostheses can also be monolithic, where they are made out of one part, and modular, where they consist of several components that need to be assembled during the surgery. Monolithic prostheses are usually cheaper and less prone to corrosion, while modular prostheses enable adjustment of the components during the surgery and make potential revision surgeries easier by enabling the replacement of only the damaged part of the prosthesis.

3.1.1. Total hip prosthesis

Total hip prosthesis, as shown in Figure 10. Total hip prosthesis, replaces both hip joint bodies. Two main components of the total hip prosthesis are the femoral component and the acetabular component. Femoral component consists of the head that is usually ceramic or metal, the neck and the stem (shaft) which are made of metal, while the acetabular component consists of the acetabular cup which is usually made of metal or polyethylene and the liner which is usually polyethylene or ceramic.

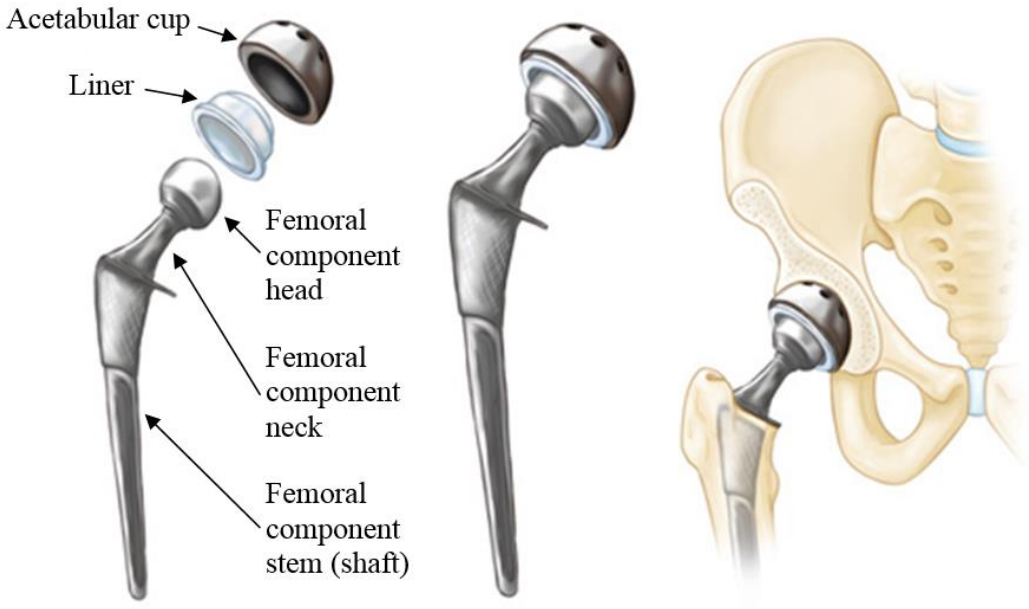


Figure 10. Total hip prosthesis [42]

The most commonly used material combination for total hip prostheses are metal head of the femoral component and polyethylene acetabular cup, but there are several other possible material combinations:

- Ceramics-polyethylene: the femoral component head is made of ceramics and the acetabular cup is made of polyethylene or it has a polyethylene coating. The most commonly used polyethylene material for this purpose is UHMWPE (ultra-high-molecular-weight-polyethylene).
- Metal-metal: both the femoral component head and the acetabular cup are made of metal.
- Ceramics-metal: the femoral component head is made of ceramics and the acetabular cup is made of metal.
- Ceramics-ceramics: the femoral component head and the acetabular cup are both ceramic. This type of prostheses have high hardness and very low friction factor, but they need to have smaller femoral component head diameter [43], which increases the possibility of prosthesis dislocation.

Femoral component stem (shaft) is usually made of titanium alloy or chrome-cobalt alloy. These two materials are the most appropriate for the prostheses because of its high biocompatibility and mechanical properties more similar to the bone than the other used materials. Total hip prostheses are usually cast or forged.

3.1.1.1. Fixation of total hip prosthesis

By the way of fixation, hip prostheses can be cemented, cementless or hybrid. Cemented hip prostheses are fixed inside the bone by using bone cement. Bone cement is a made of poly(methyl methacrylate) (PMMA), which is delivered to surgeons as a liquid in a sealed glass ampule and a powder in a bag. As soon as the liquid and the powder are mixed together, polymerisation process begins. For that reason, the liquid and the powder are mixed together during the surgery and placed into previously prepared femoral canal. Femoral stem is then inserted into the cement. The biggest deficiency of this type of fixation is the low mechanical properties of the cement, which in time becomes damaged.

Cementless prostheses have direct contact with the femur. In this case, the prosthesis is fixed after the bone grows into the porosities of the rough femoral stem surface. This type of prostheses usually have longer femoral component stem than the cemented prostheses and the recovery after the surgery is longer. Cementless prostheses usually have rougher surface than the cemented prostheses.

Hybrid prostheses have one cementless fixated component and one component fixated by the bone cement. The femoral component is usually cemented and the acetabular cup is usually cementless. This type of fixation is usually applied when the patient is young and active because the acetabulum bone loss is lower than for completely cemented prosthesis.

3.1.2. Partial hip prosthesis

Partial hip prostheses replace only the damaged hip joint body, which is usually the femoral head after fracture of the femur. In this case, the replaced femoral head moves inside the natural acetabulum. The biggest deficiency of this type of prosthesis is the high possibility of the cartilage damage due to pressure from the metal surface of the femoral component head. Partial hip prosthesis can be implanted only to patients who have completely healthy cartilage. The surgery in this case lasts shorter and the blood loss is lower than in the case of total hip arthroplasty.

3.1.3. Hip resurfacing

In hip resurfacing, only the damaged part of the hip joint is replaced. Cartilage is removed and both joint surfaces are coated with metal. Cartilage inside the acetabulum is replaced by a metal shell and the femoral head is trimmed and covered with a metal coating. Hip resurfacing is usually done to younger patients who have healthy bone tissue. Considering the fact that only a small part of the bones is removed, the size of the femoral head and the acetabulum after this procedure is almost the same as the natural femoral head and acetabulum size so the possibility of dislocation is very low. However, the possibility of femoral neck fracture increases after this procedure, which means that the patients with resurfaced hip joint will eventually have to go through another procedure to replace the resurfaced hip joint with a total hip prosthesis.

4. 3D SCANNING

3D scanning was performed using the optical scanner Advanced TOpometric Sensor (ATOS) and GOM Inspect 2016 software. In order to achieve the needed accuracy, it was necessary to carry out a proper calibration prior to the scanning. The calibration was conducted by using the calibration board, through sequential scanning of 18 characteristic points, as shown in Figure 8a. Before the prosthesis scanning, the specimen was cleaned and the polished surface of the prosthesis head was covered by a titanium dioxide and alcohol solution in order to avoid the double reflection during the scanning process. The prosthesis surface was provided with reference point markers, as shown in Figure 11b. Reference point markers are needed and important for the proper alignment of the sequential scans after the scanning process [4].



(a) **(b)**

Figure 11. (a) Calibration process; (b) sample of the prosthesis with reference point markers.

After the scanner calibration and the specimen preparation, the specimen was fixed on the rotation table by a clamping device, as shown in Figure 12, in order to prevent the movement during the scanning process. To generate the complete geometry of a complex object, individual scans from different angles need to be merged into a single data set. During the

scanning, the rotation table with the specimen was sequentially rotated by 45° eight times, taking scans each time. Every two subsequent scans were aligned by using three manually selected reference points visible in both scans. The described steps were repeated until all the scans were correctly aligned and merged together into a single data set. By using the described procedure a point cloud in STL format was obtained, as can be seen in Figure 10a. The obtained STL file was imported into Geomagic Design X software, in which a CAD model of the prosthesis was built. The obtained CAD model is shown in Figure 13b. The geometry of the head was built based on the curvature of the part of the surface visible in the point cloud, which can be seen in Figure 13a.

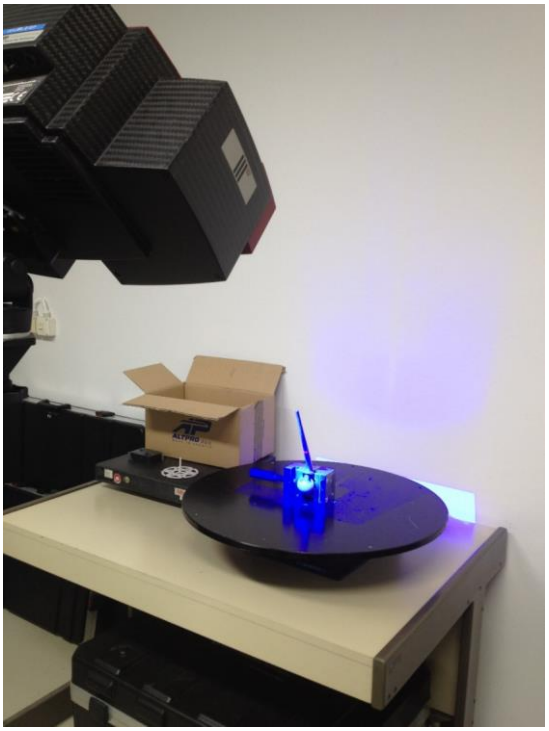
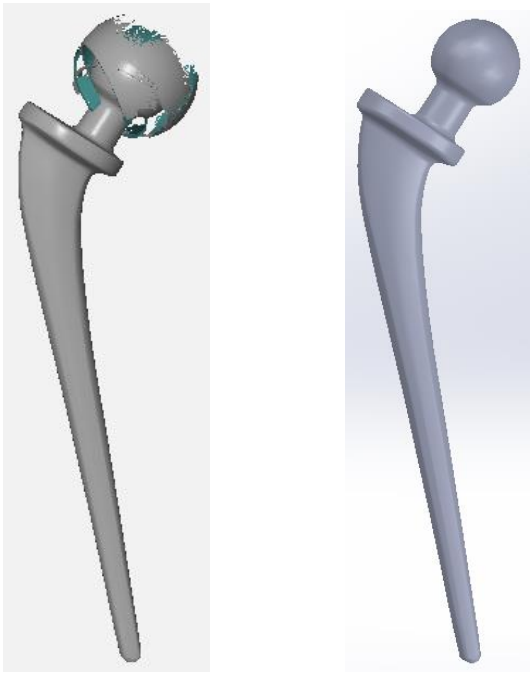


Figure 12. 3D scanning process.



(a) **(b)**

Figure 13. (a) The obtained point cloud; (b) CAD model built based on the point cloud.

5. FINITE ELEMENT MODEL AND ANALYSIS

The CAD model of the prosthesis femoral component reconstructed geometry obtained by the scanning procedure was used as a base to create a FEM model by means of Abaqus software. As a result of 3D scanning, some imperfections occurred in the CAD model built in Geomagic Design X software at sites of geometrical discontinuities of the prosthesis. These imperfections include small faces and edges. The small features may constrain the generation of the mesh, resulting in a poor mesh or a finer mesh density. The poor conditioned geometry was repaired by using the Virtual Topology toolset, Abaqus software [44]. In this way, small faces and edges were ignored in order to avoid generating a poor mesh and artificial stress concentration sites.

The aim of this study was to evaluate the endurance properties of the femoral component of the considered prosthesis. Boundary conditions were based on ISO 7206-4 standard. By finite element analysis, stress distribution for a human walking case was calculated and stress concentration sites were located. Number of cycles to failure for the stress value obtained on the stress concentration site was determined using the S-N curve of the considered ASTM F-745 stainless steel.

4.1. Geometry and boundary conditions

The analysed model consists of the three parts: femoral component of the prosthesis, cement mantle and fixture (cortical bone), with the common surfaces tied together, as shown in Figure 15 and Figure 16. The shaft surface of the femoral component model was used to create a corresponding surface inside the cement mantle model. In accordance with the standard, the femoral component shaft was imbedded in a 5 mm thick cement mantle up to 0.4CT, where CT is the distance between the head centre of the femoral component and the most distal part of the prosthesis, as shown in Figure 16b, [2]. Cement mantle was fully tied with the fixture (bone model) and the whole assembly was fixed at the base, as can be seen in Figure 16a.

Tie constraint was used to make all the motions for the assigned pairs of surfaces equal. Slave and master surfaces were needed to be defined to create a tie constraint. Example of the two components tied together is shown in Figure 14.

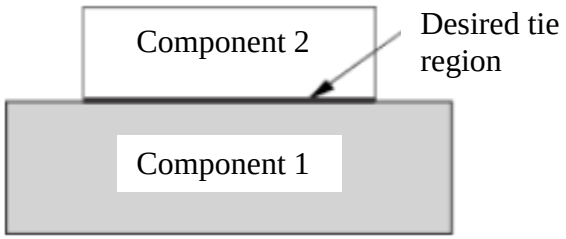
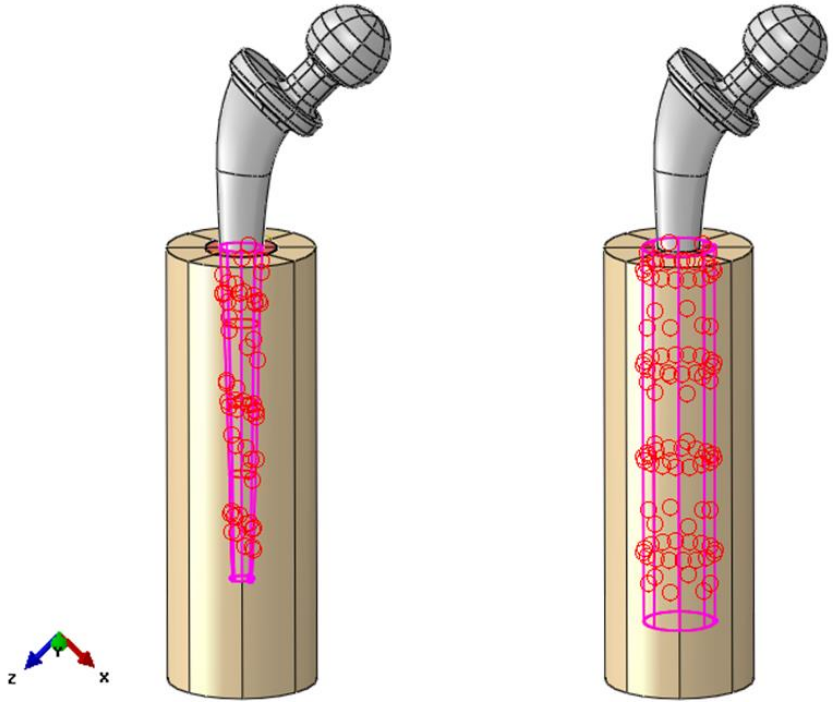


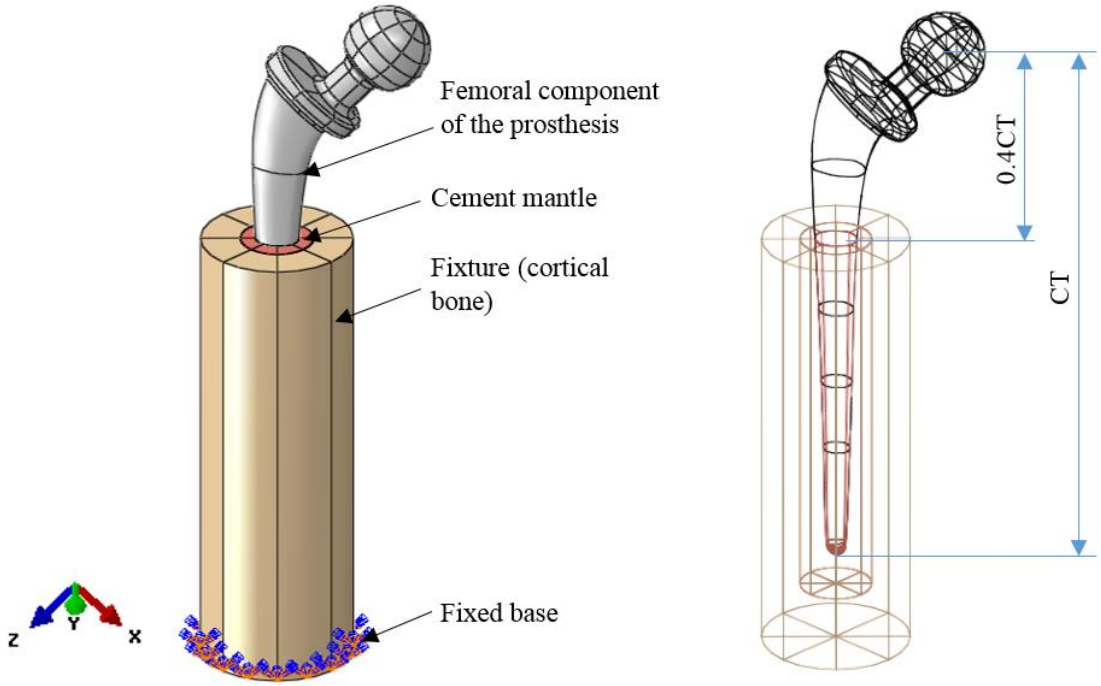
Figure 14. Example of two tied components [44].

For femoral component shaft-cement tie shown in Figure 15a, femoral component shaft with finer mesh was the master surface and the inner surface of the cement mantle was the slave surface. For the cement-fixture (bone) tie shown in Figure 15b, outer surface of the cement mantle that has a finer mesh was the master surface and the inner surface of the fixture mantle was the slave surface. Nodes of the tied surfaces are tied where the slave and master surfaces are close enough to one another. Position tolerance in both tie constraints was set as 0.1 mm, which means that the nodes on the surfaces are tied if the distance between the surfaces is not bigger than 0.1 mm.



(a) **(b)**

Figure 15. (a) Femoral component shaft-cement mantle tie; (b) Cement mantle-fixture (bone) tie.



(a) **(b)**

Figure 16. (a) Fixed base of the assembly; (b) tied surfaces.

4.2. Materials

The considered material of the prosthesis was austenitic stainless steel for cast and solution-annealed surgical implant applications ASTM F-745 (18Cr12.5Ni2.5Mo). The mechanical properties of the considered material are shown in Table 2 [2].

Table 2. Mechanical properties of stainless steel for cast 18Cr12.5Ni2.5Mo.

Mechanical property	18Cr12.5Ni2.5Mo
Elastic modulus (MPa)	205
Poisson's ratio	0.3
Initial yield stress (MPa)	235
Intermediate yield stress (MPa)	502
Maximum yield stress (MPa)	666.82

Cement mantle properties are given in Table 3, as reported in the literature, [2] [5]. Fixture material properties correspond to the properties of cortical bone obtained experimentally and by numerical simulations, as reported by Abdel-Wahab et al. [27] [45] [29]. Young's modulus of cortical bone depends on the bone density [46]. Applied properties of the fixture (cortical bone) for the specified bone density are shown in Table 3.

Table 3. Material properties of the cement mantle and cortical bone.

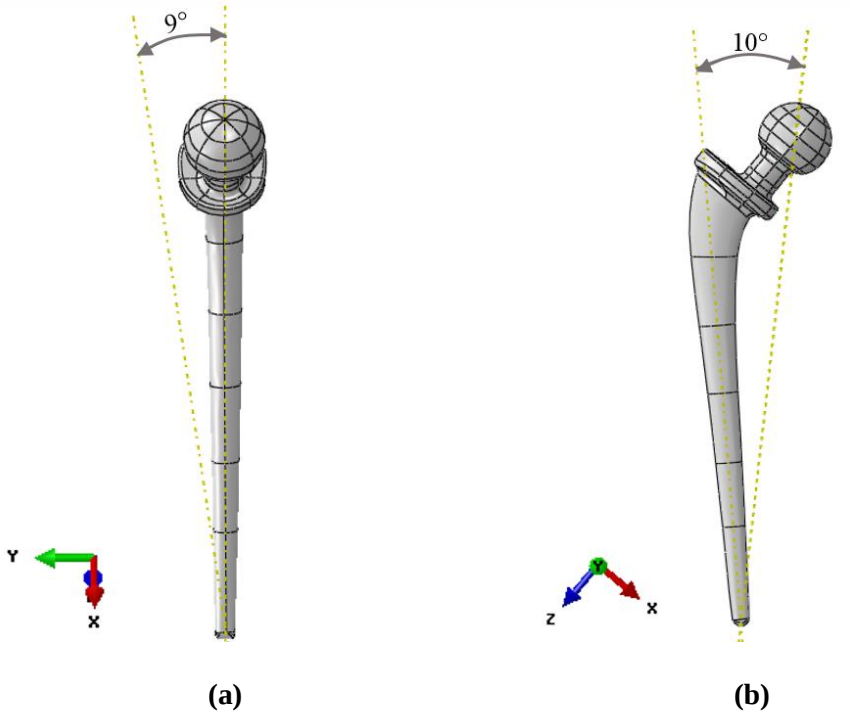
Material property	Cement mantle	Cortical bone
Young's modulus (GPa)	2.3	27.72
Poisson's ratio	0.33	0.44
Density (kg/m^3)	-	1860

4.3. Loading conditions

In time, bonds between femoral bone and the prosthesis femoral shaft may weaken. Performance and success of long-term survival of cemented total hip prosthesis is directly

related to stability of these bonds. Due to femoral component loosening through debonding, the hip prosthesis shaft becomes more exposed to bending, which causes high tensile stresses on the lateral side of the shaft [4]. These high tensile stresses caused by normal human movement can bring to crack initiation at the stress concentration sites and to subsequent crack propagation, which can lead to final fracture of the prosthesis, as reported by Mierzejewska and Oksiuta [25], Griza et al. [2], Hernandez-Rodriguez et al. [24].

Two different loading cases for the total hip prosthesis femoral component were considered. In Case I, loading and boundary conditions were based on fatigue standard ISO 7206-4 testing conditions, which is normally used to evaluate the endurance properties of hip prostheses femoral components, as described by Griza et al. [2]. A load of 2300N was applied at an angle of 9° in flexion and 10° in adduction, relative to the longitudinal axis of the femoral component stem [22], as shown in Figure 17. Here, the loading force acts out of the symmetry plane of the prosthesis, and consequently the prosthesis shaft is exposed to torsion along with bending. In Case II, the load was applied according to the force distribution model given by Ruszkowski et al. [35]. In this case, the load range was based on the measurement results of hip joint loading during normal human activities, as reported by Bergmann et al. [36] [37].



(a) **(b)**

Figure 17. (a) Angle of 9° in flexion; (b) angle of 10° in adduction.

Since the load is transferred from the acetabular cup to the femoral component head, it was applied as a concentrated force F at a point located above the femoral head, located on an axis that passes through the centre of the femoral component head, as shown in Figure 15. To avoid stress concentration, the load was transferred to the whole surface of the femoral head by coupling [44], as can be seen in Figure 18.

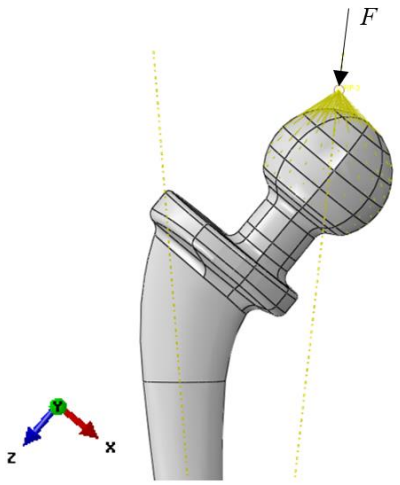


Figure 18. The load applied in Case I

In Case II, the considered load is estimated based on the static resultant force on the hip joint in accordance with the literature [35]. The longitudinal axis of the prosthesis femoral neck and the resultant force F_R during normal walking are closing the angle of 21° [4], as can be seen in Figure 19. According to Bergmann et al., the force on the femoral head during normal walking is 238% of the body weight [36]. In this case, walking of a man with an average body weight of 90 kg was considered. In the FEM model, the concentrated force lays on an axis which closes an angle of 21° with the longitudinal axis of the femoral neck, at a point above the femoral head. In the same way as in Case I, the force was transferred to the whole surface of the femoral head by coupling [44] to avoid the stress concentration. This can be seen in Figure 19.

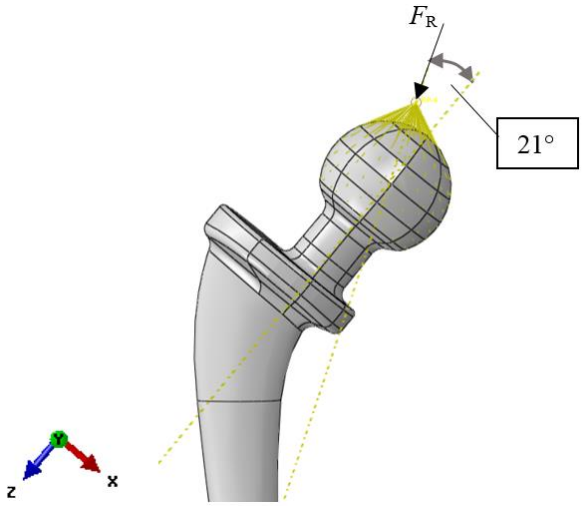


Figure 19. The load applied in Case II.

4.4. Mesh

After defining the interaction (tied surfaces) between the components of the assembly, the boundary conditions and loads, the mesh for the three components was generated, as shown in Figure 21 and Figure 22. Second order tetrahedral elements C3D10 with ten nodes and 30 degrees of freedom, shown in Figure 20, were employed in the finite element analysis. More about C3D10 elements can be found in Abaqus tutorial [44]. Mesh was refined in the region of the prosthesis where stress concentration was expected. Number of elements for each part of the assembly is shown in Table 4.

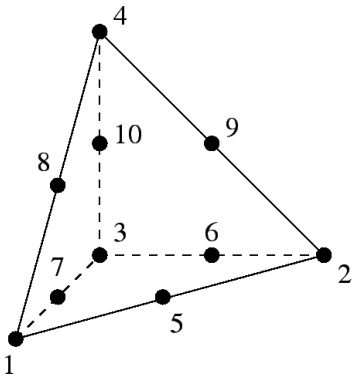
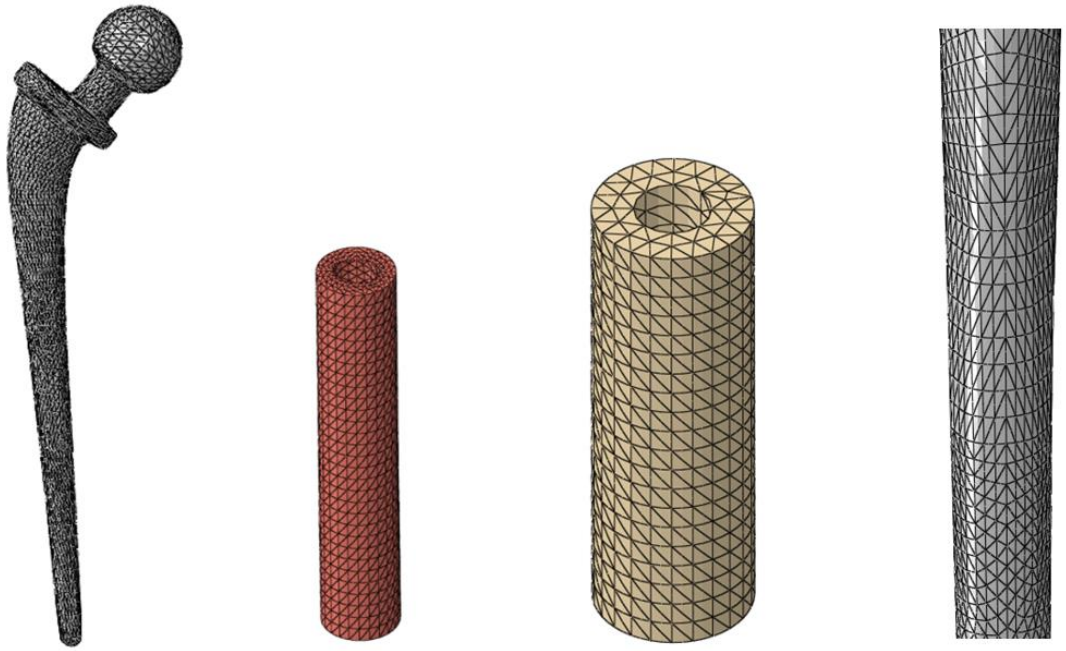


Figure 20. C3D10 element [47].

Table 4. Number of elements for each part of the assembly

Part	Number of elements
Femoral component of the prosthesis	28574
Cement mantle	11099
Fixture (cortical bone)	4321



(a) **(b)** **(c)** **(d)**

Figure 21. (a) Mesh generated on the femoral component; (b) mesh of the cement mantle; (c) mesh of the fixation (bone); (d) detail of the mesh on the expected stress concentration location.

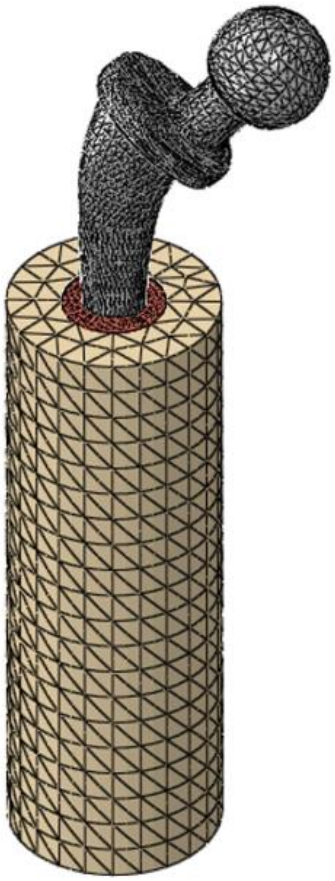


Figure 22. Mesh of the assembly.

6. STRESS CONCENTRATION SITES

One of the aims of this study was to evaluate the endurance properties of the considered prosthesis femoral component for the two loading cases, namely, loads based on the standard ISO 7206-4 and loads due to normal human walking. Stress distribution was determined for the considered load cases. Von Mises stress distribution for both cases for the prosthesis-cement-bone model can be seen in Figure 23. For Case I, Von Mises stress distribution on the femoral component of the prosthesis is shown in Figure 24, while maximum principal stress (absolute) distribution is shown in Figure 25. In this case the loading force acts out of the symmetry plane of the prosthesis, and consequently the maximum tensile stresses are located at the posterior-lateral side of the upper part of the femoral shaft, near the edge of the fixed area, as can be seen in Figure 24a, Figure 25a. This location has been proved to be the crack initiation site in real cases, as reported by Mierzejewska and Oksiuta [25], Griza et al. [2], and Hernandez-Rodriguez et al. [24]. Maximum compressive stresses appeared on the anterior-medial side of the same part of the femoral shaft, as seen in Figures Figure 24c, Figure 25c.

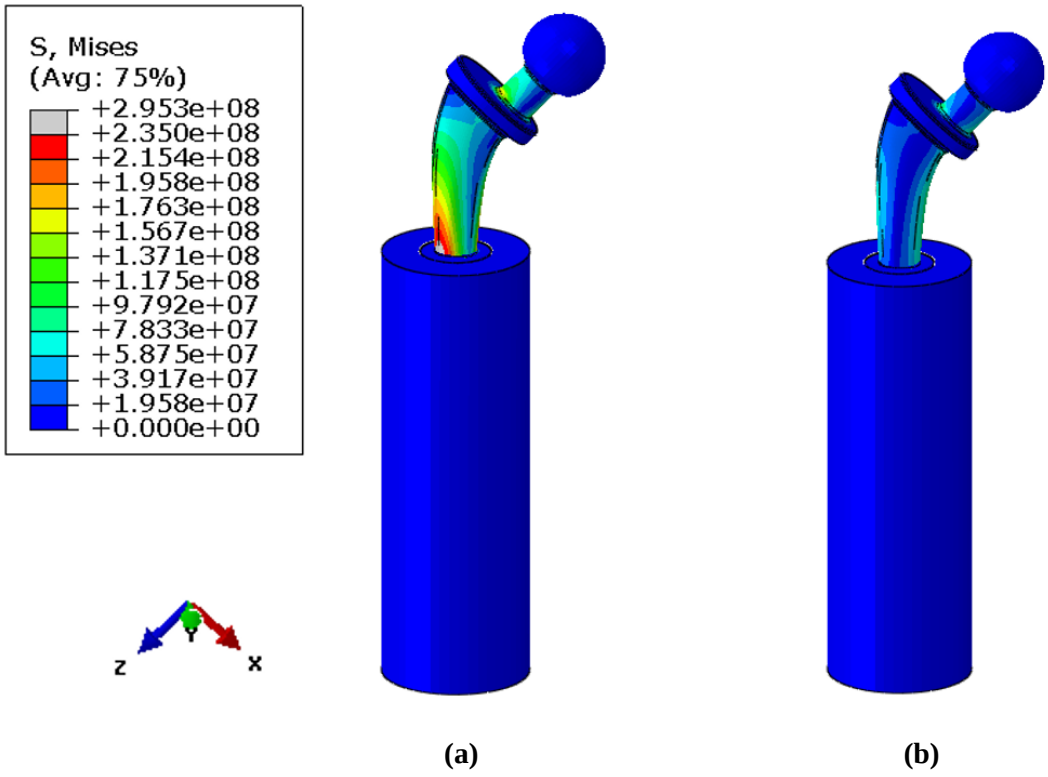


Figure 23. Von Mises stress distribution for the prosthesis-cement-bone assembly: (a) Case I; (b) Case II.

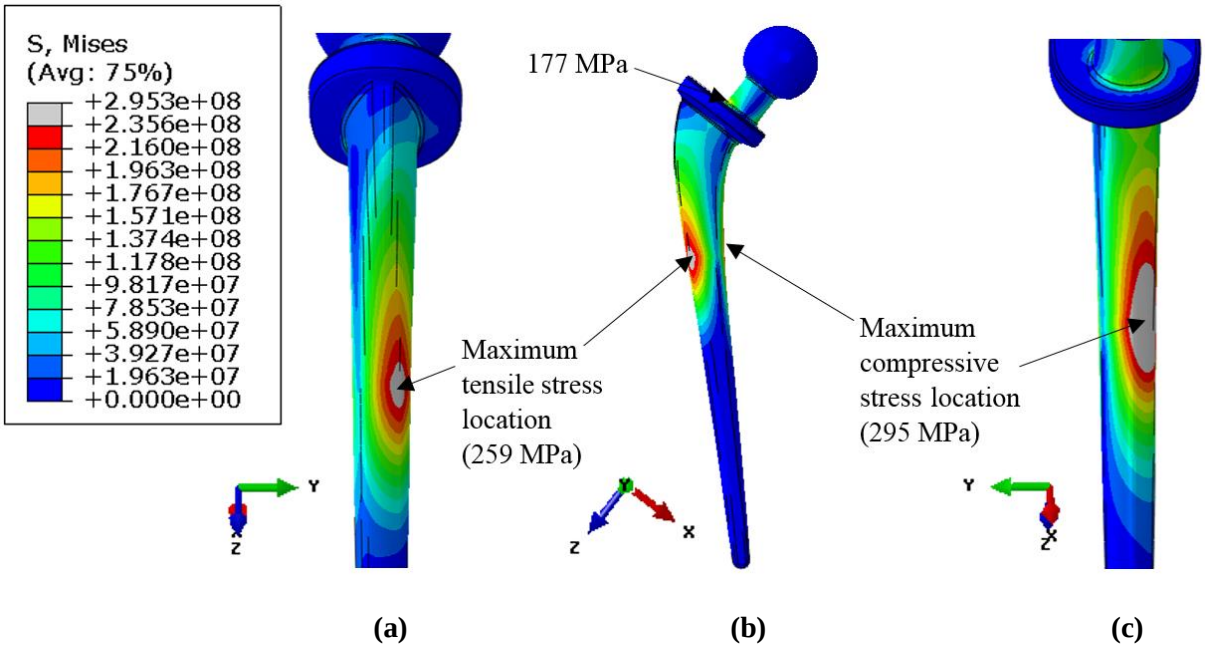


Figure 24. Von Mises stress distribution for Case I (a) stress concentration location on the posterior-lateral side; (b) stress distribution on the femoral component; (c) stress concentration location on the anterior-medial side.

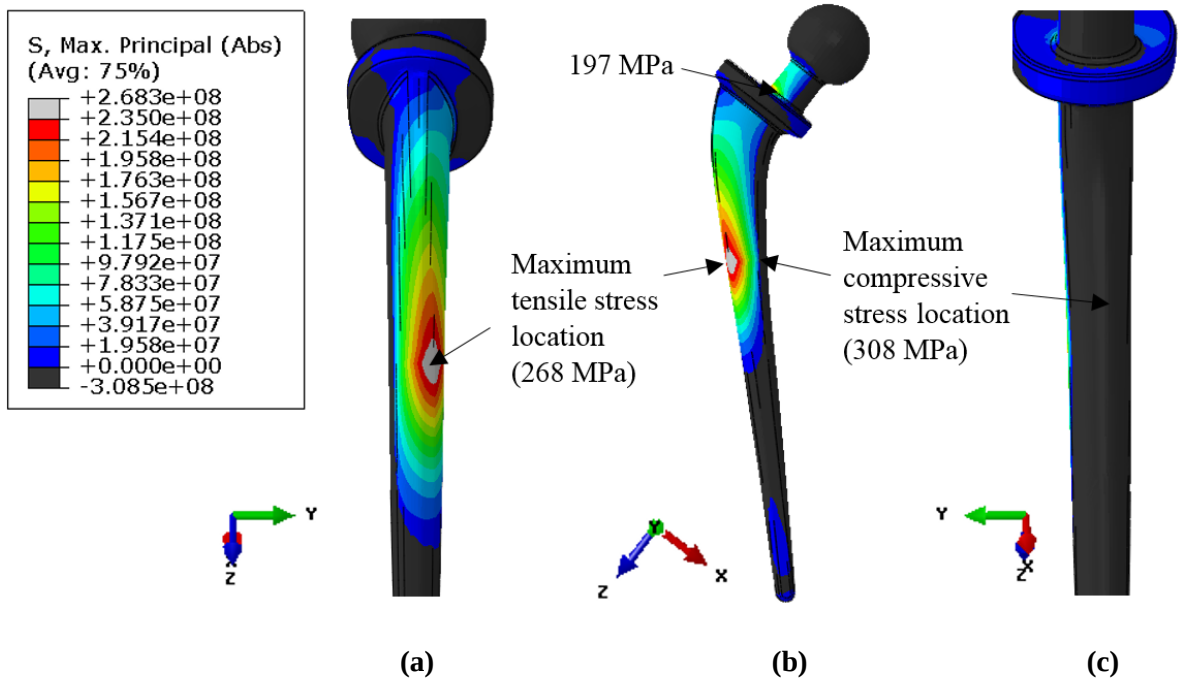
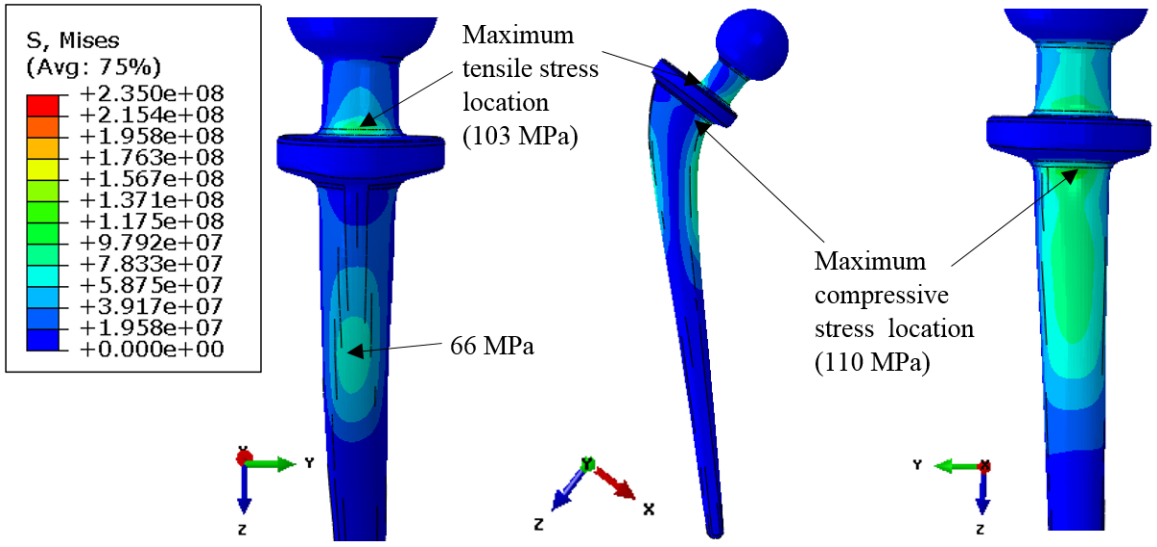


Figure 25. Maximum principal stress (absolute) distribution for Case I (a) stress concentration location on the posterior-lateral side; (b) stress distribution on the femoral component; (c) stress concentration location on the anterior-medial side.

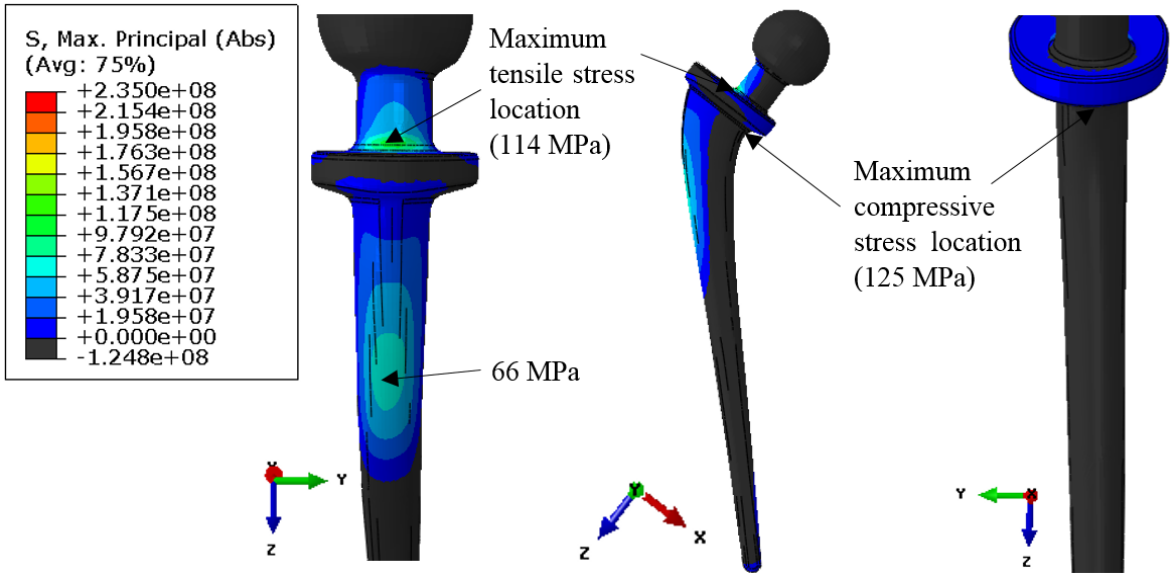
For Case II loading, Von Mises stress distribution on the femoral component is shown in Figure 26b, and maximum principal (absolute) stress distribution is shown in Figure 27b.

Maximum tensile stresses appeared on the lateral side, above the collar of the prosthesis femoral component. Tensile stresses also appear on the lateral side of the femoral shaft, as shown in Figure 26a, Figure 27a, but the stress level is not high. Compressive stresses appeared on the medial side of the femoral shaft, above the fixed area. The highest compressive stress appeared under the collar on the medial side of the femoral shaft, shown in Figure 26c, Figure 27c.



(a) **(b)** **(c)**

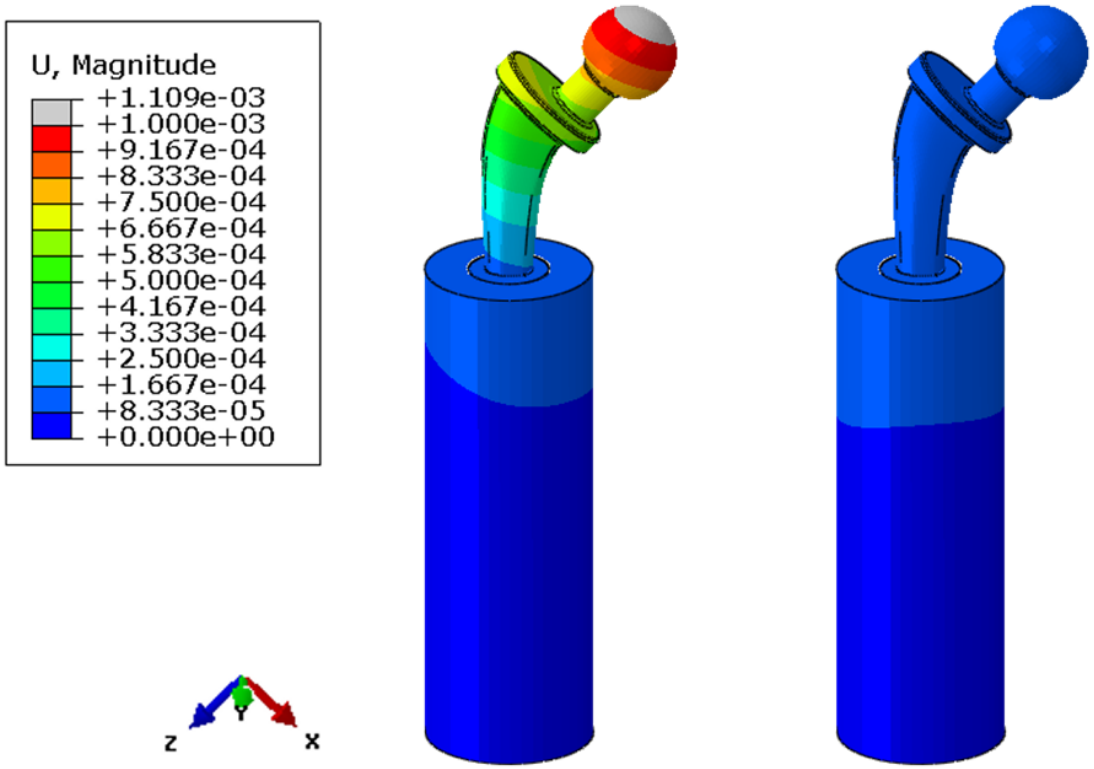
Figure 26. Von Mises stress distribution for Case II (a) stress concentration location on the lateral side; (b) stress distribution on the femoral component; (c) stress concentration location on the medial side.



(a) **(b)** **(c)**

Figure 27. Maximum principal stress (absolute) distribution for Case II (a) stress concentration location on the lateral side; (b) stress distribution on the femoral component; (c) stress concentration location on the medial side.

Displacements for both considered cases are shown in Figure 28 and Figure 29. Figure 28 shows displacements on undeformed shapes and Figure 29 shows displacements on deformed shapes. Displacements are larger in Case I, where the prosthesis is loaded both in flexion and torsion, since the loading force lays out of the symmetry plane of the prosthesis. In addition, the loading force in Case I is more inclined toward the line of gravity and its amplitude is slightly higher compared to Case II, where the loading force lays in the symmetry plane of the prosthesis.



(a) **(b)**

Figure 28. Displacement on undeformed shape: (a) Case I; (b) Case II.

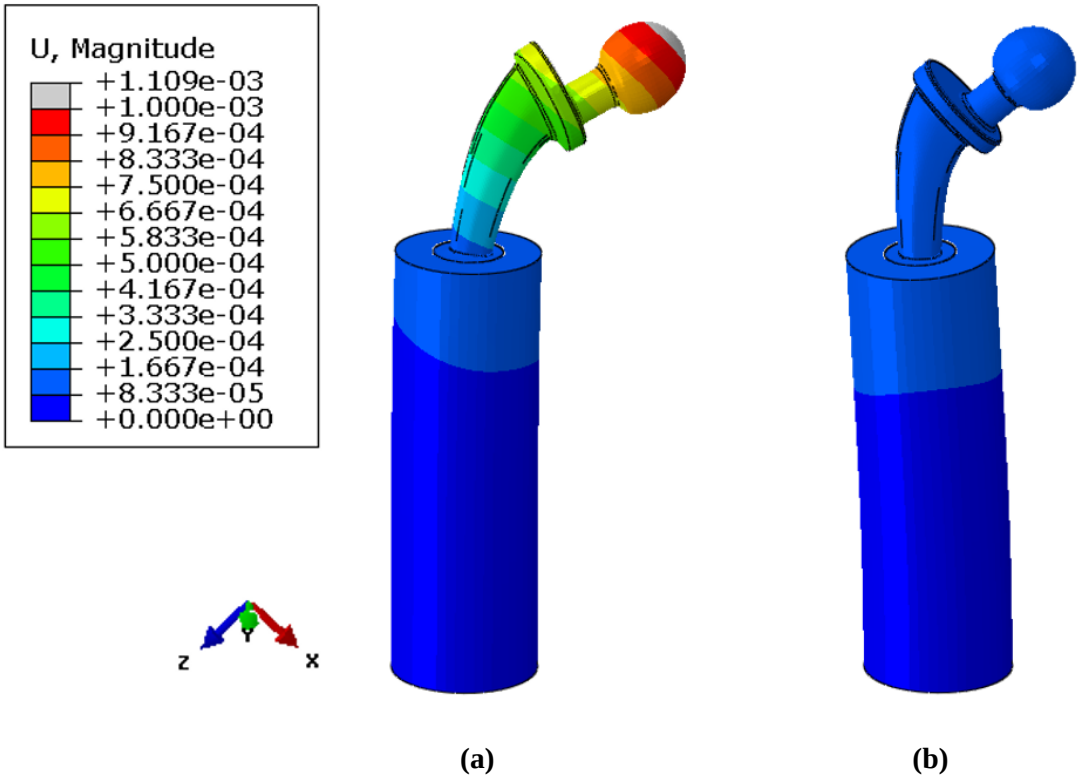


Figure 29. Displacement in both considered cases with deformation scale factor 50: (a) Case I; (b) Case II.

Fatigue cracks occur at tensile stresses locations, according to observations reported by Griza et al. [2], Mierzejewska and Oksiuta [25] and Hernandez-Rodriguez et al. [24]. Therefore, tensile stresses at stress concentration sites are considered in fatigue life assessment of the prosthesis femoral component. Number of cycles to crack initiation for the determined tensile stress values was assessed based on the S-N curve of the considered prosthesis material ASTM F-745, reported by Griza et al. [1] [20], as shown in Figure 30. In Case I, the highest tensile Von Mises stress value of 259 MPa was identified at the posterior-lateral side of the upper part of the femoral shaft. This value is higher than the endurance limit of the considered stainless steel, which ranges between 200 and 250 MPa, [2] [48]. The corresponding number of cycles to crack initiation is 353980, which is about 35% of loading cycles expected in 1 year [20]. However, in reality the component would not go through such strict loading scenario as suggested by ISO 7206-4 [2]. For 90% of the applied force, maximum tensile stress would be 233 MPa and the corresponding number of cycles to crack initiation would be 822355. Above the collar in Case I, maximum tensile Von Mises stress was 177 MPa, for

which the number of cycles to crack initiation would be 7350219. In Case II, the highest tensile Von Mises stress was 103 MPa, which is significantly under the fatigue limit.

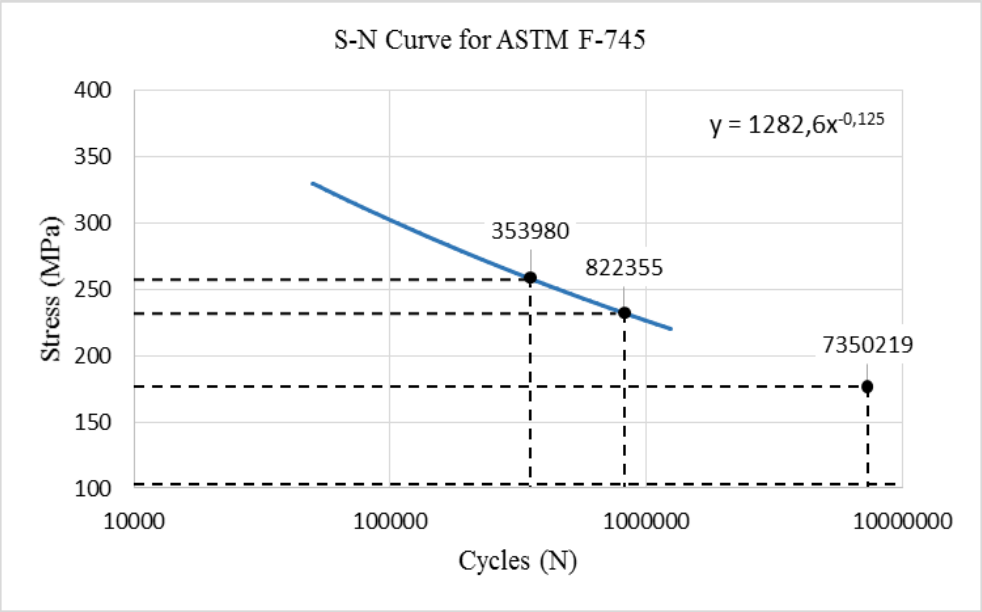


Figure 30. S-N curve of ASTM F-745.

7. FRACTURE MECHANICS

Fracture mechanics studies the behaviour regularities of cracks when a structure is loaded under various conditions, especially for brittle failure creation. Since hip prostheses failure still occurs, the fracture mechanics parameters need to be considered in the prosthesis design. Fracture mechanics explains the crack influence on the condition of the structure so fracture toughness and crack size should be considered as important parameters in structure design. This is shown in Figure 31. Therefore it is necessary to understand the crack initiation and the crack growth phenomena, in order to prevent the possible in vivo fracture of the prosthesis.

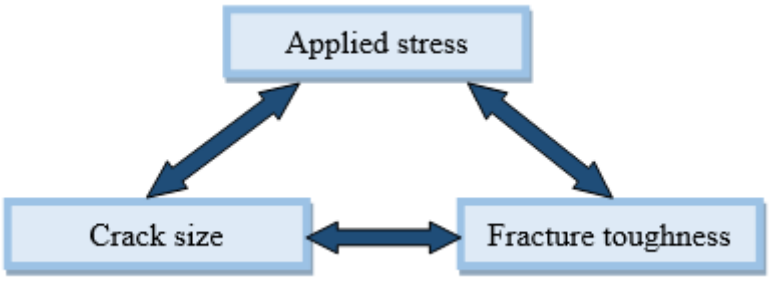


Figure 31. Important parameters in fracture mechanics.

Considering the mechanical behaviour of the material under load, fracture mechanics is divided into:

- linear elastic fracture mechanics (LEFM),
- elastic-plastic fracture mechanics (EPFM).

Linear elastic fracture mechanics (LEFM) assumes that the crack propagates in the elastic state of stress. It is assumed that the material is isotropic and linear elastic and the stress field near the crack tip is calculated using the theory of elasticity. In LEFM, the crack will propagate in unstable manner when the stresses intensity factor reaches its critical value, namely fracture toughness K_{1C}. LEFM is valid only when the inelastic deformation compared to the crack size is small, in case of low fracture toughness. In LEFM, when $\sigma < 0.8\sigma_y$, stress variation is linear to the fracture toughness and the fracture that occurs is brittle. In case of high fracture toughness, there is development of large plastic zones before the crack grows and EPFM has to be used instead of LEFM. If this is the case, ductile fracture occurs. When considering materials with very high fracture toughness value, plastic collapse can occur and

limit load analysis should be used. In cases of dynamic and shock loads, dynamic fracture mechanics is considered. LEFM, EPFM and limit load analysis zones can be seen in the diagram in Figure 32.

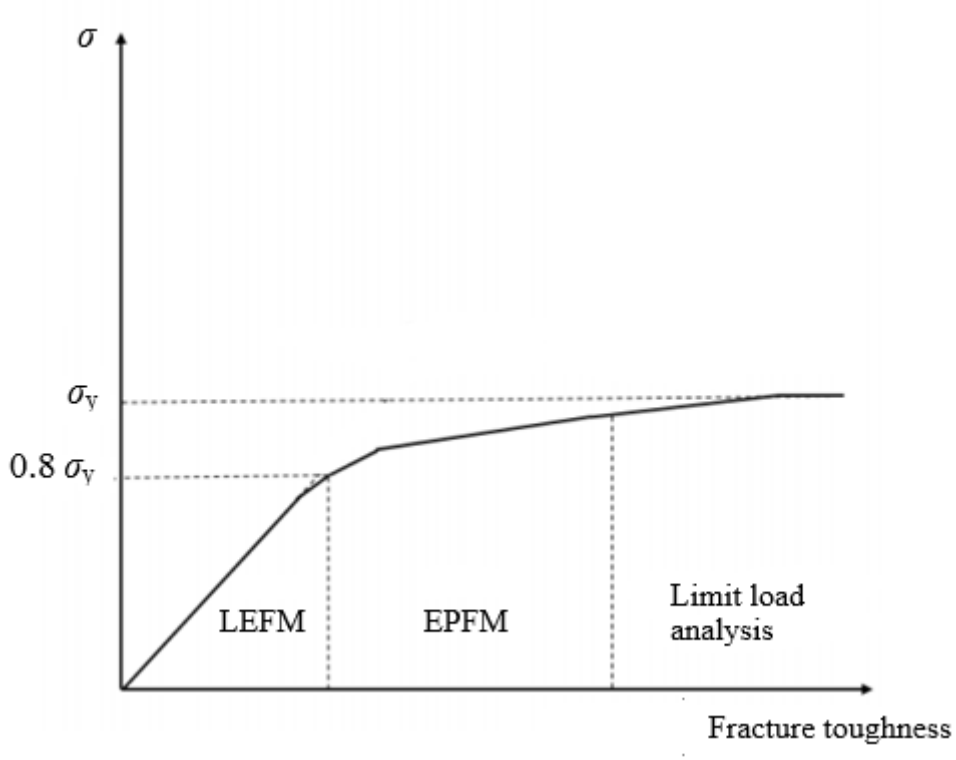


Figure 32. Classification of fracture mechanics.

If the structure is new and does not contain cracks, the strength of the structure is its ultimate strength F_u. When the load acting on the structure exceeds F_u, the structure fails. However, maximum expected work load is F_s and the structure needs to be able to withstand $S*F_s$, where S is safety factor. If the structure contains a crack, its strength decreases to a value below F_u and this strength is called the residual strength. It represents the load that the damaged structure can carry without failing. As the crack grows, the residual strength and the safety factor decrease, as shown in Figure 33. This means that if the structure which contains a crack is not fixed or replaced, in time it will fail.

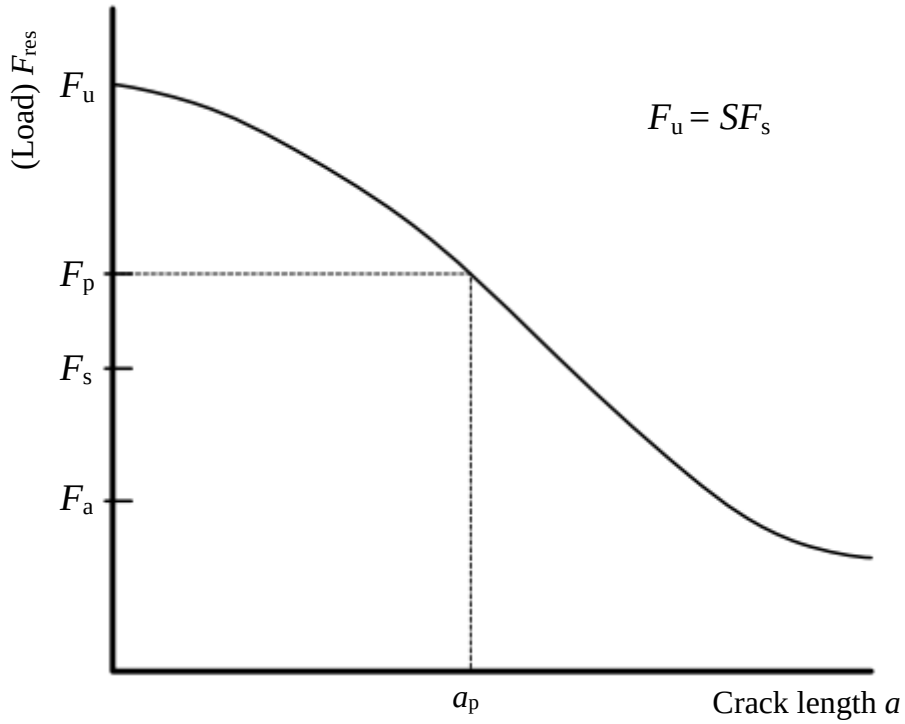


Figure 33. Residual strength diagram (influence of the crack size on the strength) [49].

If the residual strength diagram and minimum residual strength F_p are known, maximum crack length can be determined from the diagram. However, the crack tip events are caused by the local stresses at the crack tip and describing the local crack tip stress as a function of the applied stress is required. For this reason, residual strength diagram can be based on the stress that the structure can withstand without failing, as shown in Figure 34.

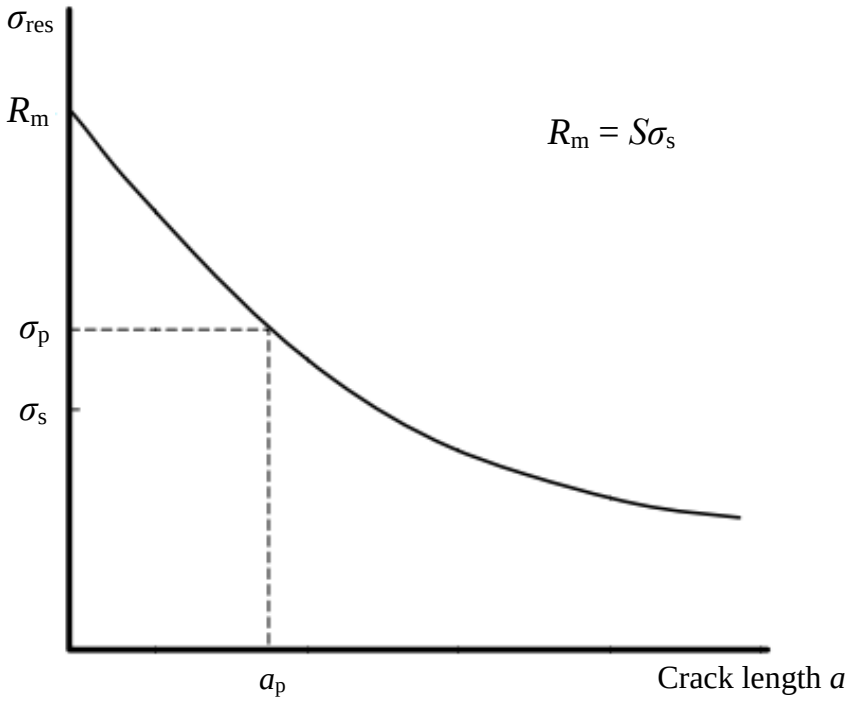


Figure 34. Residual strength diagram based on nominal engineering stress [49].

To avoid fracture of structures, in this case total hip prosthesis, it is common to use the numerical simulations for preliminary studies. Conventional FEM can be used for determining fracture mechanics parameters and simulating crack propagation in biomedical components with complex geometry. It is also necessary to use the appropriate biomaterial with high resistance to crack initiation and the appropriate component design in order to minimize the possibility of crack initiation due to design or inadequate structure of the material. After hip replacement surgery, regular check-ups are recommended to the patients. If any damage on the prosthesis is noticed, it is important to replace it before failure occurs.

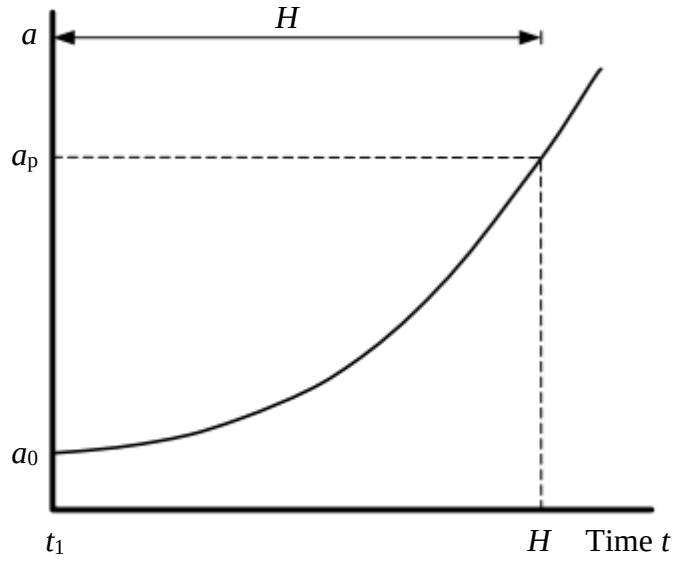


Figure 35. Crack propagation in time [49].

Maximum crack length a_p determined in the residual strength diagram can be seen in the diagram of crack propagation in time. This way it is possible to determine time *H* after which the damaged structure or component needs to be replaced.

The most common mechanisms of crack growth are

- fatigue caused by cyclic loading,
- stress corrosion caused by sustained loading and

Less common mechanisms of crack propagation are

- creep,
- hydrogen induced cracking and
- liquid metal induced cracking.

Besides fatigue and stress corrosion, combinations of those two mechanisms are also a common event [50]. Fatigue cracks, even in case they are caused by small load range, contain plastic deformation at the crack tip due to high stress concentration. The plastic deformation occurs as slip of atomic planes due to shear loads. This causes crack tip blunting and a small crack extension Δa. Due to unloading, the crack tip sharpens and the cycle repeats. Fatigue crack growth process is shown in Figure 36.

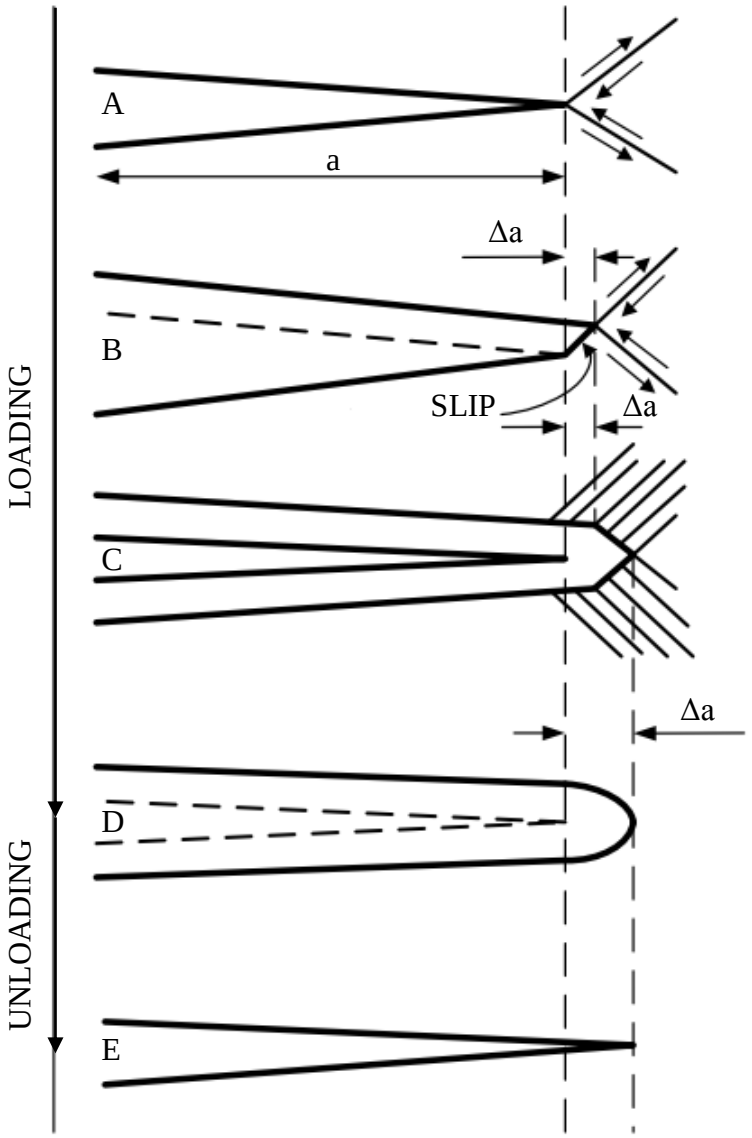


Figure 36. Fatigue crack growth mechanism [51].

Because of the repeated blunting and sharpening of the crack tip, marks of crack propagation, called fatigue striations, can be seen under the microscope, as can be seen in Figure 2 and Figure 37. Fatigue crack propagation is a slow process. Growth per cycle is usually in order of 10^{-7}-10^{-3}, but it becomes significant after a high number of cycles [50]. This process is irreversible due to oxidation of the material exposed along the slip steps and general disorder caused by the slip [50].

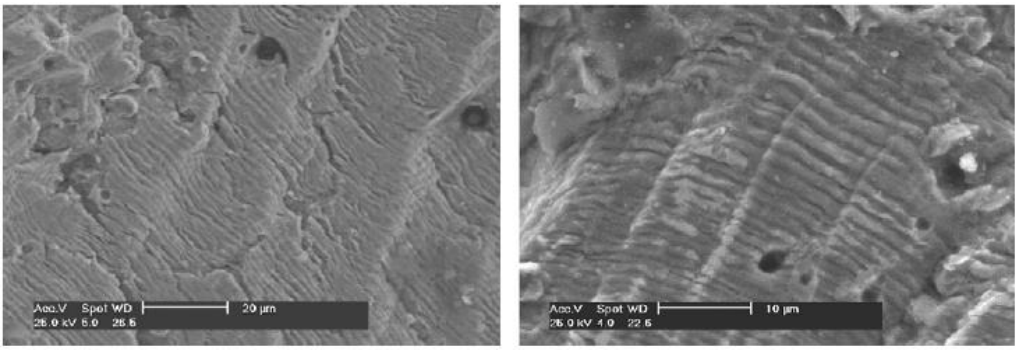


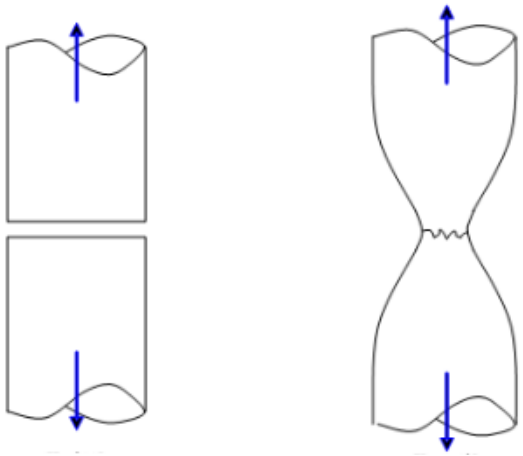
Figure 37. Microscopic view of fatigue striation on the failed femoral component shaft [2].

Stress corrosion induced crack growth is also a slow process. The high stretch causes atomic disarray at the crack tip, which causes corrosion, often along the grain boundaries. Creep cracking mechanism is usually the diffusion of vacancies (open atomic places). More open atomic places connect and form a hole which then connects to the crack tip.

Crack is only a partial failure, but in time it can lead to total failure by fracture. Fracture can occur by only two mechanisms:

- cleavage (brittle fracture), where fracture occurs with little or no plastic deformation and it is characteristic for low fracture toughness materials, as shown in Figure 38a,
- rupture (ductile fracture), where fracture occurs with plastic deformation and it is characteristic for high fracture toughness materials, as shown in Figure 38b.

The third mechanism, intergranular fracture, requires some form of cleavage or rupture.



(a) **(b)**

Figure 38. Fracture example: (a) brittle; (b) ductile [52].

Cleavage (brittle fracture) happens when atomic planes split apart. The preferred splitting plane is oriented differently from grain to grain and this causes fracture, which causes faceted fracture, as shown in Figure 39. The facets are flat, which makes them good incident light reflectors so the fracture sparkles when it occurs but soon it fades due to oxidation [50].

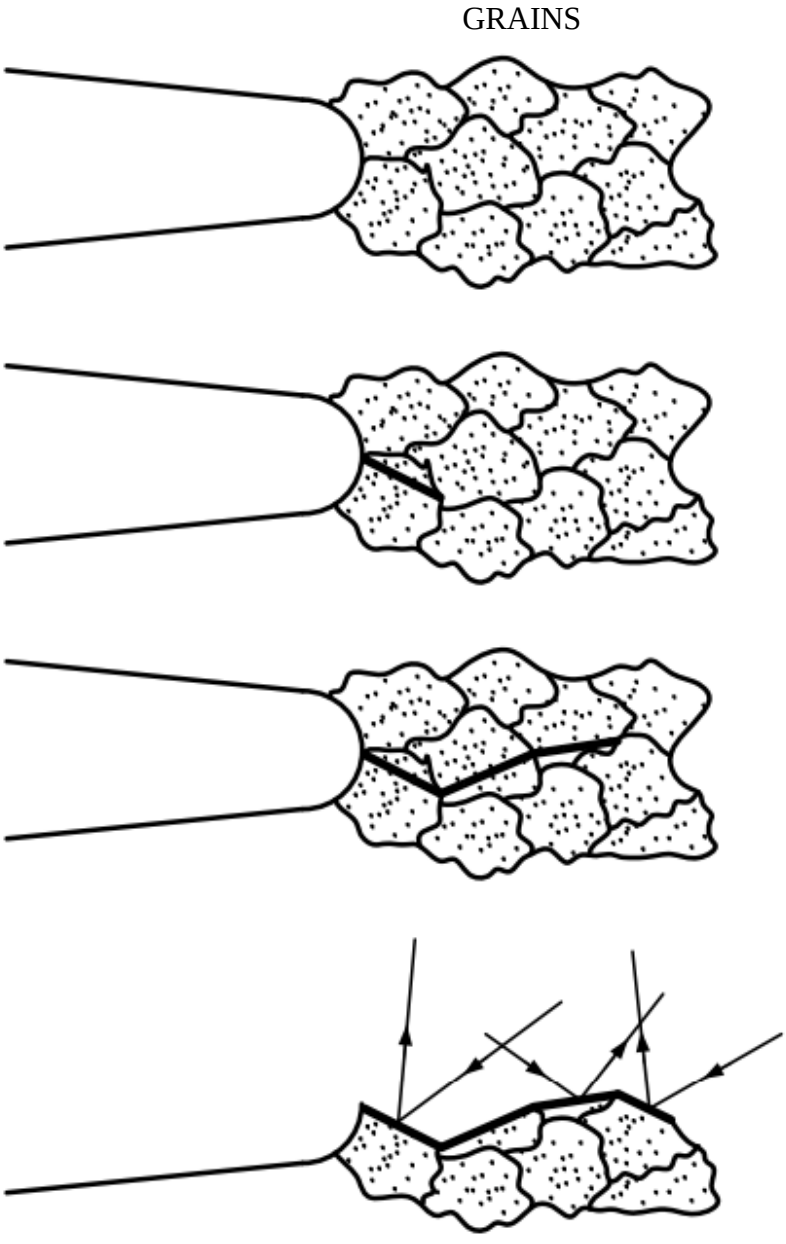


Figure 39. Brittle fracture (cleavage mechanism) at the blunted crack tip. Bottom: incident light reflection on the facets [51].

In case of rupture (ductile fracture), particles and inclusions in the material play an important role. They are usually complex compounds of alloying elements. Some of these elements

improve machineability and castability and others improve the strength of the alloy. The large particles get loose or break, which causes forming of widely spaced holes near the crack tip. After that, holes are formed at the smaller particles and then they join up and complete the fracture. This process is shown in Figure 40. Unlike the fracture surface after the cleavage fracture, the fracture surface in this case is irregular so it diffuses the light and looks grey [50]. By heat treatment or selective alloying, large particles can be eliminated and this way fracture resistance of an alloy can be improved. However, to provide strength, alloying is necessary so not all particles can be avoided [50]. Both of the mechanisms, cleavage and rupture, are fast processes. Fracturing is sometimes stable, but in this case it is usually followed by the final unstable event.

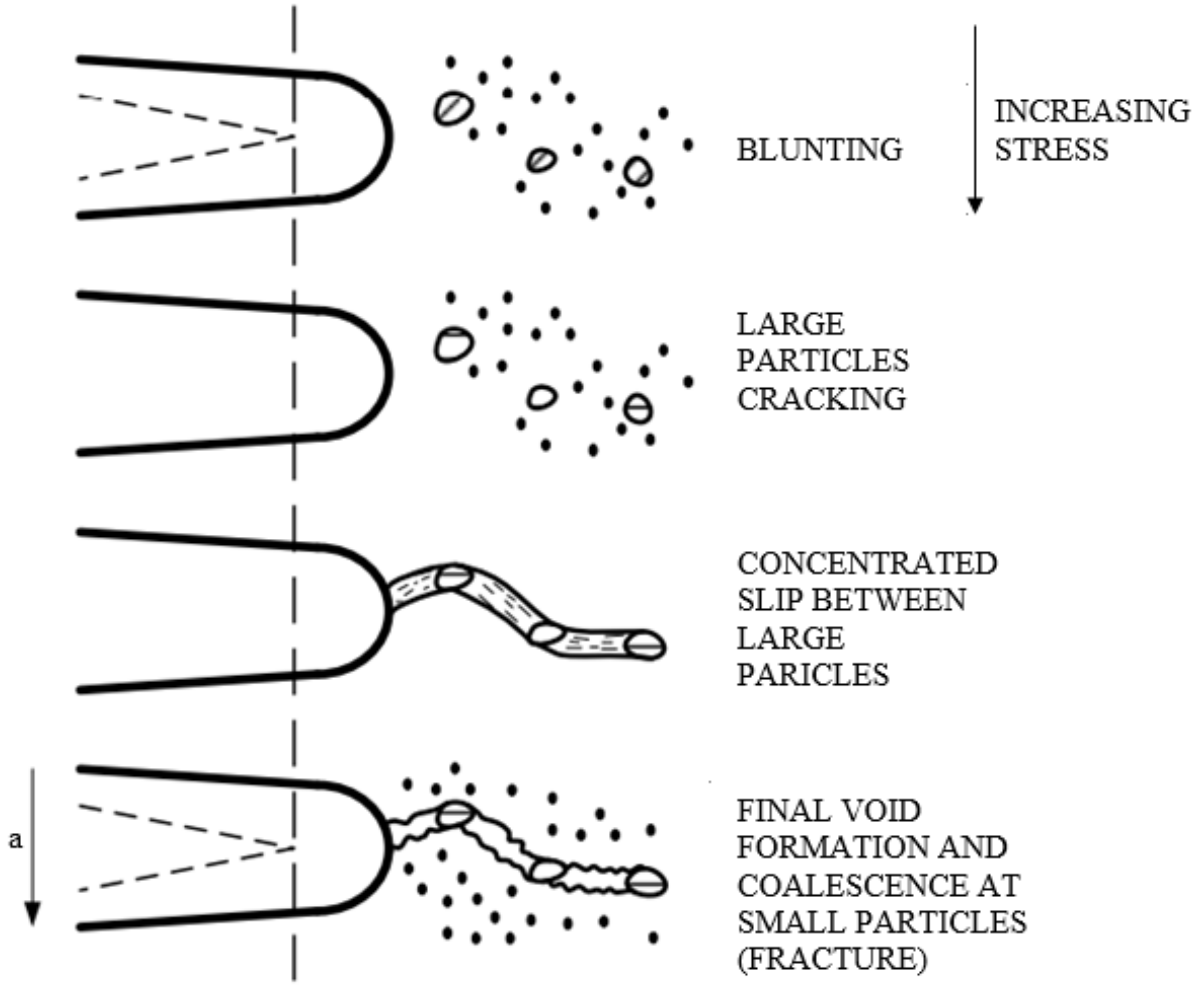
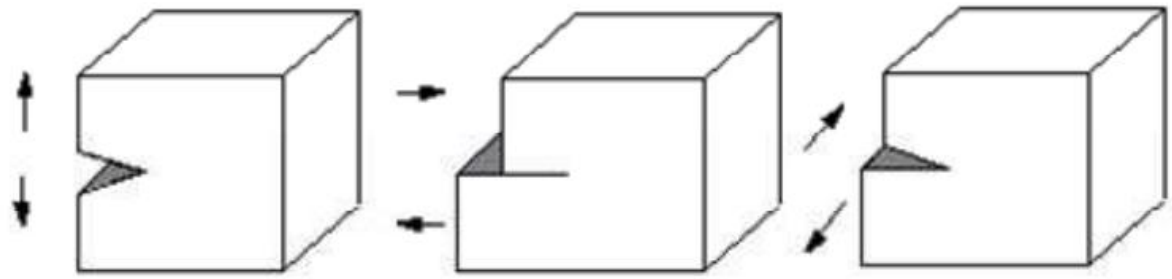


Figure 40. Stages of rupture (ductile fracture) [51].

Depending on the way of applying load to enable crack propagation, there are three fracture modes, as shown in Figure 41. Mode I fracture (Opening mode) happens due to applying a

tensile stress normal to the crack plane. Mode II (Sliding mode or In-plane shear) happens due to applying a shear stress parallel to the crack plane and perpendicular to the crack front. Mode III (Out-of-plane shear or tearing mode) happens due to applying a shear stress parallel to the plane of the crack and to the crack front. Mode II and Mode III always occur in combination in Mode I fracture.



(a) **(b)** **(c)**

Figure 41. Fracture modes: (a) Mode I (Opening mode); (b) Mode II (In-plane shear); (c) Mode III (Out-of-plane shear) [51].

7.1. Linear elastic fracture mechanics

7.1.2. Stress at the crack tip

Consider an arbitrary shaped body, as shown in Figure 42, that contains an arbitrary size of the crack, subjected to arbitrary load (bending, tension or both), as long as it is Mode I loading. The considered material is assumed to be elastic and follows Hooke's law. In this case theory of elasticity can be used to determine the stress state field at the crack tip.

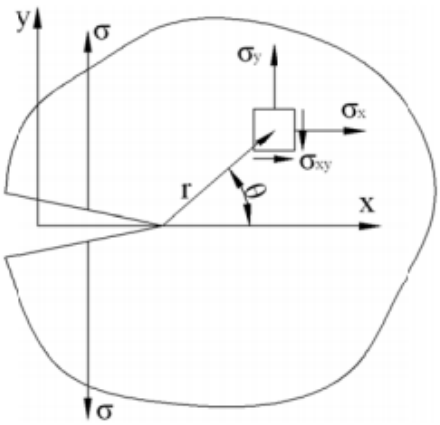


Figure 42. Stress at the crack tip [49].

Stress field at the crack tip can be described by the following equations [49]:

$$\sigma_x = \frac{K_I}{\sqrt{2\pi r}} \cos\frac{\theta}{2}\left(1 - \sin\frac{\theta}{2}\sin\frac{3\theta}{2}\right), \quad \textbf{(1)}$$

$$\sigma_y = \frac{K_I}{\sqrt{2\pi r}} \cos\frac{\theta}{2}\left(1 + \sin\frac{\theta}{2}\sin\frac{3\theta}{2}\right), \quad \textbf{(2)}$$

$$\tau_{xy} = \frac{K_I}{\sqrt{2\pi r}} \sin\frac{\theta}{2}\cos\frac{\theta}{2}\cos\frac{3\theta}{2}, \quad \textbf{(3)}$$

In case of plane through the cracked section ($\theta = 0$, $r = x$), some elements of the equations disappear and the following can be concluded:

$$\sigma_x = \frac{K_I}{\sqrt{2\pi x}}, \quad \textbf{(4)}$$

$$\sigma_y = \frac{K_I}{\sqrt{2\pi x}}. \quad \textbf{(5)}$$

For the plane $y = 0$, it is concluded that stresses σ_x and σ_y have the same value. The stress depends on the distance from the crack tip and the stress intensity factor K which in its index contains the mode (I, II or III).

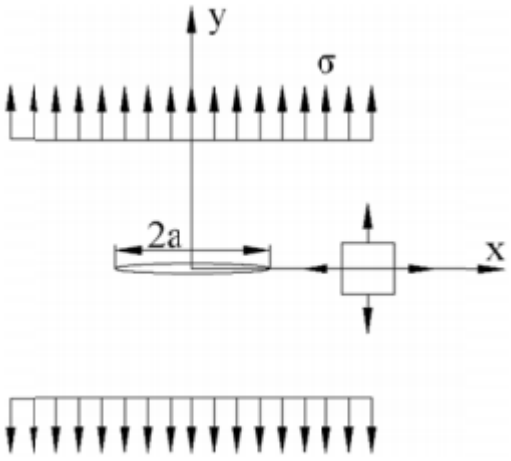


Figure 43. Infinite plate containing a central crack with uniform loading [49].

For the infinite plate with central crack, it can be concluded that the stress at the crack tip will be proportional to the load acting the plate, but it also depends on the crack size and the dimensionless number C. The following can be concluded:

$$\sigma_y = \frac{C\sigma\sqrt{a}}{\sqrt{2\pi x}}. \quad \textbf{(6)}$$

For the infinite plate $C = \sqrt{\pi}$ and the following is concluded:

$$\sigma_y = \frac{\sigma\sqrt{\pi a}}{\sqrt{2\pi x}}. \quad \textbf{(7)}$$

Comparison of Equations (7) and (4) leads to the equation for the stress intensity factor for an infinite plate with a central crack:

$$K = \sigma\sqrt{\pi a}. \quad \textbf{(8)}$$

7.1.3. Stress intensity factor

When a finite plate, as shown in Figure 44 is considered, the dimension of the plate influence the stress field at the crack tip.

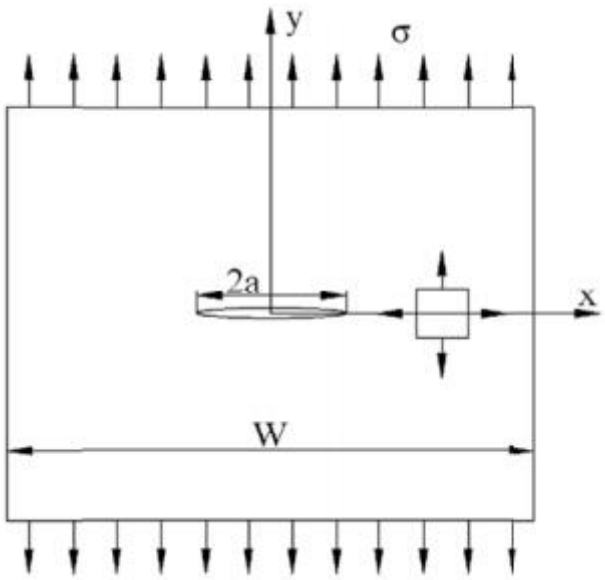


Figure 44. A finite plate containing a central crack with uniform loading [49].

As the dimensions (geometry) of the plate influence the stress field at the crack tip, geometry factor β becomes a part of the equation for determining the stress intensity factor:

$$K = \beta\sigma\sqrt{\pi a}. \quad \textbf{(9)}$$

Equation (9) represents the general form of the stress intensity factor K for a finite plate. Geometry factor β is defined by the plate geometry and for most cases it can be found in the literature.

8. FINITE ELEMENT METHOD IN FRACTURE MECHANICS

Finite element method is based on discretisation of continuum with infinite number of degrees of freedom by using finite element mesh with a limited number of degrees of freedom. Differential equations are replaced by a group of algebraic equations. There is a wide range of element types that can be used in the finite element analyses. When finite element method first started to be used for solving fracture mechanic problems, isoparametric finite elements were used in the analyses. However, they were not appropriate for this use since they could not model the singularities of stresses and strains around the crack tip. As the finite element method and the computers developed, singular finite elements started to be used instead of isoparametric elements for solving fracture mechanic problems.

8.1. Isoparametric finite elements

Considering the fact the Cartesian coordinate system is often not appropriate in cases of complex geometry, Natural coordinate system is used instead of the Cartesian. Natural coordinates are a function of Cartesian coordinates and their values range from zero to one. If the elements are described by local natural coordinates, after their transformation into the global Cartesian system, the regular shapes of the elements become arbitrary (with curved surfaces or edges). Using these kind of elements enables easier modelling of complex geometrical shapes. If the displacement field is described by the same interpolation functions as the element geometry, these elements are called isoparametric finite elements.

8.1.1. Two dimensional rectangular elements

Isoparametric element formulation can easily be explained on the example of transformation of the regular rectangular element into an arbitrary element, as shown in Figure 45.

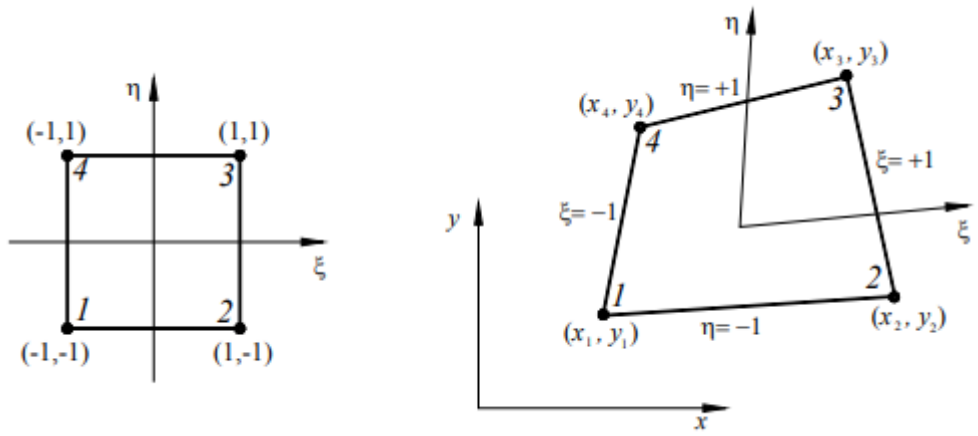


Figure 45. Transformation of a regular rectangular element into an arbitrary element [49].

The geometry of the element can be described by the following equations:

$$x = \sum_{i=1}^{4} N_i(\xi,\eta)x_i, \tag{10}$$

$$y = \sum_{i=1}^{4} N_i(\xi,\eta)y_i. \tag{11}$$

Shape functions are defined by the following equation:

$$N_i(\xi,\eta) = \frac{1}{4}(1+\xi_i\xi)(1+\eta_i\eta). \tag{12}$$

The displacement field can be described by the same shape functions as for the element geometry:

$$u = \sum_{i=1}^{4} N_i(\xi,\eta)u_i, \tag{13}$$

$$v = \sum_{i=1}^{4} N_i(\xi,\eta)v_i. \tag{14}$$

If the original regular geometry element contains several nodes on the edge, the straight edge of the original element can be transformed into a curved edge of the arbitrary element.

8.2. Singular finite elements

Since there is a wide range of applications of finite element method, many types of elements have been developed to describe singularity at the crack tip. The most commonly used method is collapsing one side of the second order isoparametric rectangular element into a

triangular element and moving the midside nodes on the sides connected to the crack tip to a specified point which location depends on the type of singularity.

For the geometry discretisation at the crack tip, singular finite elements (quad elements collapsed to triangular elements) are used around the crack tip and for the discretisation of the rest of the geometry isoparametric finite elements are used. A finite element ring shown in Figure 46 represents the usual discretisation around the crack tip.

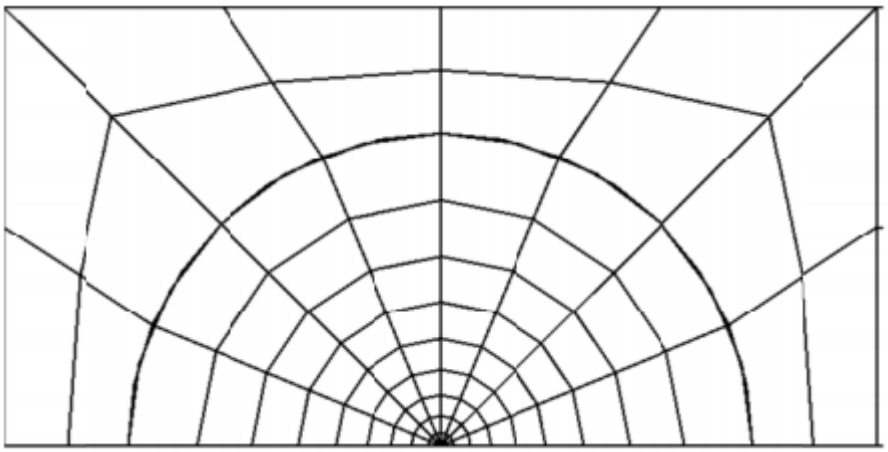


Figure 46. The usual mesh around the crack tip [49].

Depending on the location of the midside node, there are different types of singularity in order to enable solving linear elastic and elastic plastic fracture mechanics. Types of the material models are:

- Linear elastic material model,
- Elastic-ideally plastic material model,
- Elastic plastic material model.

Type of the material model determines the type of the singular elements used in the analysis.

8.2.1. Singular elements for solving linear elastic problems

If the material is linear elastic, one side of the quadratic element is collapsed into one node which represents the crack tip. Midside nodes on the sides connected to the crack tip are moved to the 0.25 point nearest the crack tip, as shown in Figure 47.

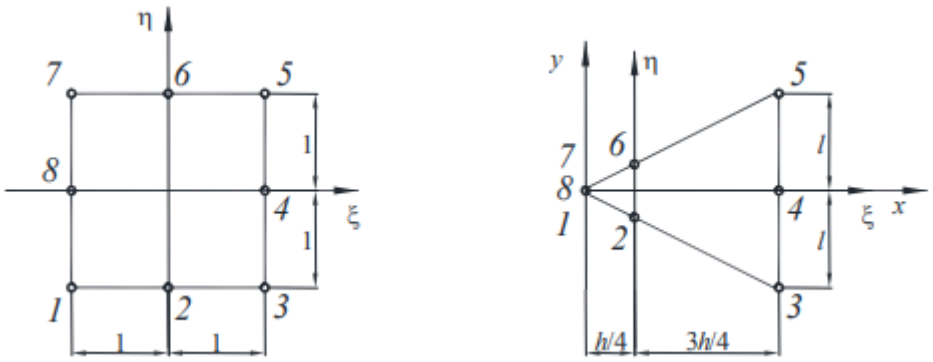


Figure 47. Definition of the singular element used in the linear elastic analysis [49].

The geometry of the element can be described by the following equations:

$$x = \sum_{i=1}^{8} N_i(\xi,\eta)x_i, \tag{15}$$

$$y = \sum_{i=1}^{8} N_i(\xi,\eta)y_i. \tag{16}$$

Shape functions are defined by the following equation:

$$N_i(\xi,\eta) = \frac{1}{4}\left[(1+\xi_i\xi)(1+\eta_i\eta) - (1-\xi^2)(1+\eta_i\eta) - (1-\eta^2)(1+\xi_i\xi)\right] + \frac{1}{2}\left[(1-\xi^2)(1+\eta_i\eta)((1-\xi_i^2)\eta_i^2 + (1-\eta^2)(1+\xi_i\xi)((1-\eta_i^2)\xi_i^2\right] \tag{17}$$

Displacement field can be described by the same shape functions as the element geometry:

$$u = \sum_{i=1}^{8} N_i(\xi,\eta)u_i, \tag{18}$$

$$v = \sum_{i=1}^{8} N_i(\xi,\eta)v_i. \tag{19}$$

If the global coordinate system origin is in the crack tip, the following can be noticed:

$$x_1 = x_7 = x_8 = 0, \quad x_2 = x_6 = \frac{h}{4}, \quad x_3 = x_4 = x_5 = h, \tag{20}$$

$$y_1 = y_4 = y_7 = y_8 = 0, \quad y_2 = -y_6 = -\frac{1}{4}, \quad y_3 = -y_5 = -l. \tag{21}$$

By including the values of natural coordinates to equation (17) and including values (20) and (21) to equations (15) and (16), the following can be concluded:

$$x = \frac{h}{4}(1+\xi)^2, \tag{22}$$

$$y = \frac{l}{4}\eta(1+\xi)^2. \tag{23}$$

Considering the fact that the strain is a function of the radius *r* from the crack tip, polar coordinates can be used and the following can be concluded:

$$r = \sqrt{x^2 + y^2} = \frac{h}{4}(1+x)^2 \sqrt{\left(\frac{h}{l}\right)^2 + h^2}. \quad \textbf{(24)}$$

The strain in *x* coordinate direction is defined as:

$$\varepsilon_x = A_0 + \frac{A_1}{\sqrt{r}} + \frac{A_2}{r}. \quad \textbf{(25)}$$

Constants in the equation (25) depend on the displacement of the nodes, which consequently determines the dominant type of singularity. By moving the midnodes as described above and under the condition that the nodes in the crack tip move together, dominant singularity becomes $1/\sqrt{r}$.

9. STRESS INTENSITY FACTOR FOR A 3D QUARTER-ELLIPTICAL CORNER CRACK

Stress intensity factor values were obtained for an example of a quarter-elliptical corner crack in a flat plate. The stress intensity factor K_I values were calculated analytically and compared to the numerical solution.

A 0.2x0.2x0.1 m flat plate with material and mechanical properties same as the hip prosthesis, shown in Table 2, was modelled. It was fixed at the base and loaded with a force of $1 \cdot 10^5$ N, uniformly distributed on the upper surface. Boundary conditions and the applied load can be seen in Figure 48.

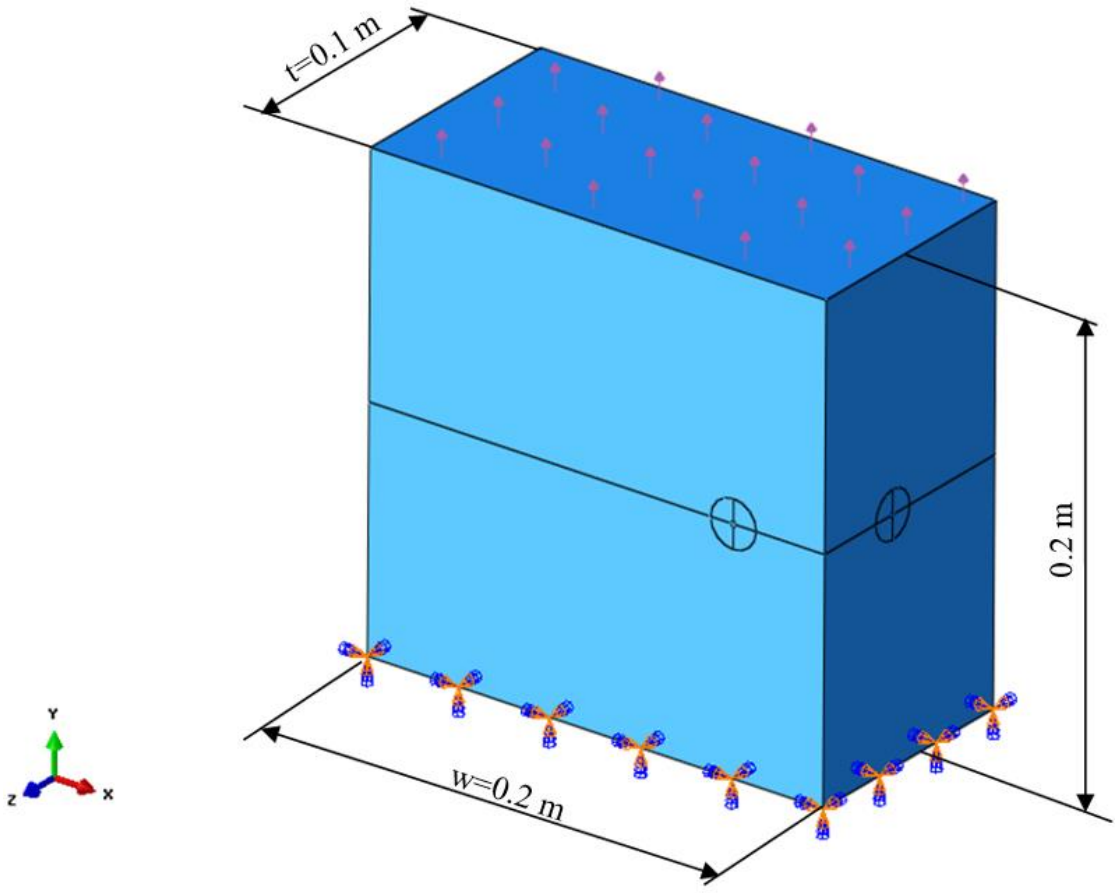


Figure 48. Dimensions of the model, the applied load and boundary conditions (fixed bottom surface).

The plate was partitioned into two cells by a plane located at the half of plate height, parallel to the plate base. A quarter-elliptical corner crack front was modelled by partitioning the

upper face of the bottom cell of the plate, shown in Figure 49, after which the face on the right side of the plate was partitioned with a 0.001 m radius circle. Both cells were partitioned by sweeping the circle on the path made in the previous step, highlighted with red colour in Figure 49. Around the obtained quarter of a torus, a 0.01 m radius quarter of a torus was modelled and the plate cells were again partitioned by this torus, as seen in Figure 48.

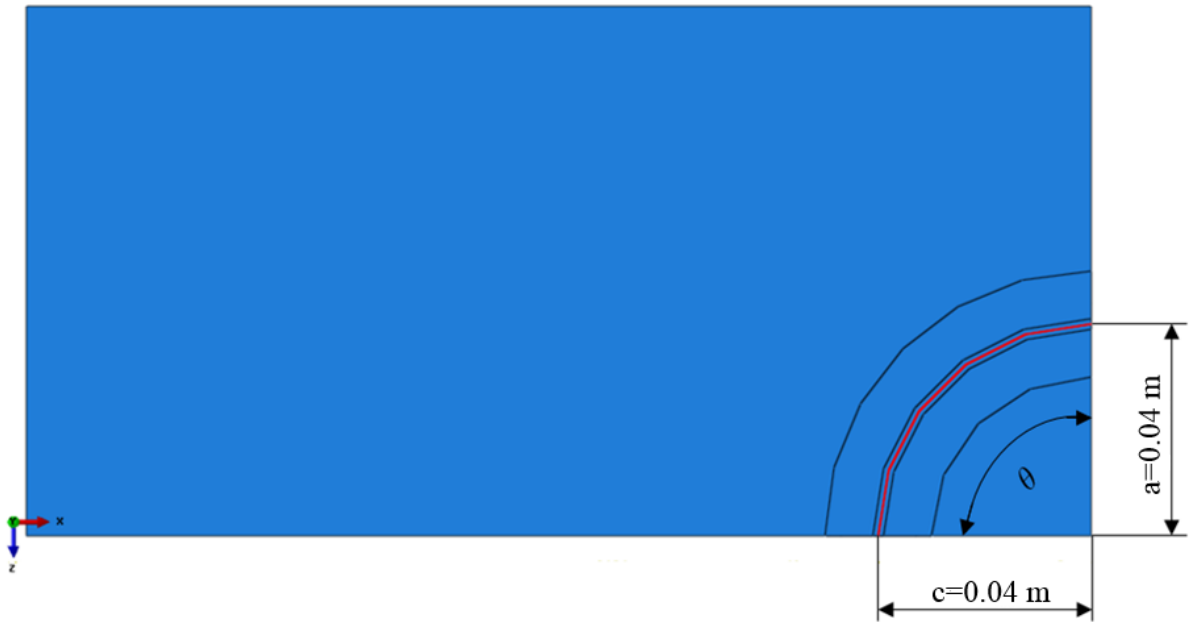


Figure 49. Crack front (red) and crack seam (from the corner to the red line).

Both the smaller and the bigger torus were partitioned into four cells to enable defining finer mesh. All the surfaces from the corner to the crack front, which can be seen in Figure 49, were selected as a crack seam. The smaller torus, containing the elements around the crack front, was meshed with wedge elements C3D15 (15-node quadratic triangular prism) in order to properly describe the singularity at the crack tip. The torus around it was meshed by structured second order hex elements C3D20 (20-node quadratic brick). The rest of the plate was meshed with free second order tetrahedral elements C3D10 (10-node quadratic tetrahedron). The mesh and the detail of the mesh can be seen in Figure 50 and Figure 51.

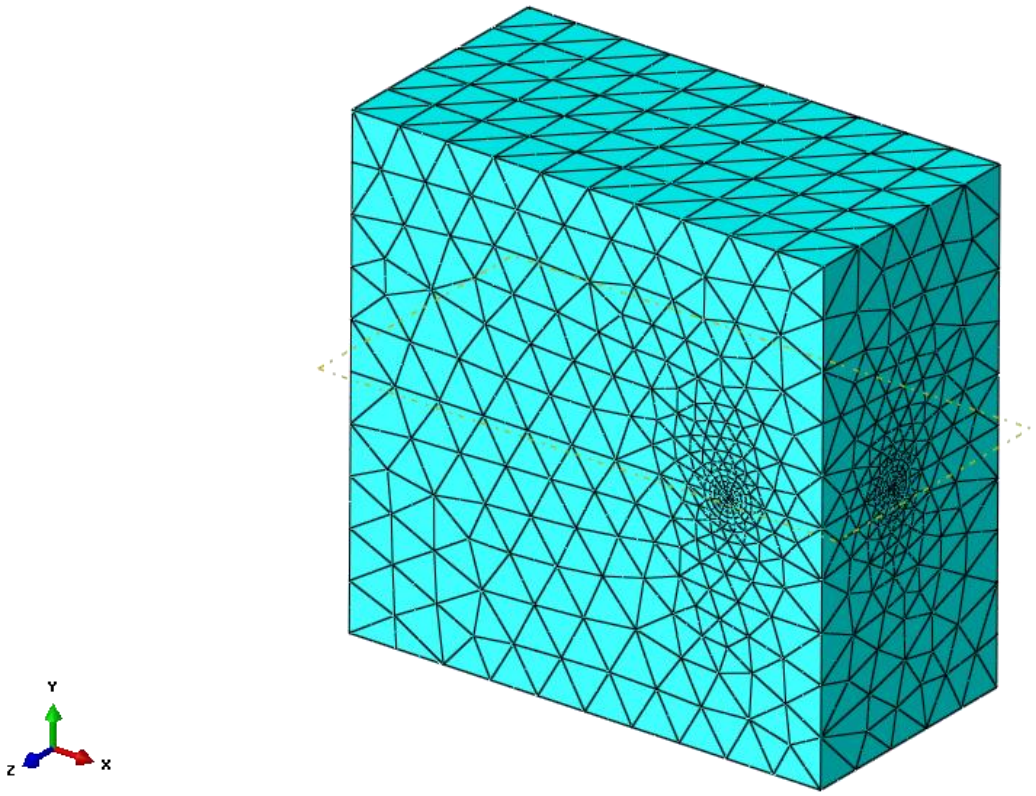


Figure 50. Mesh.

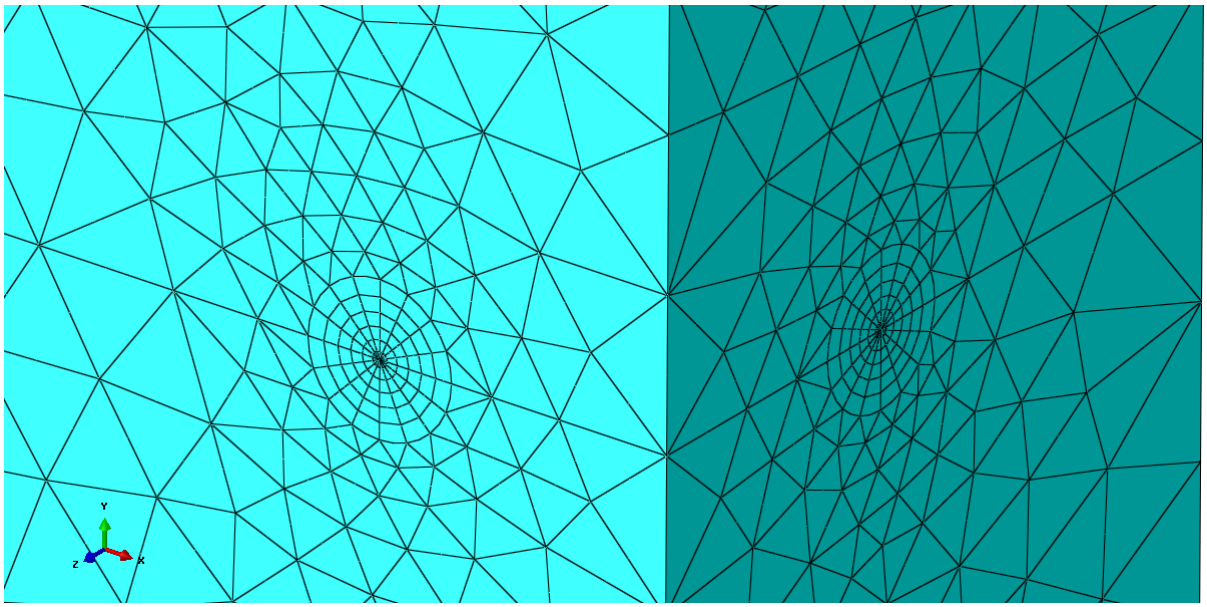


Figure 51. Detail of the mesh.

Due to the fact that the crack front is a curved line, crack extension direction was selected as normal to crack front, as shown in Figure 52. The midside node parameter of the wedge

elements was set as 0.25, which means that the midside nodes of the wedge elements were moved to 0.25 of the length of the torus, closer to the crack front.

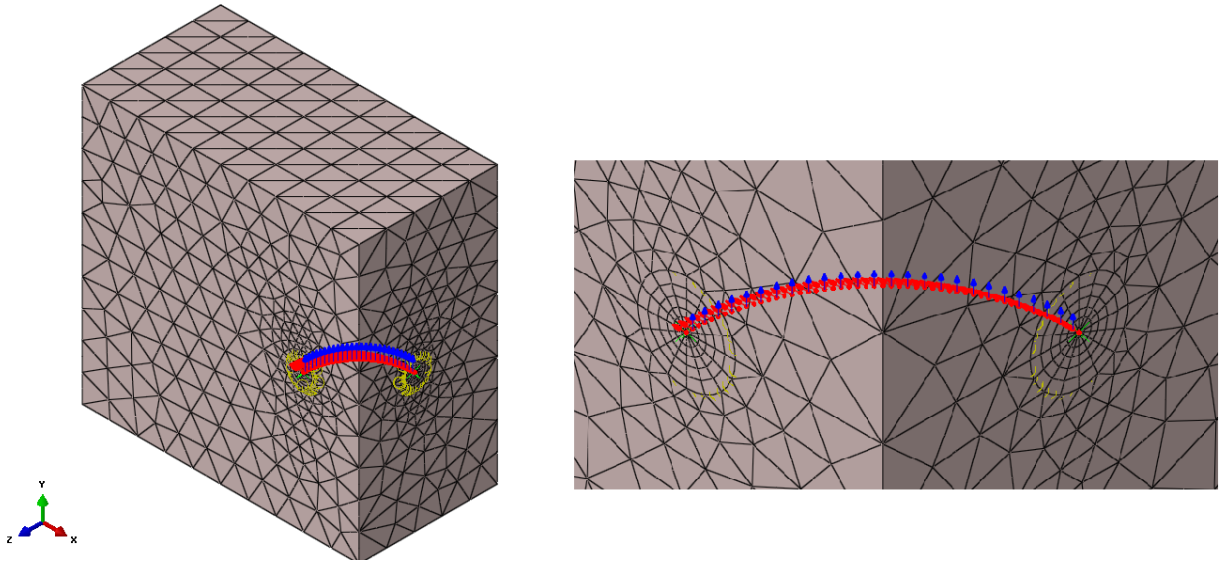


Figure 52. Definition of crack extension direction.

Von Mises stress distribution on the deformed shape can be seen in Figure 53 and the detail of the Von Mises stress distribution around the crack front can be seen in Figure 54.

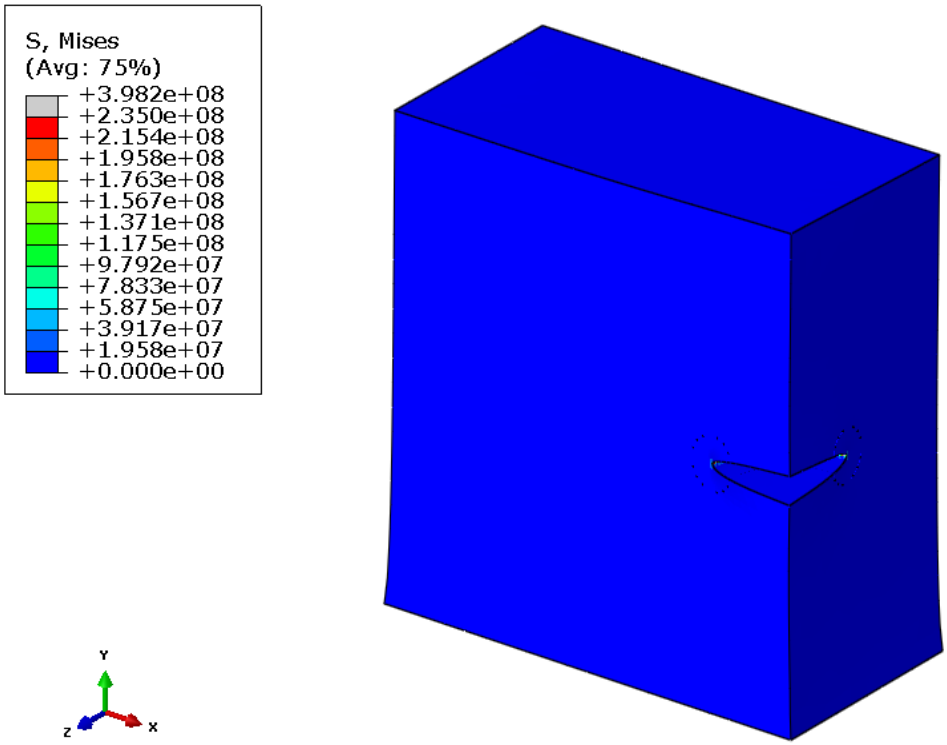


Figure 53. Von Mises stress distribution.

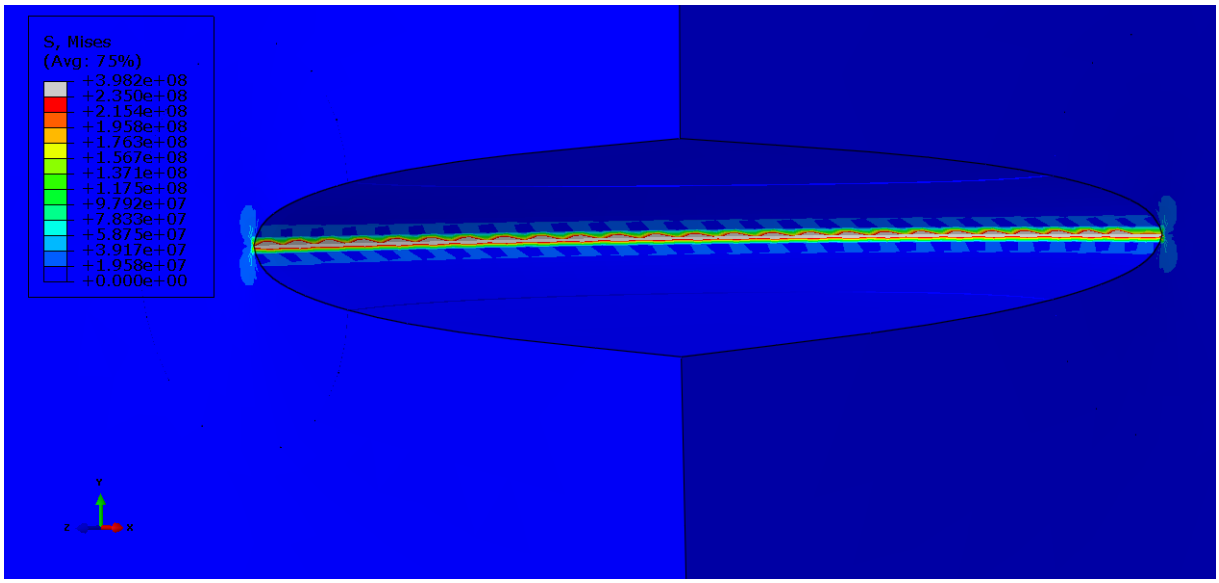


Figure 54. Detail of the Von Mises stress distribution around the crack front.

Five contours were considered around the crack front. The obtained K_I values along the contours is shown in Figure 55, while the convergence of the K_I value for node 24 is shown in Figure 56.

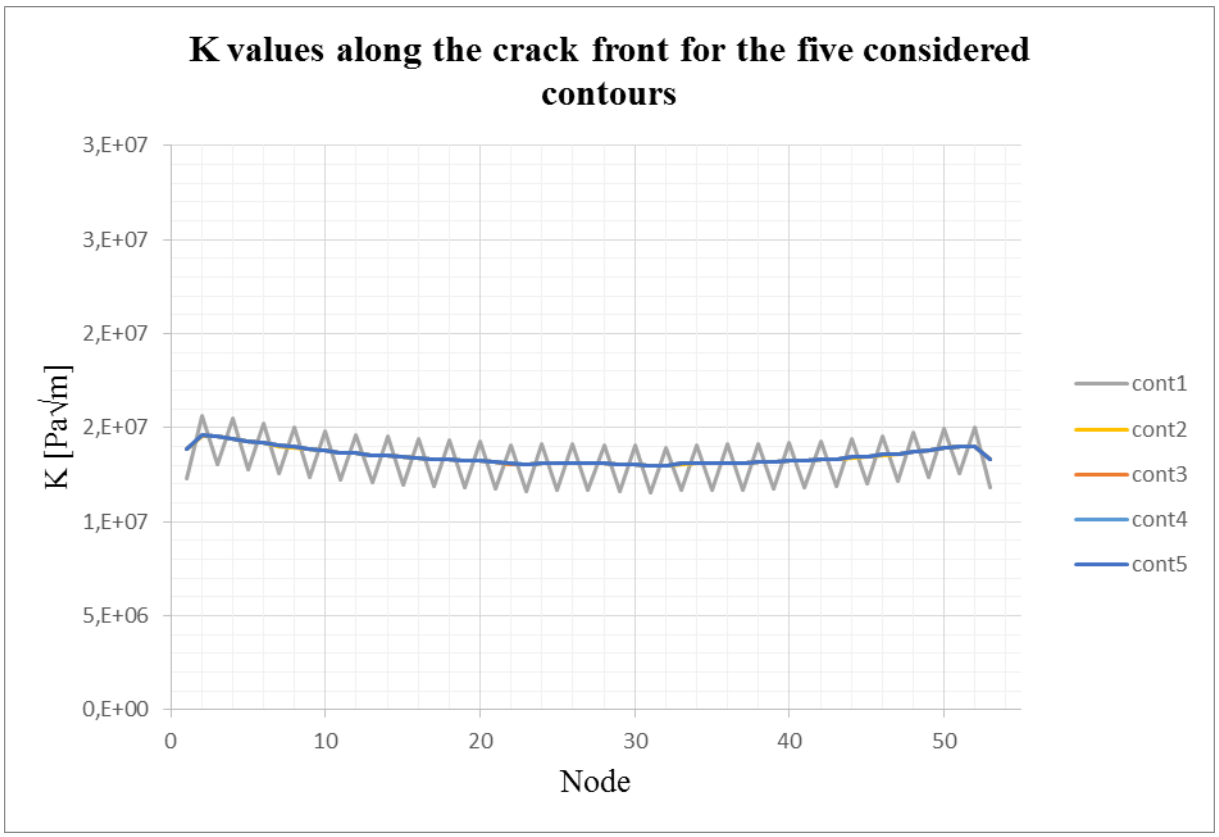


Figure 55. K_I values along the crack front for the five considered contours.

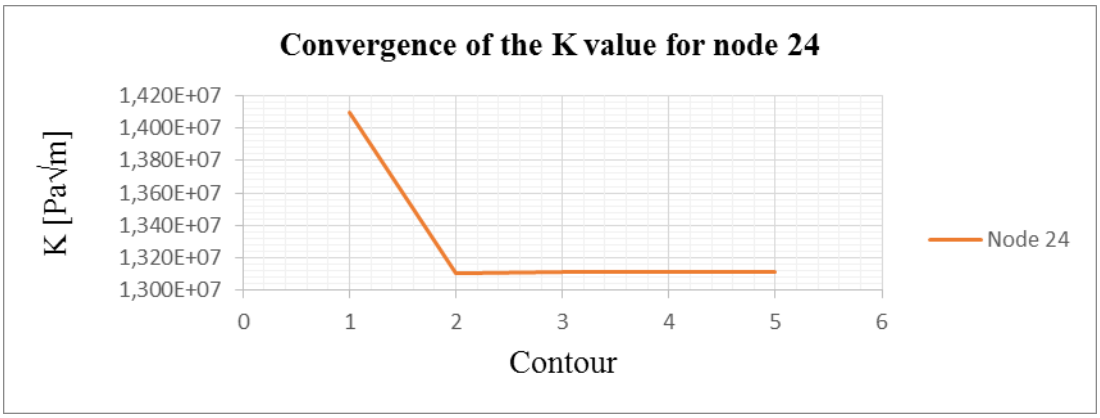


Figure 56. Convergence of the K_I value for node 24.

The average K_I value for this example is 13.48 MPa√m.

9.1. Analytical solution

Analytical calculation for stress intensity factor K_I was carried out for a quarter-elliptical corner crack in a flat plate where a=c and the analytical solution was compared with the numerical solution. K_I was calculated using the formulae [53] for calculation of stress intensity factor K_I for a quarter-elliptical corner crack in a flat plate. K_I was determined for every 10° angles along the crack front, namely for: θ = 0°, θ = 10°, θ = 20°, θ = 30° and θ = 40°, θ =50°, θ =60°, θ =70°, θ =80° and θ =90°. θ, a and c are crack dimensions shown in Figure 49. The comparison of the obtained numerical results for the fifth contour and the analytical results can be seen in Table 5 and the diagram in Figure 57.

Table 5. Comparison of analytically and numerically obtained K_I values for several nodes along the crack front.

θ	K_I [MPa√m] analytical	K_I [MPa√m] numerical	Difference [%]
0°	14.0919	13.9000	1.5
10°	13.3153	14.0000	4.9
20°	12.8227	13.5000	5.0
30°	12.5393	13.3000	5.3
40°	12.4162	13.1000	5.3
50°	12.4039	13.0000	4.6

60°	12.4778	13.1300	5.0
70°	12.6871	13.3000	4.6
80°	13.0443	13.5920	4.0
90°	13.5990	13.2870	2.3

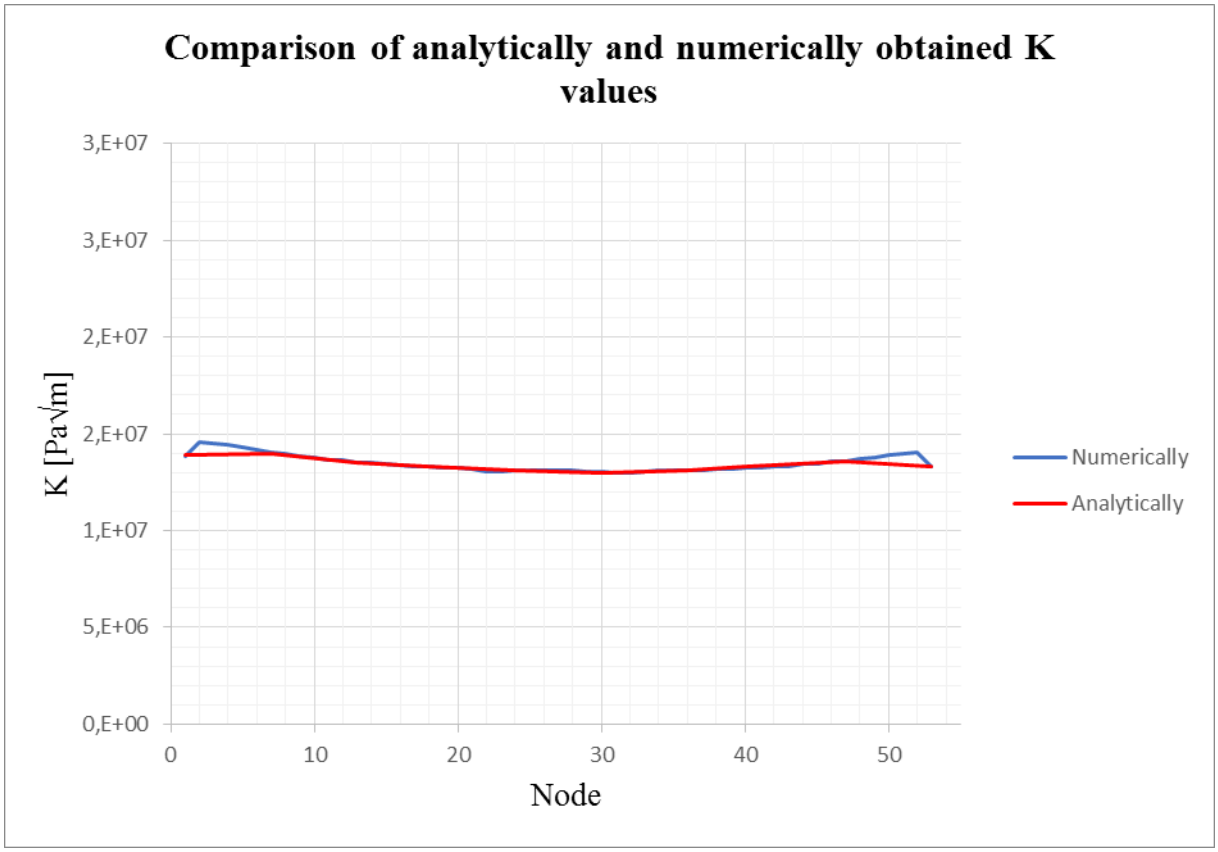


Figure 57. Comparison of analytically and numerically obtained K_1 values.

It can be concluded that the correlation between analytically and numerically obtained solutions is relatively good, with under 6% of difference between the results along the whole crack front.

10. CRACK MODELLING ON THE FEMORAL COMPONENT OF A TOTAL HIP PROSTHESIS

For the femoral component of a total hip prosthesis cemented into cortical bone, as shown in Figure 16, a corner elliptical crack was modelled based on the obtained stress values, shown in Figure 24. The considered stress values were obtained for boundary and loading conditions based on the previously explained fatigue standard ISO 7206-4 testing conditions. The highest tensile stresses in this case appeared on the edge of the fixed area, on the posterior-lateral side of the upper part of the prosthesis femoral component, as shown in Figure 58. This location is the location with highest probability of crack initiation.

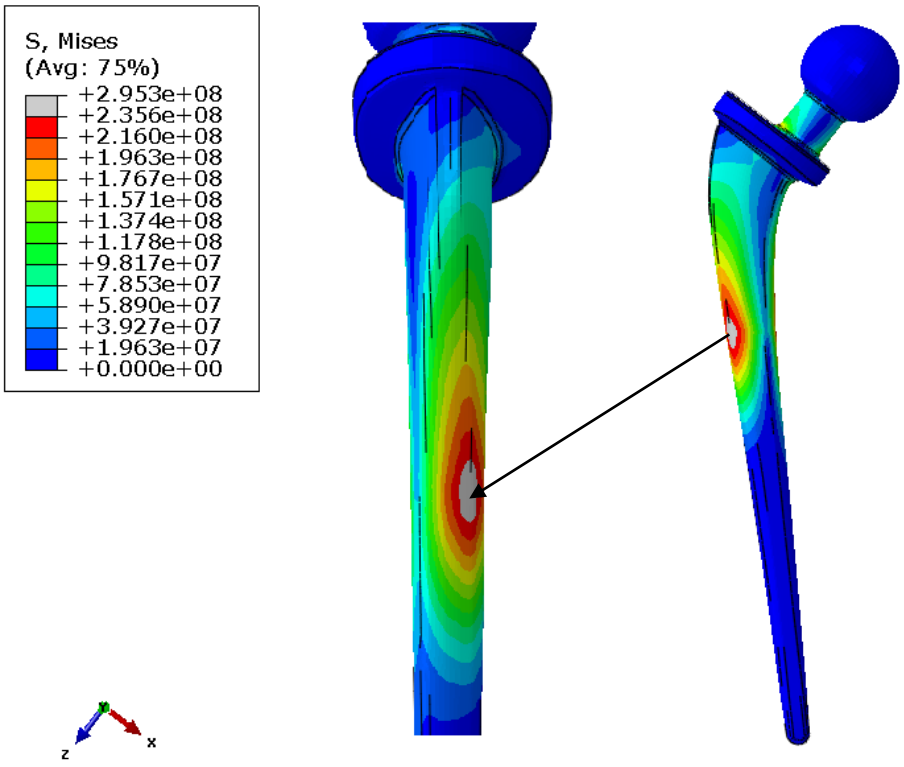


Figure 58. The site with highest tensile stress value on the femoral component in Case I.

Due to the fact that the geometry of the prosthesis femoral component is irregular and complex, it was not possible to model a crack in the same way that it could be done for a regular geometry object, as shown in Chapter 9.

The shaft of the prosthesis femoral component model was partitioned by a plane that passes through the node with the highest stress value. A 0.1 mm radius torus was modelled as a separate part and partitioned into four cells. The torus was positioned in the assembly of the prosthesis femoral component, cement and the bone so that the centre line of the torus could correspond to the crack front shape and position. It was constrained in the way that the plane passing through the middle of the torus would lay on the plane used to partition the femoral component shaft. Both cells of the femoral component shaft were partitioned by sweeping the outer and inner edges of the torus by the line that passes through the centre of the torus, highlighted red in Figure 61. A 1 mm radius torus was also modelled as a separate part and positioned in the same way as the first torus. It was constrained so that the plane passing through the middle of the torus would lay on the plane passing through the middle of the 0.1 mm torus. In order for the 1 mm torus to be in the same position as the 0.1 mm torus, the points in the middle of the faces of the 1 mm torus were set to be coincident to the points in the middle of the faces of the 0.1 mm torus. Position of the 1 mm torus in the prosthesis-cement-bone assembly can be seen in Figure 59 and the 0.1 mm torus is positioned inside the 1 mm torus. The 1 mm torus was used to partition both cells of the femoral component shaft in the same way as with the 0.1 mm torus. Both tori were later excluded from the analysis. The partitioned cells in the femoral component shaft are shown in Figure 60. Stress intensity factors were obtained for three different crack length. Different crack lengths were made by translating the tori for 1 mm two times, on the plane which was used for partitioning the femoral component shaft.

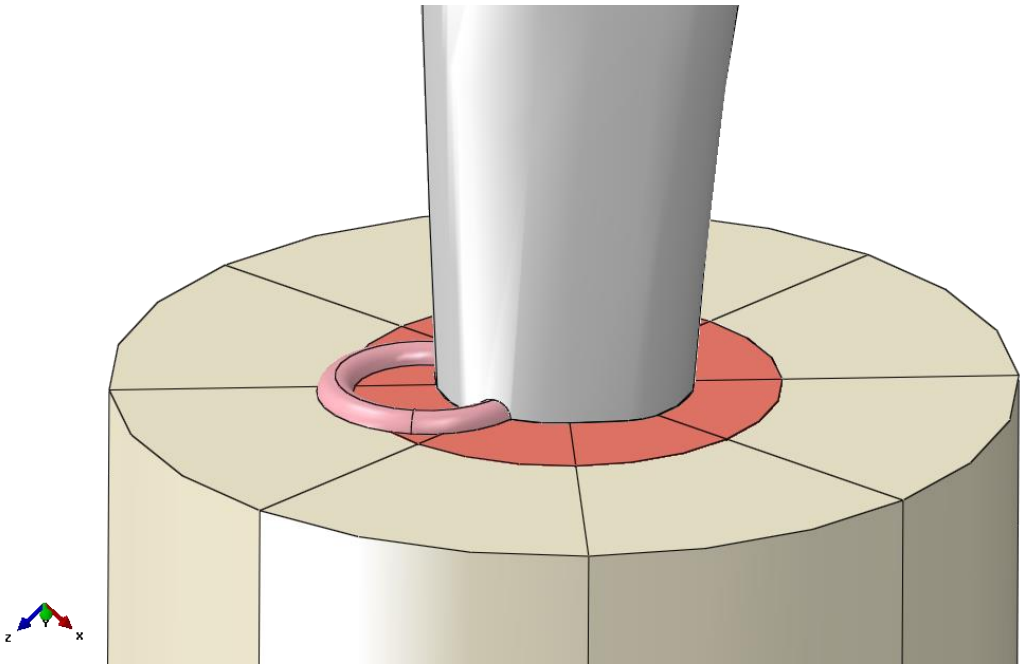


Figure 59. Position of the torus in the prosthesis-cement-bone assembly.

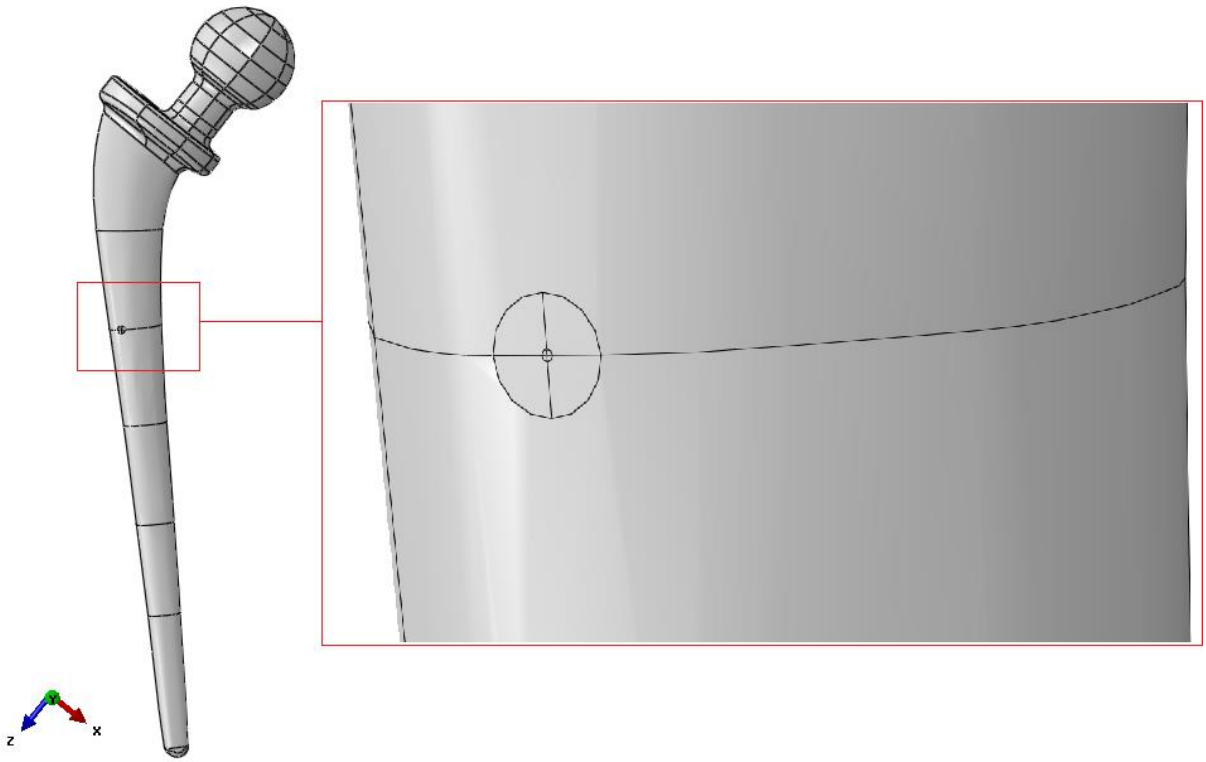


Figure 60. Partitioned cells of the femoral component shaft.

The line that passes through the centre of the cells partitioned by the tori was selected as a crack front. For the three considered crack depths, this line is highlighted red in Figure 61. All the surfaces from the edge to that line were selected as crack seam. Crack extension direction was selected as normal to crack front and the midside node parameter of the wedge elements was set as 0.25, which means that the midside nodes of the wedge elements were moved to 0.25 of the length of the torus, closer to the crack front. This is shown in Figure 63.

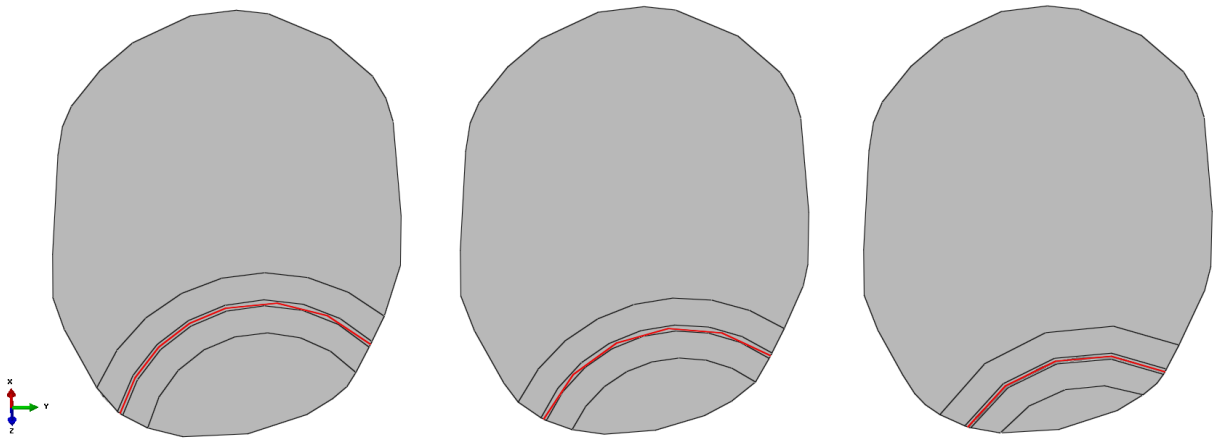


Figure 61. Crack front (red line) and the crack seam (faces from the edge to the red line) for the three crack lengths.

Cells made by sweeping the 0.1 mm torus by the highlighted line were meshed with second order wedge elements C3D15 (15-node quadratic triangular prism). Cells made by sweeping the 1 mm torus by the highlighted line were meshed with structured second order hexagonal elements C3D20 (20-node quadratic brick). Same number of elements was assigned as for the cells made using the 0.1 mm torus. The mesh of those cells can be seen in Figure 62 and the mesh detail of the prosthesis femoral component can be seen in Figure 66. Mesh on the section containing the crack front is shown in Figure 64 and Figure 65. Stress intensity factors were calculated for five contours.

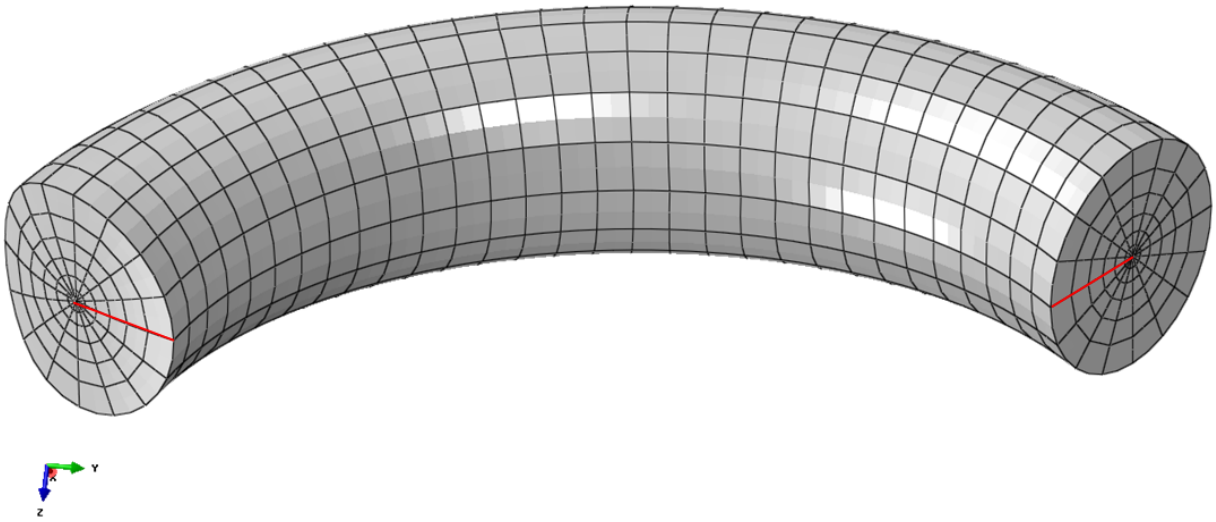


Figure 62. Mesh on the cells made by partitioning the femoral component shaft by the tori.

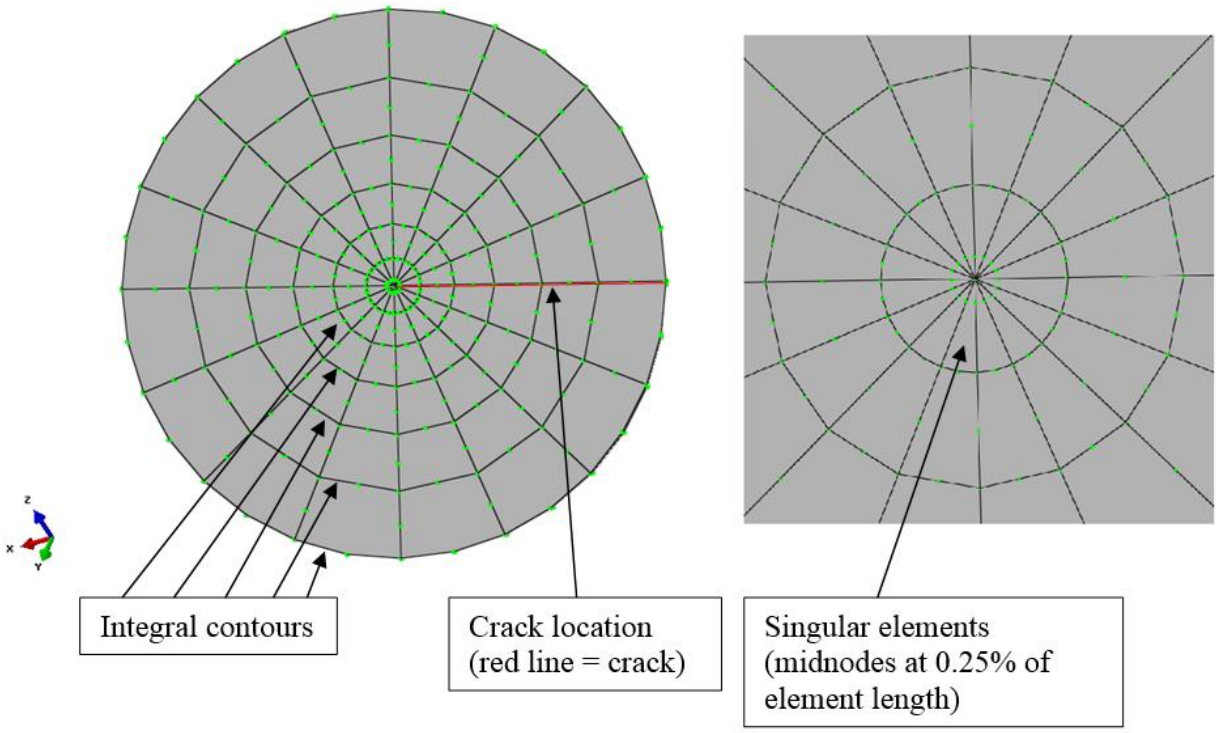


Figure 63. Elements around the crack front.

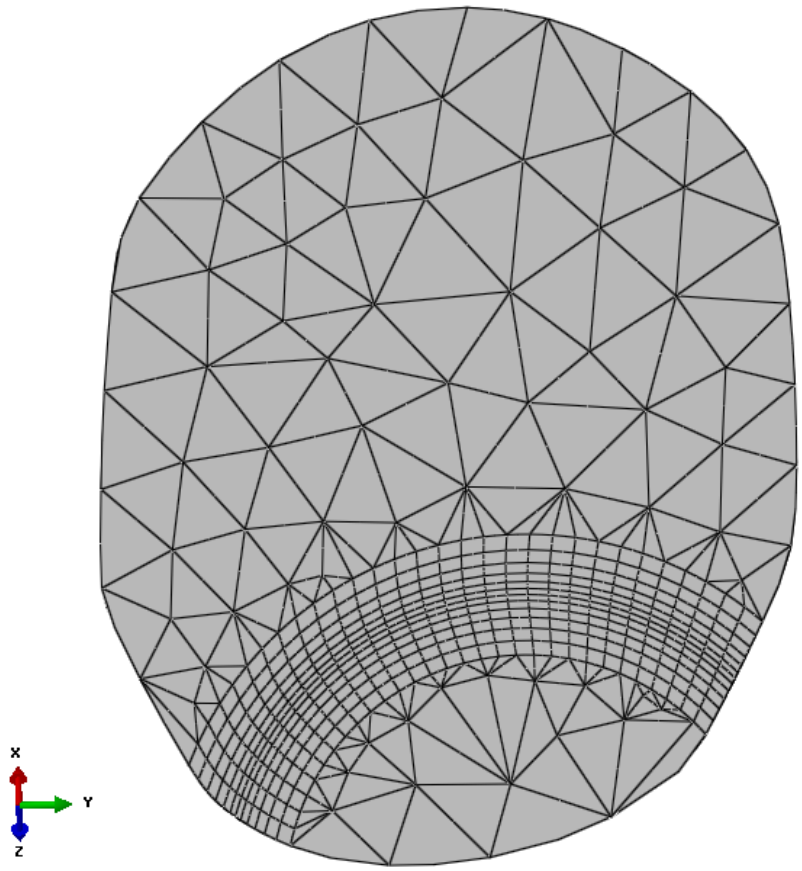


Figure 64. Mesh on the section containing the crack front for one crack length.

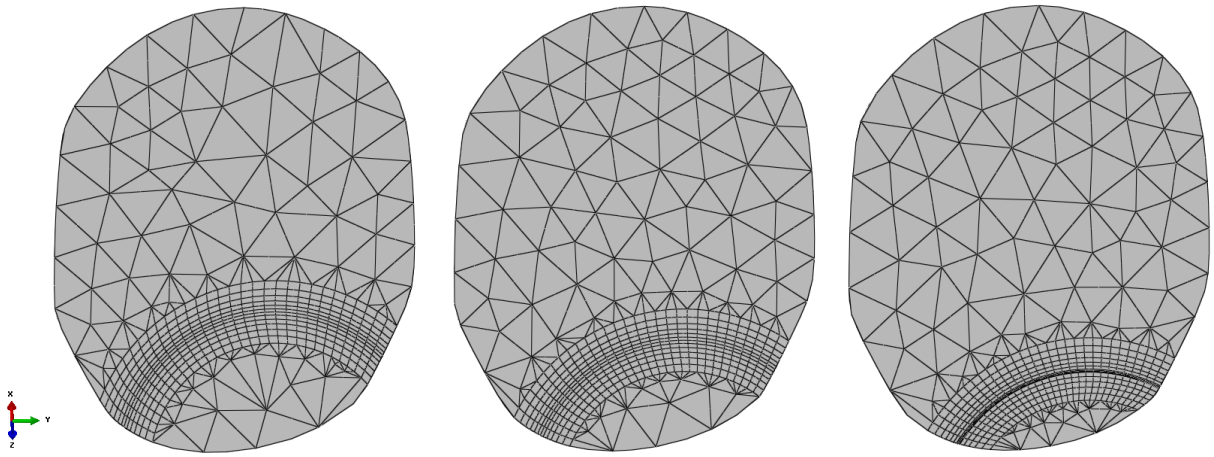


Figure 65. Mesh on the section containing the crack front for the three crack lengths.

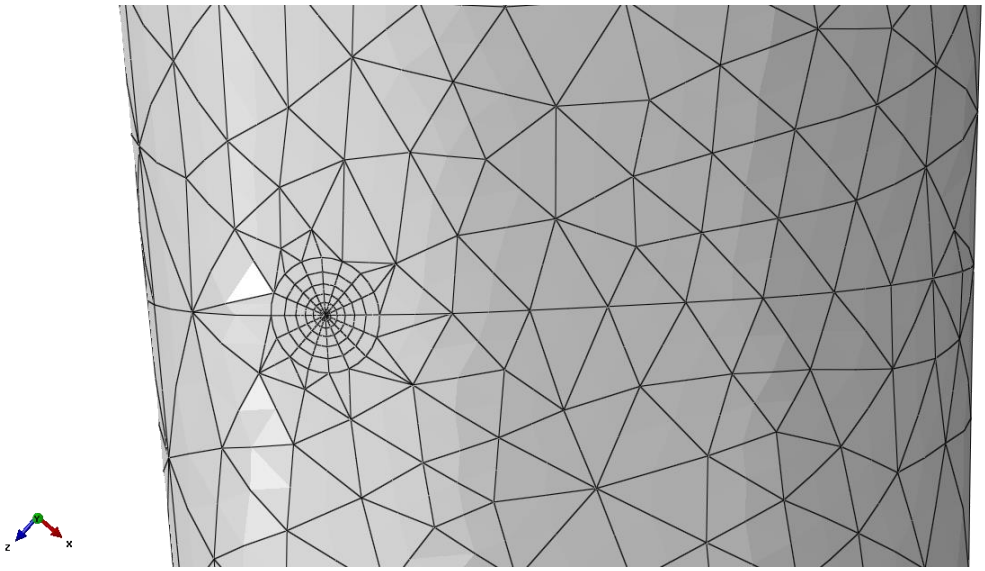


Figure 66. Mesh detail on the prosthesis femoral component model.

The obtained Von Mises stress distribution on the femoral component model for the three different crack depths can be seen in Figure 67 (the smallest crack length), Figure 68 (middle size crack) and Figure 69 (the longest considered crack length). It can be noticed that the stress values around the crack front increase as the crack length increases.

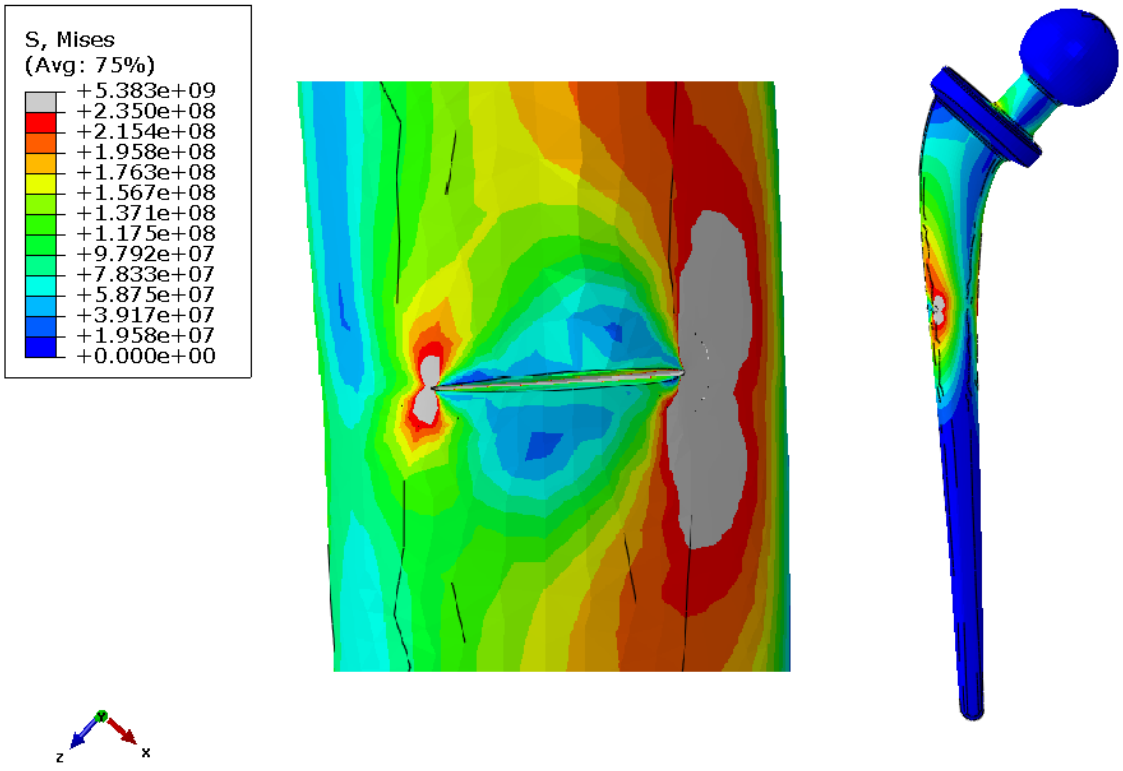


Figure 67. Von Mises stress distribution for the smallest crack size.

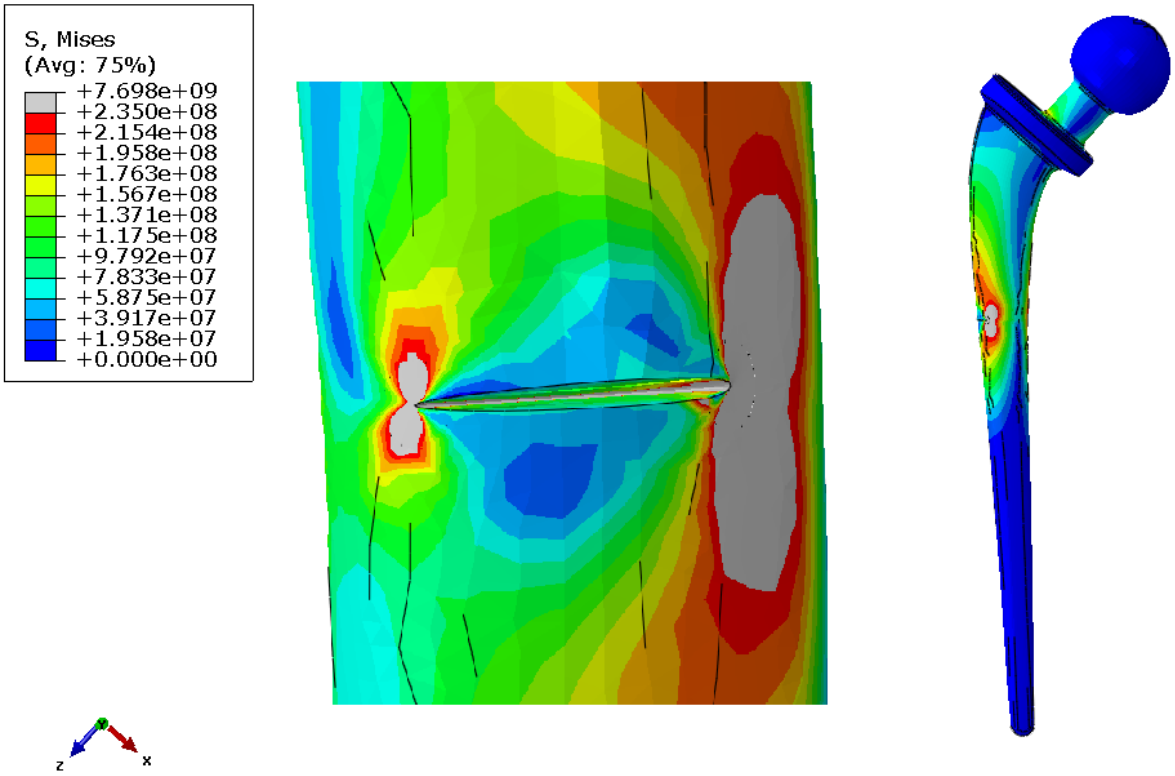


Figure 68. Von Mises stress distribution for the middle crack size.

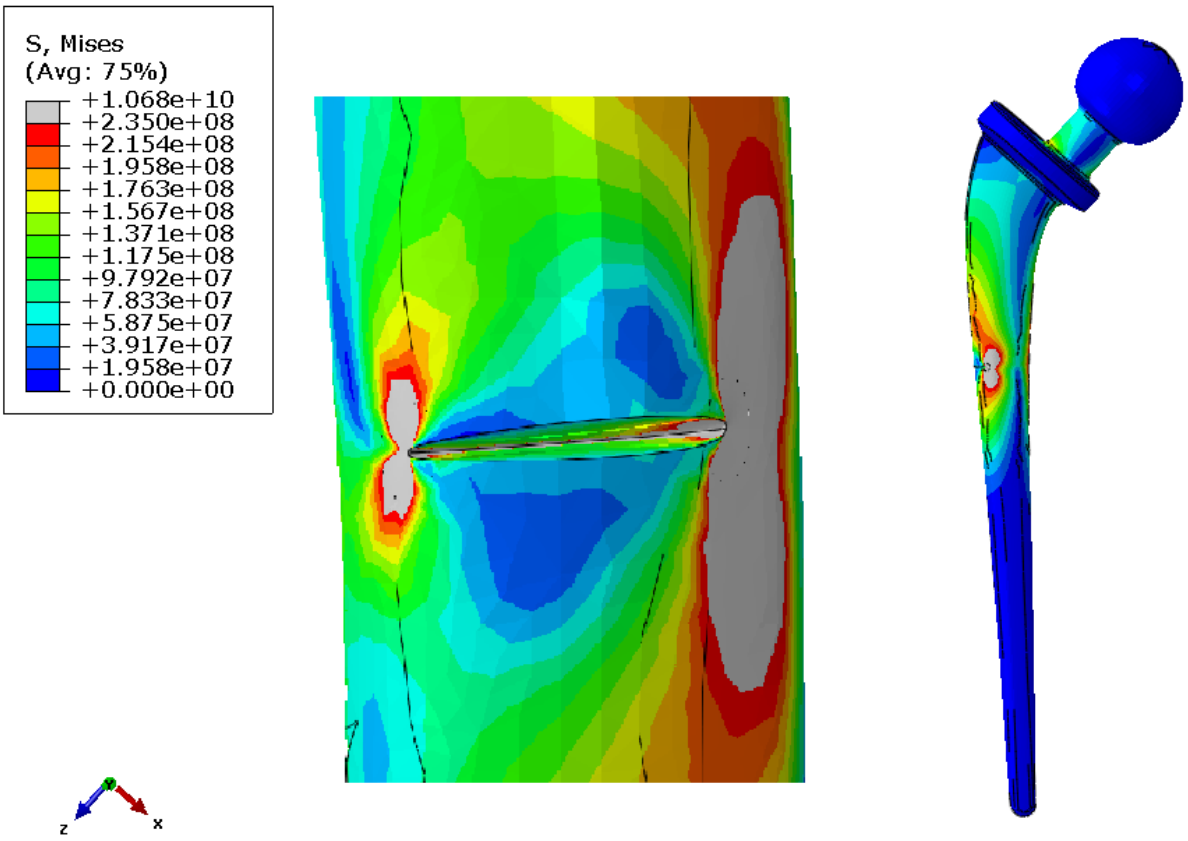


Figure 69. Von Mises stress distribution for the longest crack size.

Stress intensity factor K_I values were obtained for 61 nodes along the crack front line for each crack depth. They were obtained for five different contours around the crack front, shown in Figure 63. The first node (Node 1) and the last node (Node 61) locations are marked on the crack front line in Figure 70.

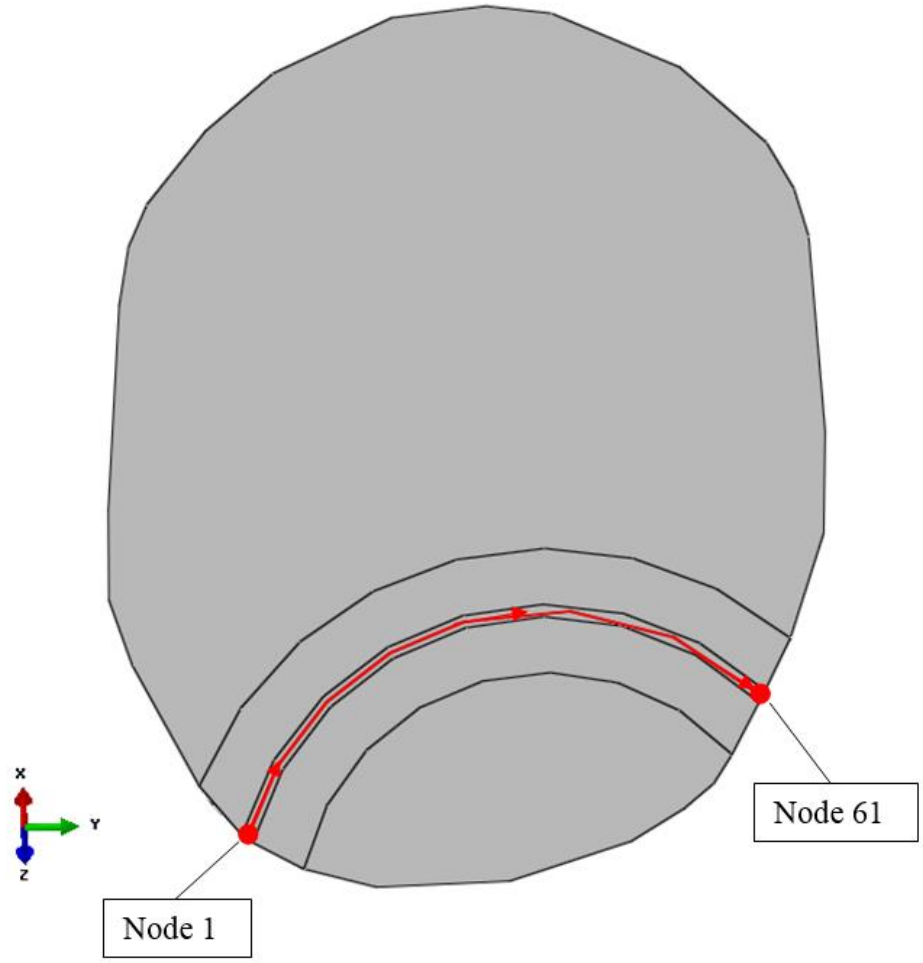


Figure 70. The first and the last node location on the crack front.

The obtained stress intensity factor K_I values along each of the contours for the smallest considered crack length are shown in the diagram in Figure 71 and the convergence of K_I value for this crack size is shown in the diagram in Figure 72. For the middle size crack length K_I values are shown in Figure 73 and the convergence in Figure 74. For the longest considered crack length, K_I values along the contours are shown in Figure 75 and the convergence is shown in Figure 76.

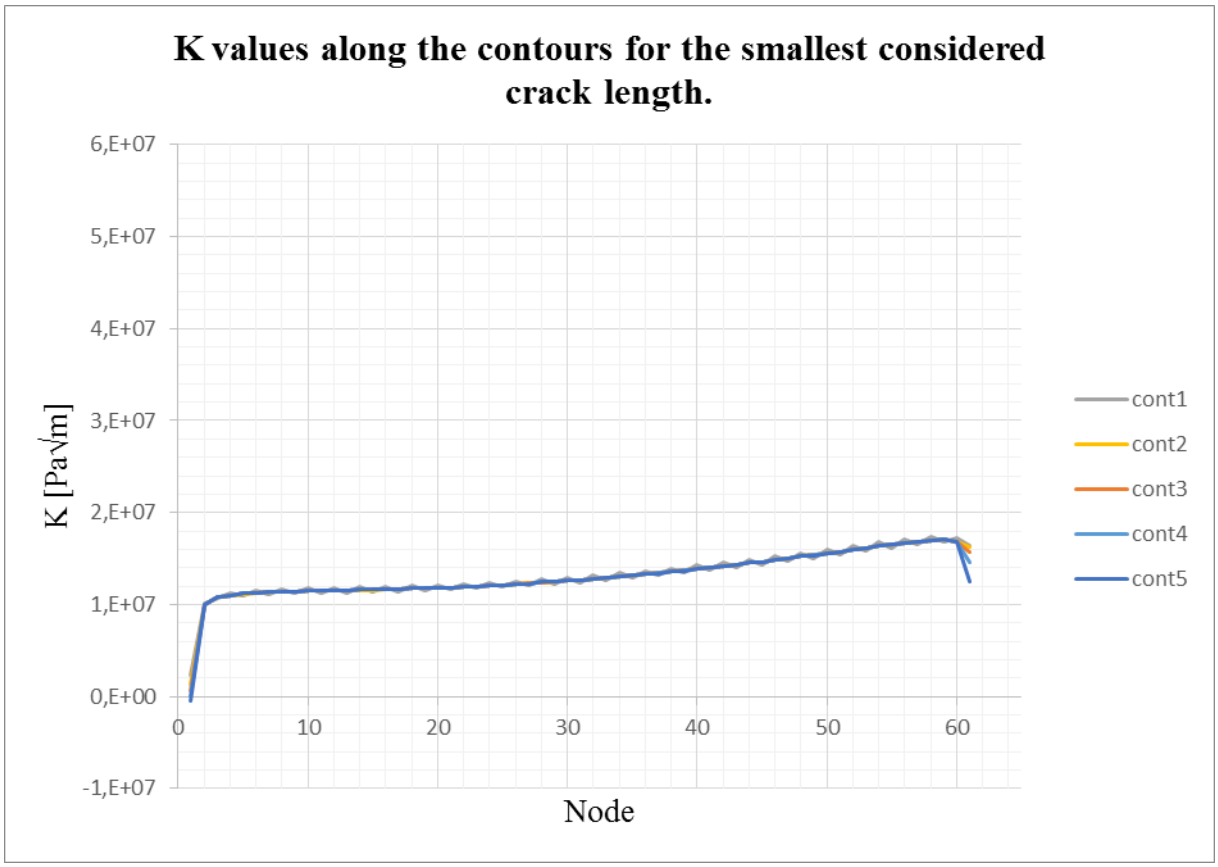


Figure 71. K_I values along the contours for the smallest considered crack size.

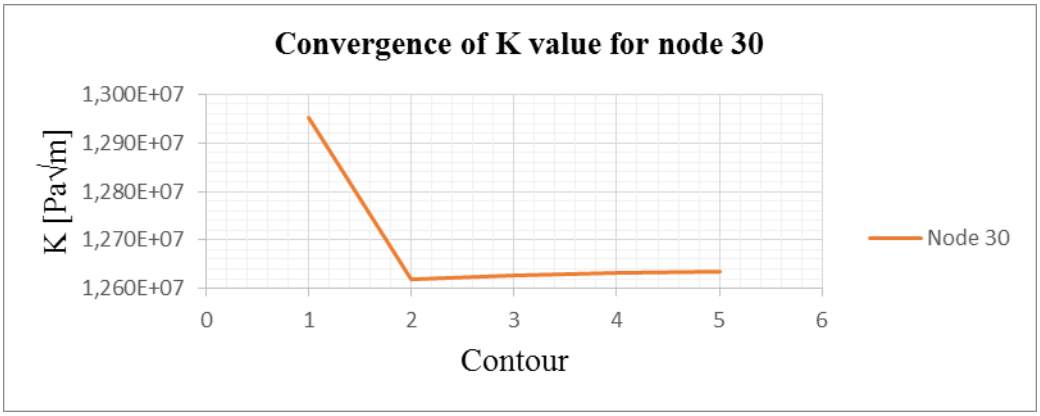


Figure 72. Convergence of K_I value for node 30 for the smallest considered crack size.

The average K_I value for the smallest considered crack size is 13.10 MPa√m.

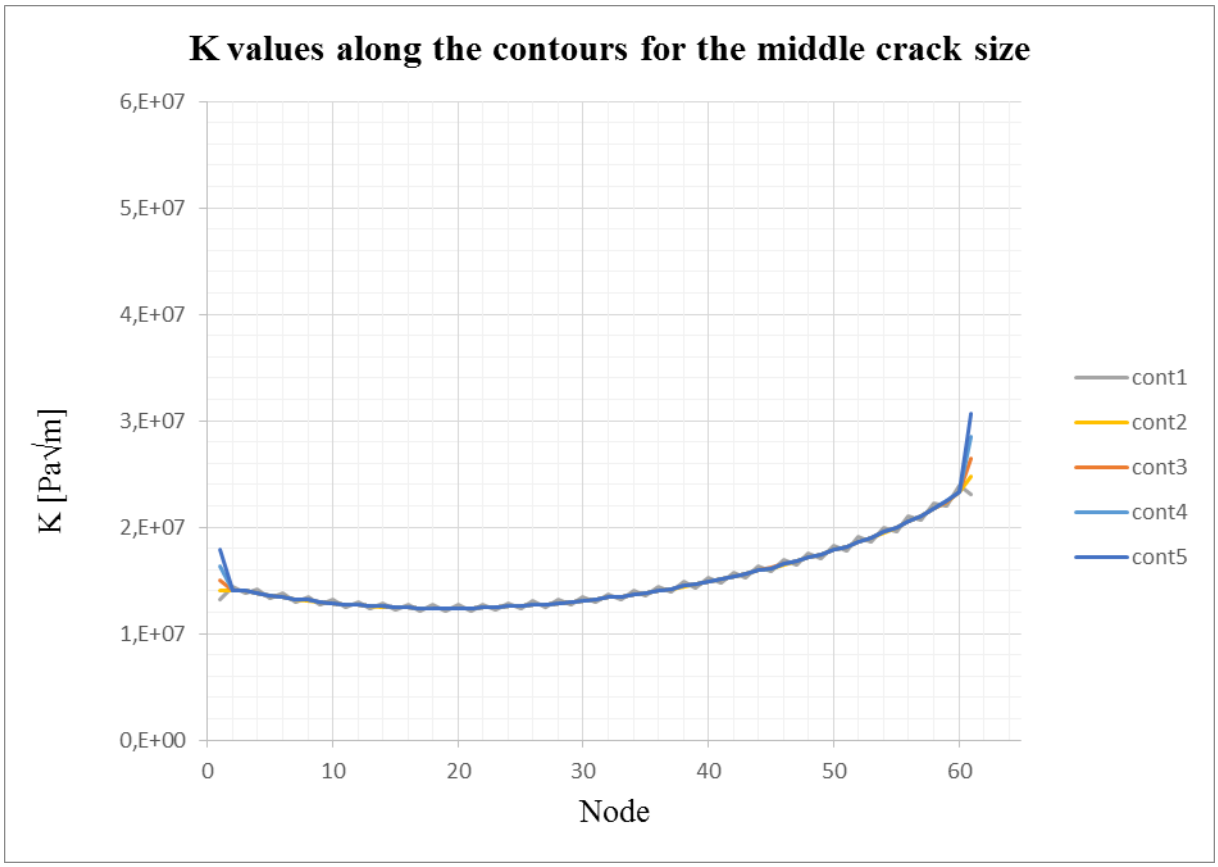


Figure 73. K_I values along the contours for the middle crack size.

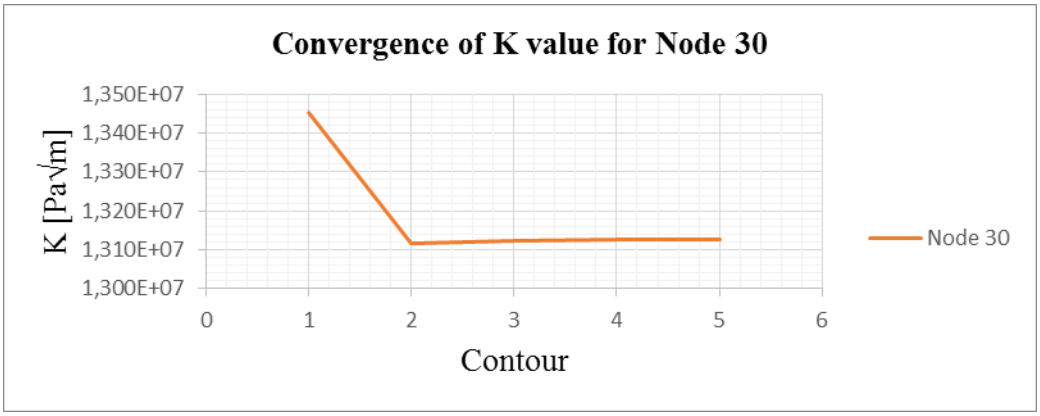


Figure 74. Convergence of K_I value for node 30 for the middle crack size.

It can be noticed that the average K_I value for this crack length is 15.16 MPa√m.

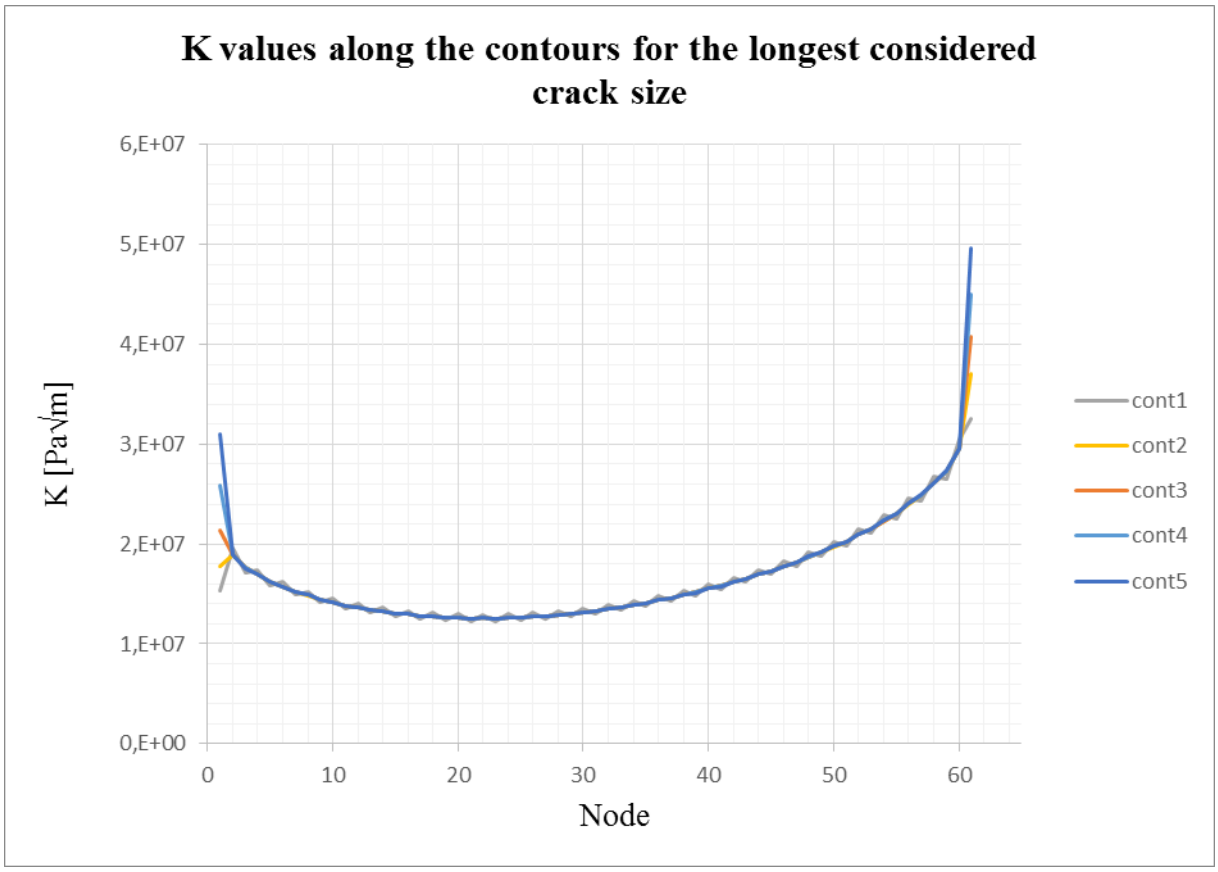


Figure 75. K_I values along the contours for the longest considered crack size.

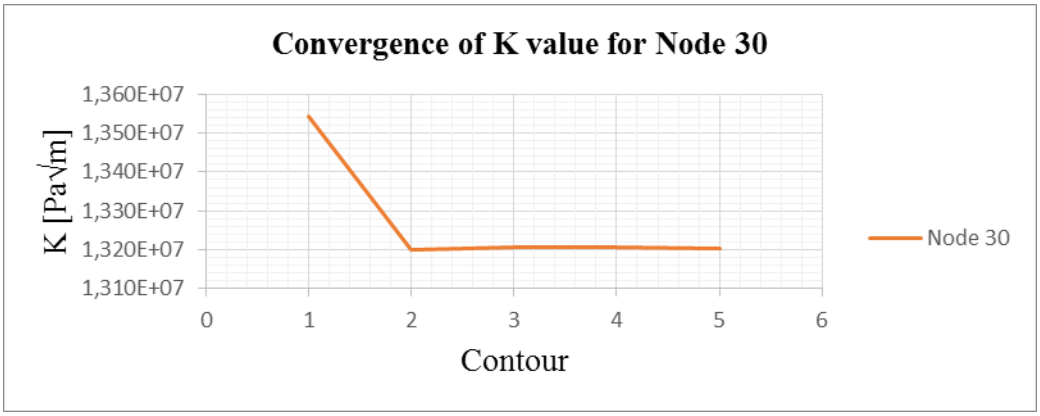


Figure 76. Convergence of K_I value for node 30 for the longest crack size.

Average K_I value for the longest considered crack size is 16.87 MPa√m. Comparison of K_I values along the contour 5 for the three considered crack lengths is shown in Figure 77. It can be noticed that K_I changes less in case of the smaller cracks. K_I values around the middle of

the crack front line are almost constant as the crack increases, while the values on the edges change the most.

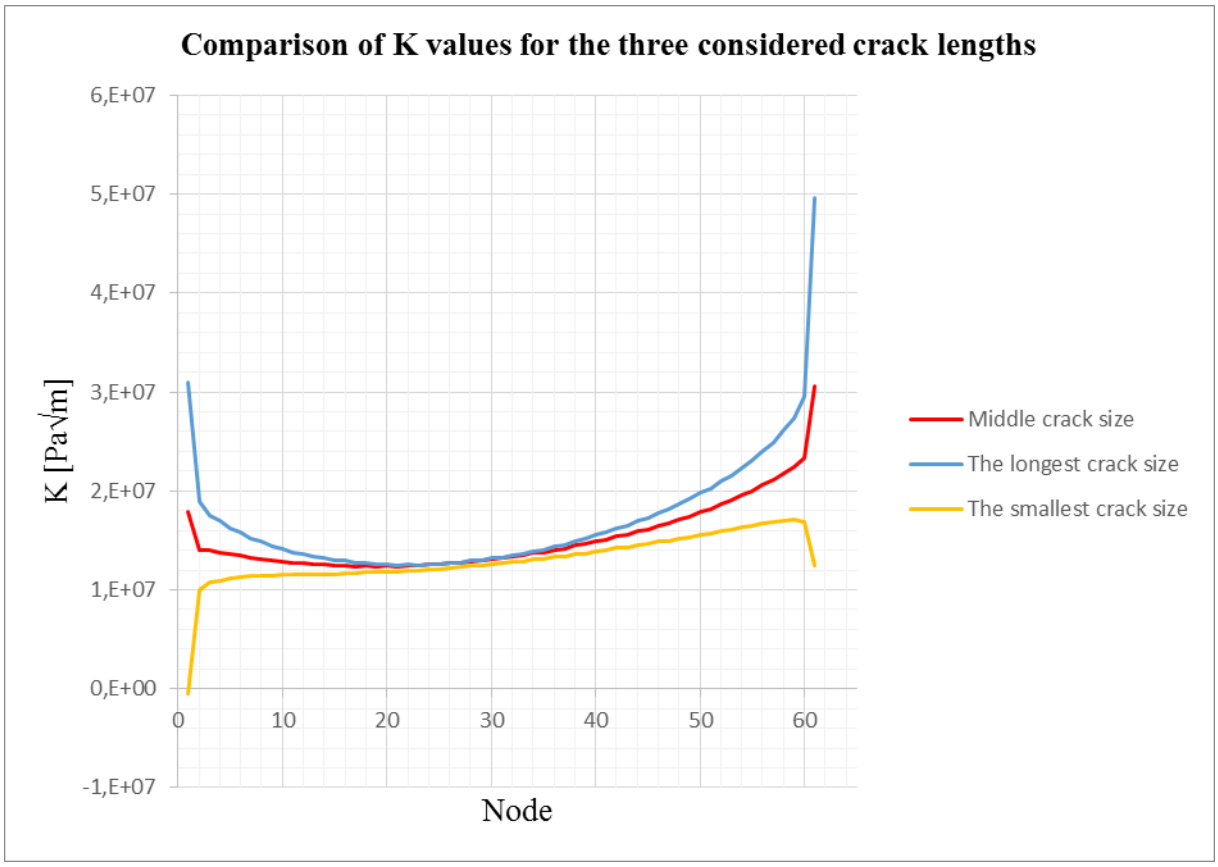


Figure 77. Comparison of K_I values for the three considered crack lengths.

Considering the fact that K_{Ic}, the critical value of K_I, usually ranges between 50 and 90 MPa√m [54] and that the average K_I value for each of the considered cases is significantly lower than the usual K_{Ic} value, it can be concluded that fracture of the prosthesis femoral component would not occur for the considered crack lengths.

11. CONCLUSION

CAD model of the prosthesis femoral component obtained by the 3D scanning procedure was used as a base to create a FEM model by means of Abaqus software. Finite element analyses were conducted for a loosened femoral component of the total hip prosthesis for the two considered loading cases. In Case I the loads are based on the standard ISO 7206-4 and in Case II are assumed loads which occur due to normal human walking. In case of loading conditions based on the standard the tensile stresses occurred on posterior-lateral side of the upper part of the femoral shaft, where fatigue cracks normally occur in vivo, as reported in the relevant literature. In the case of loads due to regular walk tensile stresses lower than the fatigue limit of the considered stainless steel occurred. It was demonstrated that the procedure based on reverse engineering can be successfully applied to fatigue life assessment of the considered total hip prosthesis. The procedure can be implemented to other implants and prostheses where it is needed to reconstruct components geometry by the scanning procedure. As a further step, three depths of a crack were modelled at the site where crack initiation was expected based on the obtained results and real cases. Stress intensity factor values were determined for each crack depth. Convergence of K_I values for each of the considered crack lengths was shown and it can be noticed that the value of K_I changes the most near the edges of the crack, while it is almost constant around the middle of the crack front line. In this work, it was demonstrated that stress intensity factors can be calculated for an arbitrary shape of a crack front. In the further step, stress intensity factors shall be calculated for longer cracks and then the obtained values can be compared with fracture toughness K_{Ic} in order to assess fracture onset conditions.

REFERENCES

[1] Griza, S., Vieira dos Santos, S., Massayoshi Ueki, M., Bertoni F., Strohaecker, T., Case study and analysis of a fatigue failure in a THA stem, Engineering Failure Analysis, 2013., vol. 28, pp. 166-175.

[2] Griza, S., Kwirtniewski, C., Tarnowski, G., Bertoni, F., Reboh, Y., Strohaecker, T., Rabin Baumvol, I., Fatigue failure analysis of a specific total hip prosthesis stem design, International Journal of Fatigue, 2008., vol. 30, no. 8, pp. 1325-1332.

[3] Bennet, D., Goswami, T., Finite element analysis of hip stem designs, Materials and Design, 2008., vol. 29, no. 1, pp. 45-60.

[4] Babić, M., Verić, O., Božić, Ž., Sušić, A., Reverse engineering based integrity assessment of a total hip prosthesis, Procedia Structural Integrity, 2018., vol. 13, pp. 438-443.

[5] Bousnane, T., Benbarek, S., Sahli, A., Serier, B. Bahir Bouiadjra, B., Damage of the Bone-Cement Interface in Finite Element Analyses of Cemented Orthopaedic Implants, Periodica Polytechnica Mechanical Engineering, 2018., vol. 62, no. 2, pp. 173-178.

[6] Oshkour, A., Davoodi, M., Abu Osman, N., Yau, Y., Tarlochan, F., Wan Abas, W., Finite element analysis of circumferential crack behaviour in cement-femoral prosthesis interface, Materials and Design, 2013., vol. 49, pp. 96-102.

[7] Li, S., Abdel-Wahab, A., Demirci, E., Silberschmidt, V., Fracture process in cortical bone: X-FEM analysis of microstructured models, International Journal of Fracture, 2013., vol. 184, no. 1-2.

[8] Kayabasi, O., Erzincanli, F., Finite element modelling and analysis of a new cemented hip prosthesis, Advances in Engineering Software, 2006., vol. 37, no. 7, pp. 477-483.

[9] Senalp A., Kayabasi O., Kurtaran, H., Static, dynamic and fatigue behaviour of newly designed stem for hip prosthesis using finite element analysis, Materials and Design, 2007., vol. 28, no. 5, pp. 1577-1583.

[10] Speirs, A., Slomczykowski, M., Orr, T., Siebenrock, K., Nolte, L.-P., Three-dimensional measurement of cemented femoral stem stability: an in vitro cadaver study, Cinical Biomechanics, 2000., vol. 15, no. 4, pp. 248-255.

[11] Bialoblocka-Juszczyk, E., Baleani, M., Cristofolini, L., Viceconti, M., Fracture properties of an acrylic bone cement, Acta of Bioengineering and Biomechanics, 2008., vol. 10, no. 1, pp. 21-26.

[12] Godec, M., Kocijan, A., Dolinar, D., Mandrino, D., Jenko, M., Antolič, V., An investigation of the aseptic loosening of an AISI 316L stainless steel hip prosthesis, Biomedical Materials, 2010., vol. 5, no. 4.

[13] Colic, K., Sedmak, A., Grbovic, A., Burzić, M., Hloch, S., Sedmak, S., Numerical Simulation of Fatigue Crack Growth in Hip Implants, Procedia Engineering, 2016., vol. 149, pp. 229-235.

[14] Pérez, M., García-Aznar, J., Doblaré, M., Seral, B., Seral, F., A comparative FEA of the debonding process in different concepts of cemented hip implants, Medical Engineering & Physics, 2006., vol. 28, no. 6, pp. 525-533.

[15] Jeffers, J., Browne, M., Lennon, A., Prendergast, P., Taylor, M., Cement mantle fatigue failure in total hip replacement: Experimental and computational testing, Journal of Biomechanics, 2007., vol. 40, no. 7, pp. 1525-1533.

[16] Achour, T., Tabeti, M., Bouziane, M., Benbarek, S., Bachir, B., Finite element analysis of interfacial crack behaviour in cemented total hip arthroplasty, Computational Materials Science, 2010., vol. 47, no. 3, pp. 672-677.

[17] Sedmak, A., Čolić, K., Burzić, Z., Tadić, S., Structural integrity assessment of hip implant made of cobalt-chromium multiphase alloy, Structural Integrity and Life, 2010., vol. 10, no. 2, pp. 161-164.

[18] Pyburn, E., Goswami, T., Finite element analysis of femoral components paper III - hip joints, Materials and Design, 2004., vol. 25, no. 8, pp. 705-719.

[19] Flitti, A., Ouinas, D., Bachir Bouiadjra, B., Benderdouche, N., Effect of the crack position in the cement mantle on the fracture behaviour of the total hip prosthesis, Computational Materials Science, 2010., vol. 49, no. 3, pp. 598-602.

[20] Griza, S., Zanon, G., Silva, E., Bertoni, F., Reguly, A., Strohaecker, T., Design aspects involved in a cemented THA stem failure case, Engineering Failure Analysis, 2009., vol. 16, no. 1, pp. 512-520.

[21] Yang, S.-Y., Yu, H., Gong, W., Wu, B., Mayton, L., Costello, R., Wooley, P., Murine Model of Prosthesis Failure for the Long-Term Study of Aseptic Loosening, Journal of Orthopaedic Research, 2007., vol. 25, no. 5, pp. 603-611.

[22] Griza, S., Reis, M., Reboh, Y., Reguly, A., Strohaecker, T., Failure analysis of uncemented total hip stem due to microstructure and neck stress riser, Engineering Failure Analysis, 2008., vol. 15, no. 7, pp. 981-988.

[23] Chao, J., López V., Failure analysis of a Ti6Al4V cementless HIP prosthesis, Engineering Failure Analysis, 2007., vol. 14, no. 5, pp. 822-830.

[24] Hernandez-Rodriguez, M., Ortega-Saenz, J., Contreras-Hernandez, G., Failure analysis of a total hip prosthesis implanted in active patient, Journal of Mechanical Behavior of Biomedical Materials, 2010., vol. 3, no. 8, pp. 619-622.

[25] Mierzejewska, Z., Oksiuta, Z., Failure analysis of a femoral hip stem made of stainless steel after short time of exposure, Acta Mechanica et Automatica, 2014., vol. 8, no. 3, pp. 146-150.

[26] Demiral, M., Abdel-Wahab, A., Silberschmidt, V., A numerical study on indentation properties of cortical bone tissue: Influence of anisotropy, Acta of Bioengineering and Biomechanics, 2015., vol. 17, no. 2, pp. 3-14.

[27] Abdel-Wahab, A., Maligno, A, Silberschmidt, V., Dynamic Properties of Cortical Bone Tissue: Izod Tests and Numerical Study, CMC, 2010., vol. 19, no. 3, pp. 217-237.

[28] Abdel-Wahab, A., Alam, K., Silberschmidt, V., Analysis of anisotropic viscoelastic properties of cortical bone tissue, Journal of the Mechanical Behaviour of Biomedical Materials, 2011., vol. 4, no. 5, pp. 807-820.

[29] Abdel-Wahab, A., Silberschmidt, V., Numerical modelling of impact fracture of cortical bone tissue using X-FEM, Journal of Theoretical and Applied Mechanics, 2011., vol. 49, no. 3, pp. 599-619.

[30] Abdel-Wahab, A., Maligno, A., Silberschmidt, V., Micro-scale modelling of bovine cortical bone fracture: Analysis of crack propagation and microstructure using X-FEM, Computational Materials Science, 2012., vol. 52, no. 1, pp. 128-153.

[31] Li, S., Abdel-Wahab, A., Demirci, E., Silberschmidt, V., Penetration of cutting tool into cortical bone: Experimental and numerical investigation of anisotropic mechanical behaviour, Journal of Biomechanics, 2014., vol. 47, pp. 1117-1126.

[32] Li, S., Abdel-Wahab, A., Silberschmidt, V., Analysis of fracture processes in cortical bone tissue, Engineering Fracture Mechanics, 2013., vol. 110, pp. 448-458.

[33] Li, S., Demirci, E., Silberschmidt, V., Variability and anisotropy of mechanical behaviour of cortical bone in tension and compression, Journal of Mechanical Behavior of Biomedical Materials, 2013., vol. 21, pp. 109-120.

[34] Alam, K., Kerchkhofs, G., Mitrofanov, A., Lomov, S., Wevers, M., Silberschmidt, V., On-line analysis of cracking in cortical bone under wedge penetration, Journal of Engineering in Medicine, 2012., vol. 226, no. 9.

[35] Ruszkowski, I., Orlić, D., Muftić, O., Endoproteza zgloba kuka, Jugoslavenska medicinska naklada, Zagreb, 1985.

[36] Bergmann, G., Deuretzbacher, G., Heller, M., Graichen, F., Rohlmann, A., Strauss, J., Duda, G., Hip contact forces and gait patterns from routine activities, Journal of Biomechanics, 2001., vol. 34, no. 7, pp. 859-871.

[37] Bergmann, G., Graichen, F., Rohlmann, A., Hip joint loading during walking and running, measured in two patients, Joural of Biomechanics, 1993., vol. 26, no. 8, pp. 969-990.

[38] Martens, M., Aernoudt, E., Meester, P., Ducheyne, P., Mulier, J.C., Langh, R., Kestelijn, P., Factors in the mechanical failure of the femoral component in the total hip prosthesis, Acta orthopaetica, 1974., vol. 45, no 5., pp. 694-710.

[39] Faller, A., Schuenke, M.: The Human Body, Thieme, Stuttgart, 2004.

[40] https://en.wikipedia.org/wiki/Genu_valgum

[41] https://en.wikipedia.org/wiki/Coxa_valga

[42] Total Hip Replacement, http://orthoinfo.aaos.org/topic.cfm?topic=A00377

[43] Total Hip Arthroplasty, https://www.ncbi.nlm.nih.gov/pmc/articles/PMC3257425/

[44] "Abaqus 2016 Documentation. Abaqus Analysis User's Guide".

[45] Abdel-Wahab, A., Silberschmidt, V., Experimental and numerical analysis of Izod impact test of cortical bone tissue, The European Physical Journal Special Topics, 2012., vol. 206, no. 1, pp. 41-50.

[46] Wirtz, D., Schiffers, N., Pandorf, T., Radermacher, K., Weichert, D., Forst, R., Critical evaluation of known bone material properties to realize anisotropic FE-simulation of the proximal femur, Journal of Biomechanics, 2000., vol. 33, no. 10, pp. 1325-1330.

[47] Ten-node tetrahedral element (C3D10 and F3D10), http://web.mit.edu/calculix_v2.7/CalculiX/ccx_2.7/doc/ccx/node33.html

[48] Niinomi, M., Fatigue characteristics of metallic biomaterials, International Journal of Fatigue, 2007., vol. 29, no. 6, pp. 992-1000.

[49] Verić, O., Diplomski rad, Fakultet strojarstva i brodogradnje, Zagreb, 2012.

[50] Broek, D., The Practical Use of Fracture Mechanics, Kluwer Academic Publishers, Dordrecht, 1988.

[51] Mlikota, M., Diplomski rad, Fakultet strojarstva i brodogradnje, Zagreb, 2010.

[52] Fracture Toughness,http://www.substech.com/dokuwiki/doku.php?id=fracture_toughness

[53] Anderson, T. L., Fracture Mechanics Fundamentals and Applications, CRC Press LLC, Texas, 1995.

[54] Plane Strain Fracture Toughness (KIC) Data Handbook for Metals, NTIS, SAD, 1973.

ENCLOSURE

I. CD-R disc